Optimization of the performance of a pixellated germanium Compton camera

A thesis submitted

for the degree of

Doctor of Philosophy

by

Walid Ghoggali

Department of Medical Physics and Bioengineering

University College London

2013

Declaration

I, Walid Ghoggali, confirm that the work presented in this thesis is my own. Where information has been derived from other sources; I confirm that this has been indicated in the thesis.

Abstract

A planar HPGe Compton camera for nuclear medicine applications that contains 177 pixels of $4 \times 4mm^2$, of which 25 are at the back detector, is being used to image point sources of Cs137 , line sources and clinical-like shape distributed sources. Experimental results are obtained to study the effects of energy resolution, position sensitivity, and reconstruction algorithms on camera images. Preamplified pulses are digitized for pulse shape analysis using gamma ray tracking GRT4s data acquisition cards to improve camera performance. Pulse shape analysis includes improving energy resolution of the camera, improving position sensitivity of the camera by using induced charges in neighboring pixels and implementing time coincidence algorithms to select good events. The energy resolution effects will be presented for three different energy resolutions at 662 keV; 1.4% by implementing a basic pulse height algorithm, 0.7% with a curve fitting algorithm and 0.3% by implementing the moving window deconvolution algorithm (MWD). By improving the position sensitivity from 2.5mm to 1.25mm, an improvement of 24% in spatial resolution is expected where the current

spatial resolution of a point source 5cm from the camera is 8mm. The results show that the effects of energy resolution are less important for this camera. Images are reconstructed using back-projection and ITEM (Imaginary Time Expectation Maximization) algorithms. Effects of scattering materials on embedded sources are studied. Different source distributions have been studied including point sources, line sources and clinical simulations (baby-heart-like distributed sources).

Contents

List of Figures

List of Tables

Acknowledgements

I would like to thank my supervisors Prof. Robert Speller and Prof. Gary Royle for all their helpful advice and support to finish this work. I would like to thank Mr. Ian Lazarus and Dr. Vic Pucknell of the Daresbury Laboratory, Nuclear Physics Group for their help with the DAQ system.

I would like to thank all family members, friends and colleagues who supported me during the years of my PhD.

Chapter 1

Compton Camera and Nuclear Medicine

1.1 Nuclear medicine

Nuclear medicine imaging obtains the in vivo image of the spatial and temporal distribution of the radioactive tracers (radio nuclides or radioactively labelled pharmaceuticals) within the patient's body. Nuclear medicine uses radiopharmaceuticals (labelled with radioactive isotopes) to diagnose and treat diseases. Nuclear medicine is unique in that it provides information about function of the body. It is fundamentally different from MRI, CT and other medical imaging techniques in that the radiation originates from inside the body. The principle works by injecting radioactive substances into patients, and capturing the radiation being emitted from inside

the body. Radiotracers participate in the biochemical or physiological processes in the body in the same way as the non-radioactive material. Tracing the radiotracers by external detectors leads directly to tracking the flow or distribution of analogs of natural substances in the body. Depending on the organ to be imaged, the selection of the radionuclide materials can be then selected. Specific Radioactive isotopes linked to radiopharmaceuticals are absorbed by specific organs which permits studying various functions of the body. Images represent the quantitative distribution of a radiopharmaceutical within the human body. The emissions from the radioactive isotopes within the body are detected with radiation detectors placed outside the body.

There are two types of radio active labels used in NM: single photon emitters and positron emitters. Single photon emitters emit one principal gamma ray or a sequence of directionally uncorrelated gamma-rays (Single Photon Emission Tomography (SPECT, figure 1.1) used to detect them). Positron emitters emits positrons that travel a short distance and annihilates with an electron to generate two 511keV gamma-rays traveling in opposite directions (180 degrees) (Positron Emission Tomography (PET, figure1.2) used to detect them)

Figure 1.1: SPECT scanner

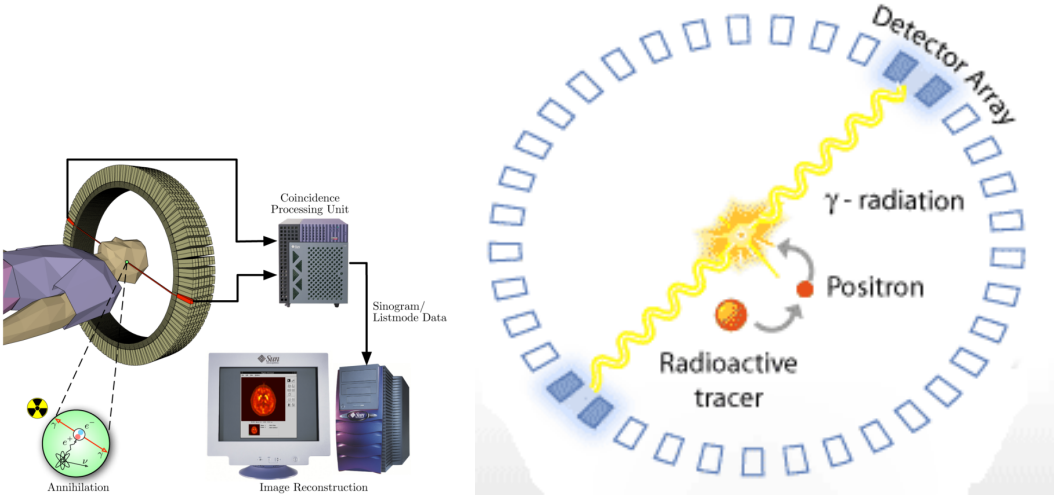

(a) PET scanner diagram (b) PET scanner

Figure 1.2: PET scanner

Recently a debate has begun to visualize the future of nuclear medicine after what PET has has achieved. One point of view expect that PET will completely replace SPECT [Alavi & Basu, 2008], and an opposing view expressed by [Mariani *et al.*, 2008] think that it is too early for such a dramatic change to happen in the near future.

In the middle of this heated debates that begun to surface, an alternative type of detector that address the limitations of SPECT would be much beneficial to the field of single photon radionuclides and the nuclear medicine community in general.

1.2 Compton camera

Among the advantages of the Compton camera Its superior detection efficiency and spatial resolution performances compared to SPECT for medium and high energy spectrum (energies above 250KeV). Compton camera uses Compton scattering principle to localize the origin of the incident gamma ray which eliminates the tradeoff between spatial resolution and detection efficiency found on SPECT technique.

1.2.1 Aim of the thesis

This thesis studies a high purity germanium Compton camera. This Compton camera is unique (to the best of my knowledge) in that it is made by a set of pixels all of which are made of germanium. hence, it is the first time for such a type of Compton camera to be investigated. The thesis demonstrates how the the spatial resolution of the UCL HPGe Compton camera is optimized by optimizing energy resolution and position sensitivity. The thesis will, in addition, demonstrate the ability of the camera to image point sources and distributed sources.

1.3 Thesis structure

To achieve the above aim, chapter 2 gives the theoretical background to the thesis, it starts by explaining the principle of Compton camera, it then explains how the angular and spatial resolutions are affected by the energy resolution, the energy of the incident gamma ray source, Doppler broadening and the geometry of the camera. A brief history of Compton cameras in literature is presented and the chapter finally explains the theory of charge creation in semiconductor detectors and how can be used to optimize the camera's performances, namely the position sensitivity. Chapter 3 describes the Compton camera and the DAQ system in details. Chapter 4 presents the results of energy resolution enhancements and the predicted angular and spatial resolution due to the energy resolution of the MWD algorithm and two offline algorithms. Chapter 5 presents position sensitivity enhancements work done for the pixellated HPGe of the UCL Compton camera combined with the predicted angular and spatial resolution due to the geometry of the camera. Chapter 6 presents the efficiency of the UCL Compton camera and the effects of energy resolution and position sensitivity on the spatial resolution of the UCL Compton camera measured from point source images and how they compare with the predicted, and finaly the chapter finishes by giving two examples to demonstrate the UCL Compton camera's capability to image distributed sources. The last chapter draws some conclusions and propose some future work.

Chapter 2

Compton Camera

2.1 Compton camera principle

A Compton camera is a medical imaging system that uses kinematics of Compton scatter in order to reconstruct the radioisotope image distribution. The diagram of figure 2.1 shown below highlights the main features of a Compton camera. The Compton camera consists of two position-sensitive γ-ray detectors; scatter (or front) and absorption (or back) detectors. Both, the front and the back detectors, should have a good energy and position resolution; and are working in time and energy coincidence. The scatter detector must have a high probability for photons to undergo a Compton scattering interactions (i.e. a low Z material). The absorption detector is where the scattered photons from the front are to be absorbed, thus the detector should have a high probability for photons to undergo a photoelectric interaction

(i.e. a high Z material). Although it is desirable to design the back detector in Compton cameras to absorb the scattered photons, coincidence events where the scattered photon is not absorbed can be used to reconstruct images if the incident gamma ray source energy is known (as is the case in nuclear medicine).

When an incident gamma-ray of Energy $E\gamma$ is scattered inside the front detector depositing an energy Ere (on a recoil electron), then the Compton scatter angle θ is given by the Compton equation (2.1):

$$\cos\theta = 1 - \left[\frac{E_{re}}{\alpha(E_\gamma - E_{re})}\right], \alpha = \frac{E_\gamma}{m_0 c^2} \tag{2.1}$$

where m_0c^2 is the rest mass energy of the electron. The electron is assumed free and at rest before the interaction.

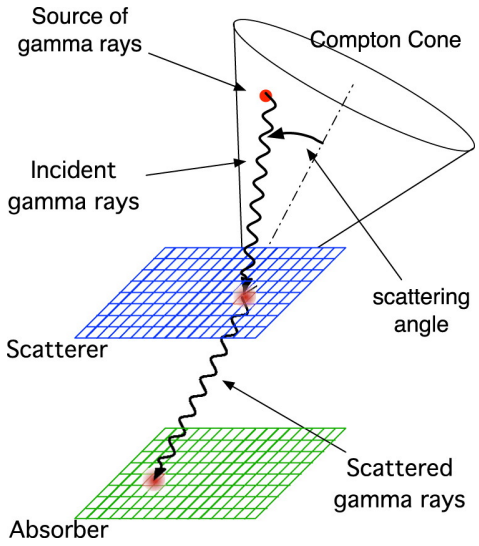

Figure 2.1: Compton camera principle

In order to understand the principle of the camera functioning, the imaging of a point source is considered and the same principle can be expanded for complex sources. On the diagram of figure 2.1 photons from the point source undergo a Compton scattering process in the scatter detector after which the scattered photons get absorbed and deposit their remaining energy in the absorption detector. The two detectors are made so that the energies deposited of the photons as well as their positions of interactions are measurable. This information is used in conjunction with the Compton equation (2.1) in order to localize the source.

The source is defined somewhere in the surface of the backprojected cone, which its apex originates from the position of the first interaction and its angle is the Compton angle. By considering many events, the intersection of the cones leads to the localization of the source.

The principle of imaging one point source can be extended for complex sources; an organ in the body or a tumour, since it can be considered as an array of point sources.

To back project an event from a photon, a Compton camera requires the following data: The energy of the incident photon, the energy deposited in both detectors and the position of the photon's interaction in both detectors.

2.2 Interaction of γ-Ray with Semiconductors

The interaction of gamma rays with semiconductor materials creates electron-hole pairs (charge carriers) that can be collected and measured directly as electrical signals. Many detector designs based on semiconductors (mainly germanium and silicon) are used to detect gamma rays; among those are, for example, pixel, strip and coaxial detectors. These detectors are capable of measuring both energy deposited and position of interaction.

Gamma rays interact with semiconductors mainly via three processes; namely photoelectric effect, Compton effect where the photon interacts with a target electron and pair production where the interaction is with the semiconductor nucleus. In both cases, part of the energy absorbed during the collision in the semiconductor will be converted into ionization (the creation of electron-hole pairs), the remaining of energy into phonons (lattice vibrations) which eventually converts into thermal energy. The energy needed to create an electron-hole pair is a characteristic of the material; it dependence on the band gap of the semiconductor. The band gap of Si and Ge respectively are 1.12eV and 0.67eV at T= 300K. The mean energy for electron-hole creation are 3.63eV and 2.96eV at T= 300K.

2.3 Compton Camera Brief History

The principle of the Compton camera and the possible advantages expected from it are outlined in many research works. Following is a brief historical account of some of the Compton camera imaging systems for medical applications that have been investigated over the last four decades. The principle of Compton cameras was first proposed by Todd, Nightingale, and Everett for nuclear medicine imaging [Todd *et al.*, 1974] and Schoenfelder for astrophysical applications [V. Schoenfelder, 1973]. The concept of the Compton camera is currently implemented for high energy x-ray imaging, the COMPTEL (Compton telescope), ATHENA (advanced telescope for high energy nuclear astrophysics) are examples of such applications. Since then a number of detector components and configurations have been proposed to investigate the possibilities of using this concept for medical applications. In 1983 Singh and Doria from the University of Southern California designed the first Compton camera for medical applications with a pixellated germanium array as a front detector and used a gamma camera without a collimator made of NaI(Tl) as a back detector [Singh & Doria, 1983]. Kamea and Hanada [Kamea & Hanada, 1988] proposed a new design for Compton cameras called multiple Compton camera. A multiple Compton camera consists of a series of large area thin silicon (or germanium) layers . Each layer is an independent, two dimensional, position sensitive detector. The layers are designed to be sufficiently thin so the probability of multiple interactions in any layer

is small [Dogan *et al.*, 1990]. In 1993 Martin and other researchers from the University of Michigan, propsed a Compton camera to image medium energy (0.5 to 3 MeV) gamma-ray fields. Their camera consists of two position sensitive detector arrays: a 4×4 planar array of high purity germanium crystals and a ring array of up to 64 NaI(T1) crystals. On previous Compton cameras designs a degradation on efficiency was reported and the explanation given was that direct hits of gamma rays in the back detector are the cause of this degradation. The proposed design addresses this issue by using a planar second detector a ring array which significantly reduces direct and small angle scattered events in the second detector [Martin *et al.*, 1993]. To address the issue of the tradeoff of field of view and the number of readout electronics channels in Compton cameras, one idea is to cover the field of view of a SPECT detector. However, Bolozdynya and others built high pressure xenon scintillation drift chamber Compton cameras for low energy y-rays. Traditionally, Si and Ge semiconductor detectors have been investigated as Compton scatter detectors because of their good energy resolution. With such detectors it is, however, difficult to achieve a clinically useful field of view with a reasonable number of readout channels. Compared with ionization and semiconductor detectors, the high-pressure xenon gas electroluminescent chamber detector has an optical readout not affected by the capacitance of the electrode structure and uses a small number of readout channels over a large field of view [Bolozdynya *et al.*, 1997].

In the last four decades of Compton cameras, researchers used different geometrical designs, different materials for the front and the back detectors, 3D detectors and different readout electronics designs to address, mainly, the limitations of spatial resolution and efficiency. These limitations governed mainly by detectors and electronics technology which have prevented the theoretical advantages of the Compton camera principle from being fully realized: For example the anticipated enhancement in sensitivity has not been achieved, a reduction of sensitivity by a factor of three has been reported by Singh [Singh & Doria, 1983]. This means that the gap between anticipated and achieved performance is large. However, continual advances in these technologies is slowly closing the gap to overcome these challenges and eventually close the gap between the anticipated and the achieved performances.

Table 2.1 summarizes some of the Compton cameras that have been built and tested to date .

Table 2.1: Previous Research

Research Group	Year	Detector Material	Energy Resolution	Angular Resolution	Efficiency	Position Resolution	Analytical Images	Experimental Images
University of Southern California	1983	HPGe/NaI(Tl)(C-SPRINT)	HPGe = 0.7% NaI=10 % at 140 keV	6.8	2.6×10^{-3} for 140 keV			Point source (140 and 662keV)
University of Michigan	1998	Si/NaI(Tl) (C-SPRINT)	Si = 1% at 140 keV NaI=9% at 140 keV	2.2 at 360 keV	2.7×10^{-3} for 140 keV	7.2 mm (x-y-z)	Point and line (662 keV)	
University of Michigan	2001	CZT	1.7% at 662 keV	3 at 511keV	1.5×10^{-4} for 511 keV			
University of Liverpool	2007	HPGe	2% at 122 keV	6 at1408 keV	4×10^{-2} for 662 keV	1mm(x-y-z)		Point source (1408 keV)
Los Alamos National Laboratory, USA	2008	Si/NaI(Tl)	4.3% at 834 keV	-	-	-	Point, distributed source	Point, distributed source
University College London	2009	HPGe	0.7% at 662keV	3 at 662 keV	3.06×10^{-5} for 662 keV	1.25 mm (x-y-z)	-	Point, distributed source (662 keV)
Institute of Space and Astronautical Science, Japan	2005	Si/CdTe	1% at 511 keV	3.5 at 511 keV	1×10^{-2} for 360 keV	-	-	Point source (120, 356, 511, and 662 keV)
Institute of Space and Astronautical Science, Japan	2009	Si/CdTe	1% at 511 keV	3.5 at 511 keV	1×10^{-2} for 360 keV	-	-	distributed source (360 keV)
Harvard University	2010	Si/NaI(Tl)	Si = 1% at 140 keV NaI=8% at 140 keV	8.6 at 511 keV	4.15×10^{-8} for 511 keV	3mm(x-y)	-	Point source (511 keV)
University of Kyoto	2009	Time Projection Gas Chamber /GSO	TPG= 15.4%	7 at 662 keV GSO= 8% at 662 keV	1×10^{-5} for 360 keV	6 mm (x-y-z)		Point, distributed source, and small animal (360 and 511 keV)
University of Kyoto	2010	Time Projection Gas Chamber /GSO	TPG= 15.4% LaBr3(ce)= 3% at 662 keV	4.2 at 662 keV	-	-	-	-

2.4 UCL Compton camera

Instead of having one small first detector and a large back detector, the UCL Compton camera has been designed such that the back detector is the smallest. Also the first detector was constructed such that it consists of many separate sub-detectors (8 sub-detectors). This approach of dividing the detector into a set of separate sub-detectors will be discussed in the following section.

In previous works on Compton cameras, the back detector was made larger than the front detector in order to optimise the camera efficiency [Royle *et al.*, 2003]. In the case of our camera, however, the front was made larger than the back detector. The detection efficiency is strongly affected by the size of the front and back detectors. Therefore, the design will increase the probability of gamma rays hitting the front detector and will on the other hand decrease it in the back detector. This leads to comparable detection efficiency to the existing Compton cameras, where the probability of gamma rays hitting the back detector is more significant. An estimation of the camera efficiency has been calculated for a point source of distance 5cm from the camera face [Royle *et al.*, 2003].

Another characteristic of the UCL Compton camera differentiate it from other existing designs is that the front detector has been divided into small sub-detectors. All the existing designs of Compton cameras use single front detector and single back detector. This design leads to a significant degradation in efficiency. Because the

data are collected using a single detector, multiple interaction events were recorded within the same detector (multiple interactions happened in different pixels or strips at the same time). It is necessarily to eliminate those events, because the drifting charges not only induce signals in the adjacent pixels (strips) but in all pixels (strips). This, leads to overlapping between the induced signals from different interactions and therefore an ambiguity in finding the interaction position. The degradation could reach 95% for this type of detectors design.

Although the UCL Compton camera has the front detector divided into eight sub-detectors, this will improve the efficiency. However, the efficiency would be higher if the UCL Compton camera had a back detector sub-divided into sub-detectors.

2.5 3D Detectors For Compton Cameras

Two types of configurations double-strip and pixel array configurations are normally the main 3D detector configurations used to build Compton cameras. Figure 2.2 shows a diagram of a pixellated and a double-strip detector configuration. In the pixellated configuration the semiconductor is segmented into small equal pixels with N^2 pixels (N^2 electronics channel), while in the double-strip configuration the semiconductor is segmented into N parallel strips (N electronics channel). Thus, it can be concluded that the double-strip configuration needs fewer readout electronics than the pixel array. Therefore, the cost is considerably reduced in the double-strip configuration.

However, the readout electronics complexity in reading a large number of channels in the pixel array configuration is no longer a challenge with the recent development in the field of nano-technology. Also this configuration (pixel array) can result in the minimum electronic noise because the total leakage current is shared among a large number of pixels and the capacitance of each pixel is minimized [Zhang *et al.*, 2004]. The UCL Compton camera has a pixellated geometry.

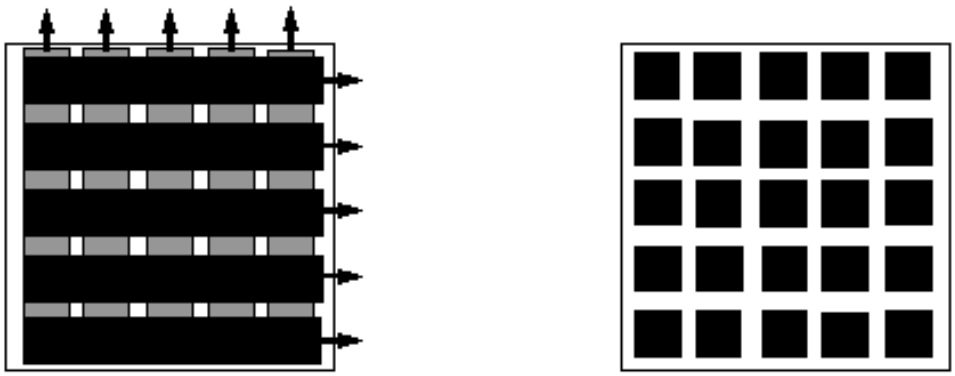

Figure 2.2: Double strip and pixel 3D detectors configurations

The energy resolution depends mainly upon two physical factors. It is directly related to the material and the geometry (configuration) of the detector. It is well known that High Purity Germanium semiconductors (HPGe) have the best energy resolution compared to silicon and other room temperature semiconductors (i.e. HgI2, CdTe, CdZnTe). This is due to the differences in the loss of charge carriers during the drift time. For the HPGe the loss can be always ignored, however, it is significant in the other semiconductor materials.

The weighting potential for the two configurations is the same. The difference is

in the rate of increase as we approach the electrodes (pixel or strip). This is because the differences in the size of electrodes. In order for a detector to have a better energy resolution, the collection of charge carriers has to be complete. It is not, however, due to charge carriers trapping, which varies from a semiconductor material to another. For example, the HPGe has the lowest charge trapping; however, in the case of room temperature semiconductors the trapping of holes is quite significant. Due to this limitation, both configurations are made such that they are a single polarity charge. In other words electrodes are either sensitive to electrons or holes. For both configurations the weighting potential is almost zero when charge carriers move on the region far away from the electrode (pixel or strip). However, the weighting potential is very strong near the electrode (pixel or strip). The induced charge therefore is then created mostly from the charges crossing the region near the electrode. The pixel array has a better energy resolution [Zhang *et al.*, 2004] over the double-strip configuration. This is due to the smaller area of the pixel compared to the strip; the increase of the weighting potential is much lower in the case of pixel array compared to the double-strip configuration. The smaller the ratio between the dimension of each electrode to the thickness of the detector, the lower the increase of the weighting potential. Therefore, the pixel array configuration is more sensitive to single charge carriers. Therefore the pixel array configuration has a better energy resolution compared to the double-strip configuration.

For both configurations the X-Y position sensitivity (position resolution of gamma ray interaction within the pixel/strip) is calculated by comparing the induced signals of the neighboring pixels (strips). For instance, to improve the X position sensitivity beyond the pixel (strip) size consider two neighboring pixels (strips) (one at the right hand and the other at the left hand side of the pixel (strip) where the interaction took place) if the induced signal is more significant on the left pixel (strip) this means that the interaction took place in the half part of the pixel (strip) near the left pixel (strip). And therefore the position sensitivity is enhanced by a factor of two.

Strips have high probability compared to pixels in housing multiple gamma ray interactions at the same time. This, leads to an uncertainty (ambiguity) in finding the position of gamma ray interaction. Which in turn have a direct impact on the image resolution. Due to the small area of pixels, the probability for a pixel to house multiple gamma ray interactions is much lower.

In the pixel array configuration, pixels at the edges of a sub detector array, when an interaction happens in them, do not have the capability of enhancing the position sensitivity. This is because to find the position of a gamma ray interaction within a given pixel with an improved position sensitivity, the pixel has to have at least 4 neighboring pixels (from the right, left, top and bottom sides). This is because the induced signals in those pixels are used to find the position. In the case of the pixels at the edges there are between three and five neighboring pixels (depending on the

position of the pixel). In the double-strip configuration the same limitation exists, however, the number of strips that will not have the capability of position sensitivity enhancements are four. This number is the same for any size of the detector (it does not depend on how much strips a detector has) because there is always four strips at the edges. However, in the pixel array configuration the larger the detector is the larger the number of pixels at the edges, in total for a detector of $N \times N$ pixels, 3N pixels are at the edges.

2.6 Energy Resolution

2.6.1 Fano Factor

For a given energy absorbed in a semiconductor, the number of electron-hole pairs created is subject to some fluctuation due to the variation in the amount of energy which ends up in electron-hole creation and phonon generation. This in turn has an effect on energy resolution achievable for a given semiconductor detector.

The energy needed to create an electron-hole pair in a semiconductor is not constant but fluctuates around a mean value N given by (2.2):

$$N = \frac{E}{\epsilon} \tag{2.2}$$

E is the energy absorbed and ϵ is the mean energy spent for creating an electron-

hole pair (2.96eV for Ge at 300K). The Fano factor F is introduced as an adjustment factor to relate the observed variance to the Poisson predicted variance in the number of charge carriers N(electrons or holes)(2.3):

$$F \equiv \frac{N}{E/\epsilon} \tag{2.3}$$

The Fano factor for Si and Ge for example are 0.115 and 0.13 respectively.

2.6.2 Noise

The proportionality of charge and absorbed energy in semiconductor can be affected by noise originates from the detector and the readout electronics.

There are two main detector related factors that affect energy resolution in semiconductor detectors. First, Incomplete charge collection in semiconductor detectors will lead to energy measurements fluctuations for a given absorbed energy. Second, the leakage current adds statistical fluctuations to the measured signal.

Charge collection is affected by two effects, trapping and recombination. Recombination is significant in applications where unbiased diodes are used; in applications where biased diodes are used, which is the case in Compton camera applications, recombination is insignificant. Recombination occurs between radiation-generated electrons and holes as long as are not separated by an applied electric field or by diffusion. Trapping, however, which is the temporary capture and delayed release of

charge carriers caused by local material defects , could be of a significant importance in energy measurements precision. Because the signal created from an electron-hole pair is proportional to the distance between electron and holes once they stopped (either at the electrodes or by being trapped), and because the path taken by a given electron-hole pair created by a given interaction position vary, the probability of trapping vary as the local defects are not uniform across the detector. This would lead to fluctuations in the measured signal and hence on the energy resolution of the detector. Also, because the probabilities of electron and hole capture (trapping) is different, trapping will lead to a depth dependence of the signal created for every interaction position.

2.6.3 Moving Window Deconvolution

There are two approaches used in gamma ray spectroscopy to measure gamma ray energies: analog shaping and digital shaping. For systems that use analog shaping the preamplifier's output is followed by an analog shaping stage before the ADC stage after which the energy is measured by measuring the amplitude of the shaped signal. For systems that use digital shaping, the implementation of the shaping filter happens numerically where the preamplifier's output is directly digitized using an ADC. The moving window deconvolution (MWD) is a digital energy measurements algorithm implemented in the GRT4's FPGAs. Advantages of digital shaping over

analog shaping include the ability to implement complex shaping functions that are difficult or impossible to implement using analog electronics and the second advantage is that only the preamplifier's stage is subject to environment's changes which affects the performances of the shaping stage.

The MWD [Georgiev & Gast, 1993] implements a trapezoidal shaping which is known to be the optimal shaping for detectors where the pulse shape is dependent on the depth of interaction. The signal from the preamplifier, which is an exponential decaying signal, is transformed into a stair case signal after which a moving average operation removes high frequency noise and finally generates a trapezoid signal shape.

A radiation event produces an amount of charge proportional to the energy deposited in the detector. The charge results in a steplike waveform at the preamplifier output and its signal is described by equation (2.4):

$$U_p(t) = \int_{-\infty}^{+\infty} g(\tau) f(t-\tau) \tag{2.4}$$

Where the preamplifier's output signal $U_p(t)$ is described by a convolution between the charge distribution function $g(t)$ and the preamplifier impulse response $f(t)$.

In order to perform deconvolution the preamplifier's output is digitized where the integral of equation (2.4) becomes a sum:

$$U_p(it_s) = \sum_{j=0}^{\infty} g(jt_s) f(it_s - jt_s) \tag{2.5}$$

where t_s is the sampling time. if the time scale is normalized to t_s equation (2.5) becomes:

$$U_p(i) = \sum_{j=0}^{\infty} g(j) f(i-j) \tag{2.6}$$

For a resistor feedback preamplifier which corresponds to a single pole transfer function. Then $f(n) = k^n$, where $k = e^{-\alpha}$ and α is the decay time of the exponent. Therefore, the solution to equation (2.6) is given by equation (2.7) for $i \cap (z, z+M)$:

$$G(i) = \sum_{j=z}^{i} g(j) = U(i) + (1-k) \sum_{j=z}^{i-1} U(j) \tag{2.7}$$

where z is an arbitrary time reference and M is the window size. When the index i reaches the right limit of the window, the total charge $G(n = z+M)$ in the window $(z, z+M)$ is extracted. Therefore, for any further window shifted by one sampling time interval with respect to the previous one, the total charge is given by for any $n > z+M$:

$$G(n) = \sum_{j=n-M}^{n} g(j) = U(n) - U(n-M) + (1-k) \sum_{j=n-M}^{n-1} U(j) \tag{2.8}$$

2.7 Spatial and Angular Resolution

The spatial resolution SR, ignoring the contribution of the image reconstruction algorithm, given by the FWHM of the point spread function (PSF) for a Compton camera at a distance D from the camera is related to the angular resolution $\Delta\theta$ by equation (2.9). Therefore, once the angular resolution is known, the spatial resolution can be calculated knowing the source distance from the camera. The angular uncertainty $\Delta\theta_{tot}$ results from the uncertainty of energy measurement of the scatter detector $\Delta\theta_{energy}$, the Doppler broadening effect of the scatter detector $\Delta\theta_{Doppler}$, and the geometry contribution $\Delta\theta_{Geo}$ (uncertainty of determining the positions of interactions in the scatter and the absorption detectors, the source to detector distance and the physical dimensions of the camera). The uncertainty of the position of the interactions in the two detectors results in an uncertainty on the cone's axis; whereas, the uncertainty on the energy and the Doppler effect result on an uncertainty on the cone's angle θ. The total angular resolution, given by equation (2.10), is the quadratic summation of the three quadratic uncertainties [Du *et al.*, 2001]:

$$SR = Dtan(\Delta\theta) \tag{2.9}$$

$$\tan^2(\Delta\theta_{tot}) = \tan^2(\Delta\theta_{energy}) + \tan^2(\Delta\theta_{Doppler}) + \tan^2(\Delta\theta_{Geo}) \tag{2.10}$$

2.7.1 Energy Uncertainty Contribution

The energy uncertainty contribution to the angular resolution is derived from the Compton camera equation (2.1) using error propagation [Du *et al.*, 2001]:

$$(\Delta\theta_{energy})^2 = (\frac{d\theta}{dE_{re}})^2(\Delta E_{re})^2 + (\frac{d\theta}{dE_{\gamma}})^2(\Delta E_{\gamma})^2 \tag{2.11}$$

Because in nuclear medicine applications the energy of the incident gamma ray E_{γ} is known, the equation (2.11) becomes:

$$(\Delta\theta_{energy})^2 = (\frac{d\theta}{dE_{re}})^2(\Delta E_{re})^2 \tag{2.12}$$

where by using equation (2.1):

$$(\frac{d\theta}{dE_{re}}) = \frac{(1+\alpha(1-\cos\theta))^2}{E_{\gamma}\alpha\sin\theta} \tag{2.13}$$

Which results in the equation below that represents the energy contribution to angular resolution:

$$\Delta\theta_{energy} = \left[\frac{(1+\alpha(1-\cos\theta))^2}{E_{\gamma}\alpha\sin\theta}\right]\Delta E_{re} \tag{2.14}$$

It is clear from equation (2.14) that the angular uncertainty due to energy contribution is inversely proportional to the gamma ray energy: the higher the energy

the better the angular resolution, which makes the Compton camera perform better at medium to high energies ($> 250keV$). Also, the better the energy resolution of the scatter detector the better the angular resolution. In addition, the angular uncertainty is proportional to the scattering angle by $1/\sin\theta$. The graphs below show how the angular resolution changes with the scattering angle θ, the energy resolution (which is a characteristic of the material used) and the gamma ray energy.

To show the effects of energy resolution, the materials Ge, Si, CZT were chosen to show the effects of the energy resolution. These materials are used to design most of the Compton cameras. To study the effects of incident energy, gamma ray energies of 662keV, 511keV, 364keV and 140keV were chosen because they cover the whole spectrum of nuclear medicine applications. The energy resolutions of the different materials used were estimated from mathematical models found in the literature. The energy resolutions of Germanium is given by the equation (2.15) [Ordonez *et al.*, 1997a] and that of Si is given by the equation (2.16) [Conka-Nurdan *et al.*, 2002], CZT is given by the equation (2.17) [Du *et al.*, 2001].

$$\Delta E_{re}(MeV) = \sqrt{1.055 + 1.064 \times 10^{-3} \times E_{re}(MeV)} \tag{2.15}$$

$$\Delta E_{re}(MeV) = 8.5 \times 10^{-5} \sqrt{330 \times E_{re}(MeV) + 1} \tag{2.16}$$

$$\Delta E_{re}(MeV) = 6.0 + 0.15\sqrt{E_{re}(MeV)} \tag{2.17}$$

Figure 2.3 shows, for an incident energy of 511kev, the angular resolution for Ge, Si and CZT which have different energy resolutions of which Ge is the best and CZT is the worst. In the case of germanium for scattering angles between 5° and 130°, the angular resolution is below 1°, for scattering angles below 5° and scattering angles between 130° and 170° the angular resolution is between 1° and 10°, and for scattering angles above 170° the angular resolution goes up to 100°; In the instance of silicon for scattering angles between 10° and 90°, the angular resolution is below 1°, for scattering angles below 10° and scattering angles between 90° and 165° the angular resolution is between 1° and 10°, and for scattering angles above 165° the angular resolution goes up to 100°; For CZT, for scattering angles between 5° and 135°, the angular resolution is between 2° and 10°, for scattering angles below 5° and scattering angles above 135° the angular resolution is goes up to 100°; Germanium, silicon and CZT have the minimum angular resolution at roughly the same scattering angle of 40°. It is clear from this graph the importance of a good energy resolution for Compton cameras to get a good angular resolution as well as the importance of the scatter angle range.

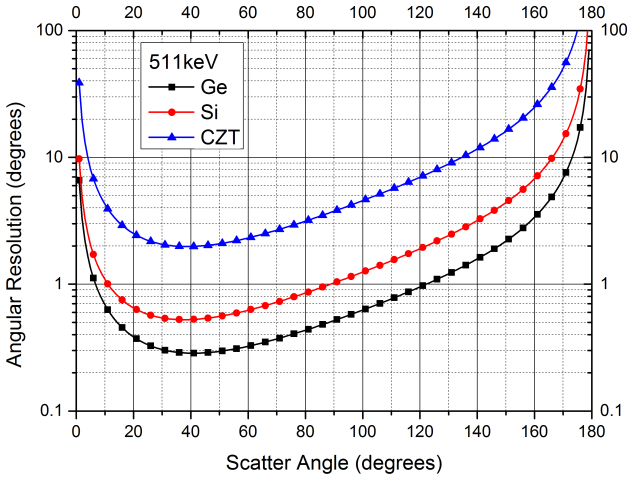

Figure 2.3: Angular Resolution for Ge, Si, CZT semiconductor materials where the effects of energy resolution are shown for a gamma ray source of 511keV

Figure 2.4 shows the effects of the incident gamma ray energy for silicon and for gamma ray energies of 662keV, 511keV, 364keV and 140keV. For 662keV gamma ray source and scattering angles between 5° and 130°, for 511keV and scattering angles between 7° and 125°, for 364keV and scattering angles between 15° and 110°, for 140keV and scattering angles between 10° and 160°; the corresponding angular resolutions are below 1° for 662keV, 511keV and 364keV; however, for 140keV the angular resolution is between 2° and 10°. This shows that the Compton camera is best suited for imaging gamma ray sources of medium to high energies, but is not best for imaging low energies.

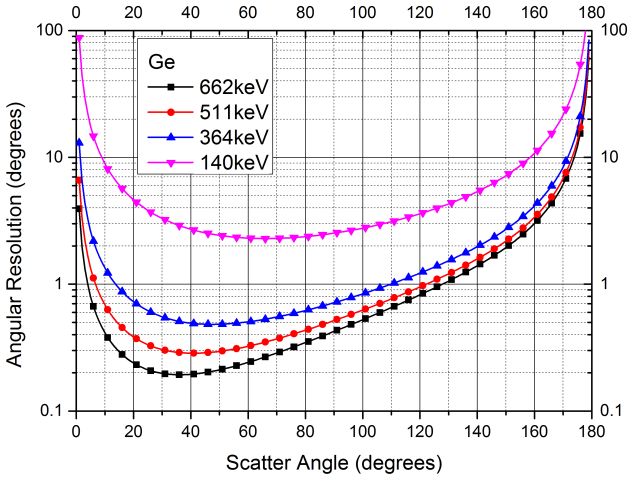

Figure 2.4: Effects of gamma ray source energy on angular resolution for Si

2.7.2 Doppler Broadening Contribution

The Compton equation (2.1) is used to relate the energy measured in the detector to the scatter angle. The Compton equation gives a one-to-one relationship between the scatter angle and the energy, which is only true when the electron involved in the Compton scattering interaction is considered at rest; however, in reality, gamma ray interacts with moving electrons bound to atoms. the effect of electron motion is manifested by the broadening of the energy spectra of both scatter and absorption detectors, which results in an additional source of energy uncertainty. The equation that accounts for the electron's non-zero pre-collision energy and momentum is given by (2.18) [Ordonez *et al.*, 1998]:

$$p_z = -m_0 c \frac{E_0 - E_A - E_0 E_A (1 - \cos\theta)/m_0 c^2}{\sqrt{E_0^2 + E_A^2 - 2E_0 E_A \cos\theta}} \tag{2.18}$$

where p_z is the projection of the electron's pre-collision momentum on the momentum-transfer vector of the gamma ray.

The degree of the Doppler broadening in a target atom can be calculated from the probability for Compton scattering from an electron in the nth sub-shell into a scatter energy and scatter angle of E_A and θ respectively. This probability is given by a double-differential cross section [Ribberfors, 1975]:

$$\left(\frac{d^2\sigma}{d\Omega dE_A}\right)_n = \frac{m_0 r_0^2}{2E_0}\left(\frac{E_c}{E_0} + \frac{E_0}{E_c} - \sin^2\theta\right) \times \frac{E_A}{\sqrt{E_0^2 + E_A^2 - 2E_0 E_A \cos\theta}} J_n(p_z) \tag{2.19}$$

where $J_n(p_z)$ is the Compton profile for the nth sub-shell of the target atom. r_0 is the classical electron radius and E_c is the energy given by the Compton equation. The Compton profiles used to study the effects of Doppler broadening for the UCL Compton camera are taken from [Biggs *et al.*, 1975] and [Reed & Eisenberger, 1972], both gives values for Ge and were used for comparison reasons (see Chapter 4).

The angular uncertainty due to the effects of Doppler broadening is given by equation (2.20) [Ordonez *et al.*, 1998]:

$$\sigma_\theta = \frac{1}{k_\theta}\left(k_{p_z}\sigma_{p_z}\right) \tag{2.20}$$

where

$$k_\theta = \left(\frac{1}{m_0c^2} - \frac{\bar{p_z}}{m_0cw}\right)\bar{E_A}E_0\sin\theta \tag{2.21}$$

$$k_{p_z} = \frac{w}{m_0c} \tag{2.22}$$

$$w = \sqrt{E_0^2 + \bar{E_A^2} - 2E_0\bar{E_A}\cos\theta} \tag{2.23}$$

The parameter σ_{p_z} can be estimated from the width of the total Compton profile of the target atom.

2.7.3 Geometry Contribution

To predict the geometry contribution to angular resolution, the work done by [Ordonez *et al.*, 1999] was adopted. The geometry contribution to angular resolution is due to the fact that the uncertainty in defining the positions of the interactions in the front and the back detectors. These positions determine the axis of the Compton cone and the position on the front defines the vertex of the cone. The uncertainties in defining the interaction positions comes from the limitations of the detectors spatial

resolutions.

The overall FWHM angular resolution is given by equation (2.24):

$$[\Delta\theta]^2 = [\Delta\theta_S]^2 + [\Delta\theta_A]^2 \tag{2.24}$$

Where $\Delta\theta_S$ is the angular resolution of the front detector, and $\Delta\theta_A$ is the back detector contribution.

The front detector's $\Delta\theta_S$ contribution is given by equation (2.25):

$$[\Delta\theta_S]^2 = \frac{1}{R_1^2}\left((\Delta x_S cos\phi)^2(1+\alpha cos\theta)^2 + (\Delta y_S sin\phi)^2(1+\alpha cos\theta)^2 + (\Delta z_S \alpha sin\theta)^2\right) \tag{2.25}$$

Where R_1 is the distance between the source and the interaction position in the front detector; $\Delta x_S, \Delta y_S$ and Δz_S are the front detector resolution vector's Δr_S components; ϕ and θ are the polar and azimuth angles in spherical coordinates. α equals to R_1/R_2 where R_2 is the distance between the interactions positions in the front and the back detectors.

The back detector's contribution to angular resolution $\Delta\theta_A$ is given by equation (2.26):

$$[\Delta\theta_S]^2 = \frac{1}{R_2^2}\left((\Delta x_A cos\theta cos\phi)^2 + (\Delta y_A cos\theta sin\phi)^2 + (\Delta z_A sin\theta)^2\right) \tag{2.26}$$

Where $\Delta x_A, \Delta y_A$ and Δz_A are the back detector resolution vector's Δr_A components.

For Compton cameras of isotropic spatial resolutions ($\Delta x_D = \Delta y_D = \Delta z_D$) or with uniform resolution along two out of the three axes (i.e. UCL Compton camera) ($\Delta x_D = \Delta y_D \neq \Delta z_D$), where $D = S$ or A, equations (2.25) and (2.26) reduce to (2.27):

$$\Delta\theta_{Geometry} = \sqrt{\frac{(\Delta r_A)^2}{(R_2^2} + \frac{(\Delta r_S)^2}{(R_1^2}\left[1 + \frac{R_1^2}{R_2^2} + 2\frac{R_1}{R_2}cos\theta\right]} \tag{2.27}$$

From equation (2.27) the angular resolution is almost inversely proportional to R_2 which translates to the fact that the larger the detector separation between the front and the back the better is the angular resolution. Likewise $\Delta\theta_{Geometry}$ is also almost inversely proportional to R_1, which means the further the source is from the camera the better is the angular resolution [Ordonez *et al.*, 1999].

2.8 Signal Formation in a Pixellated Gamma Ray Detector

2.8.1 Charge Creation

Gamma rays undergoing interactions in a pixellated semiconductor detector give rise to mobile electron-hole pairs. The cloud of charges moves under the influence of the applied electric field between the anode and cathode of the detector. The magnitude of these charge signals collected by the electrode corresponds to the energy deposited by the photon and their characteristics depend on the interaction position.

Figure 2.5 shows a cross section of a pixellated detector with a bias potential of Vb. When a gamma ray interacts within the detector, the electron-hole cloud created will separate and drift to the electrodes under the influence of the electric field. Electrons travel towards the positive electrodes, holes go in the opposite direction.

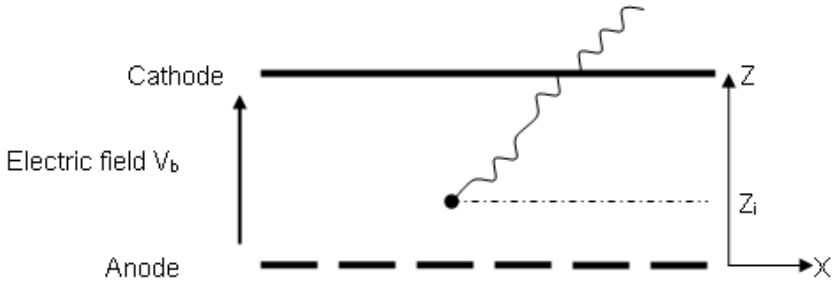

Figure 2.5: Cross section of a pixellated detector. the continuous top electrode is connected to a bias voltage Vb. Pixel electrodes are held at a ground potential

Once the cloud is created within the semiconductor, it will induce a surface charge

on any existing electrodes. Initially the density of the surface charge will be nearly uniform on the surrounding pixels when the charge cloud is relatively far from the electrodes. However, as the cloud becomes closer to a given pixel, the surface charge becomes more concentrated on the closest pixels [Eskin *et al.*, 1999]. Since the current induced is due to charge movement and not whether or not the charge reaches the electrodes, the central pixel, as well as surrounding pixels, record the presence of charge movement. However, as the magnitude of induced signal depends on the distance between the pixel and the charge cloud, the central pixel will record the biggest pulse. This simple explanation of the creation of induced charges in the main and neighboring pixels, can be explored and expanded by considering the concept of the near field-effect and weighting potentials, after considering the Ramo-Shockley theorem.

2.8.2 Ramo-Shockley theorem

Ramo [Ramo, 1939] proved a theorem which had been introduced by Shockley [Shockley, 1938] earlier. The RamoShockley theorem introduced what is referred to as a weighting field (E_w). This is the electric field appearing within a volume that contains an arbitrary number of electrodes held at a fixed potential in the presence of a point charge e moving with velocity v. This field appears within the volume if the electrode of interest is raised to unit potential and all other electrodes kept at ground

potential. Under these conditions the electrode current i due to a charge e at point r is ([Ramo, 1939], [Shockley, 1938]):

$$i = ev(r)E_w(r) \tag{2.28}$$

The integral of electrode current can be found by means of a weighting potential, w. The right side of (2.28) is the time derivative of $-ew(r)$, so as the point charge e moves from position r_1 to r_2 , the net charge built up on an integrating capacitor connected to the electrode would be:

$$Q = e[\phi(r_2)\phi(r_1)] \tag{2.29}$$

2.8.3 Weighting potentials and the near field effect

The notion of weighting potentials is important in understanding the mechanism by which induced signals are created in a pixellated detector. Figure 2.6 shows the weighting potential due to the central pixel. The potential gradually becomes stronger moving towards the pixel surface. This is known as the near-field effect.

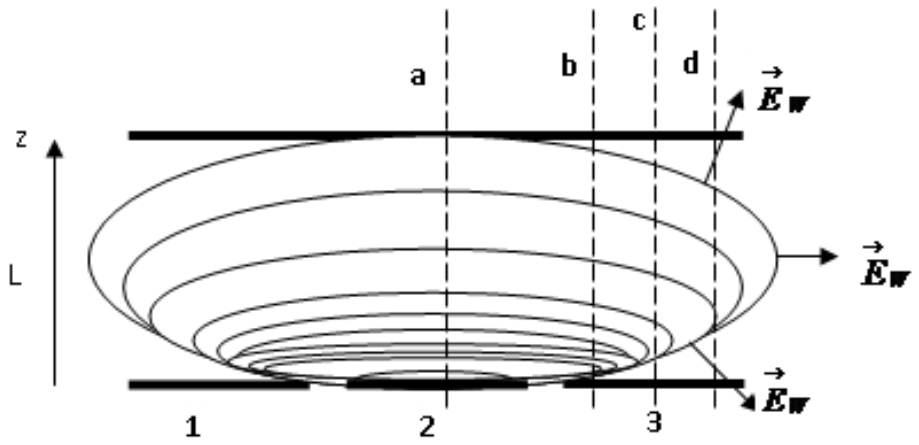

Figure 2.6: Weighting potential plots for a pixilated detector represent the weighting field

The weighting potential for the neighboring pixels would be identical to that of the central pixel. It is important to appreciate that the charge moving in a neighboring pixel will be influenced by the central pixel weighting field.

Figure 2.7 shows the weighting potential variation as a function of distance from the pixel surface. The graph on the left hand side (labeled a) is the weighting potential as measured along line 'a' in figure 2.6 and the graph on the right hand side is taken along line 'b', 'c' and 'd'.

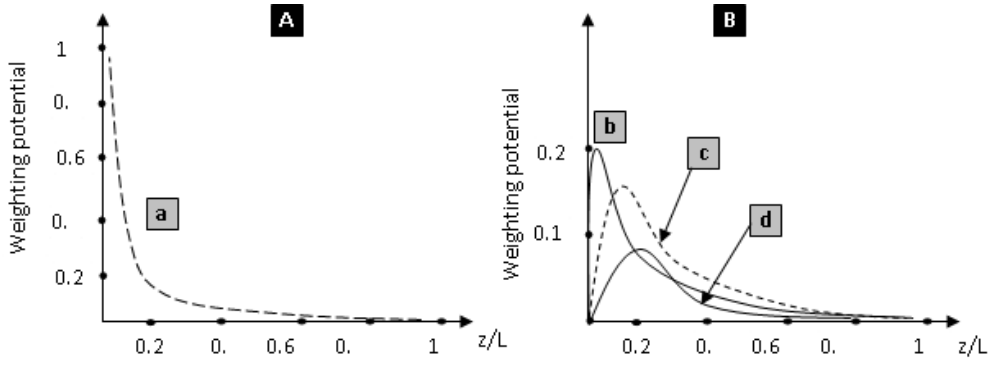

Figure 2.7: Weighting potentials in function of a normalized depth and lateral (x or y)

There are two types of weighting potential waveforms: When inside the pixel, the potential falls away from the pixel surface (line a). When outside the central pixel (lines b, c and d), the potential first increases then falls as the point of interest moves away from the pixel surface.

A great variety of resultant signal waveforms for the induced current in the adjacent pixels may arise depending on the particle type and the charge carrier transit time. Consider figure 2.6, a charge q_m traversing the full distance between the electrodes along line 'a' would produce a bipolar signal, whereas the same charge traversing half this distance will give rise to a unipolar pulse whose polarity depends on the polarity of the charge. The reason for this behavior is the direction of the weighting field and whether or not its direction changes as the path of the charge changes [Radeka, 1988].

2.8.4 Induced charge creation process

When a gamma ray hits a pixel in a given pixellated geometry, the induced signals created in the surrounding pixels depend on the the energy deposited in the detector and the X, Y, Z position of the interaction.

2.8.5 X, Y dependence

Figure 2.8 shows the X, Y dependence. In these graphs two interactions at two different positions have been recorded. The first interaction occurred close to the left pixel (dashed line) and thus the amount of charge induced in the left pixel is less than that induced in the right pixel. For the second interaction which occurred close to the right pixel, the opposite happens so that the induced charge on the left pixel is greater than that on the right pixel. Therefore, from this explanation some conclusions can be drawn so that a simple algorithm can be developed in order to improve the X, Y position resolution.

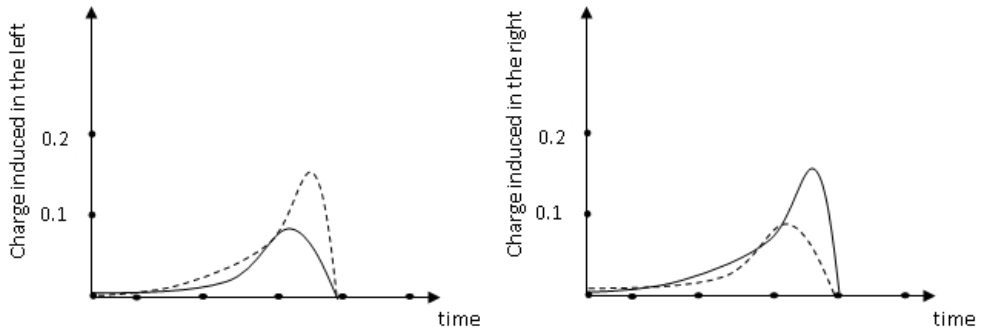

Figure 2.8: Weighting potentials of the right and the left pixel for two different interactions. The dashed line represent an interaction near the left pixel. The continuous line, an interaction near the right pixel

This algorithm simply compares the ratio between the induced signals (charges) in the neighboring pixels to find the position of interaction in the central pixel.

$$X = \frac{Q_r - Q_l}{Q_r + Q_l} \tag{2.30}$$

$$Y = \frac{Q_t - Q_b}{Q_t + Q_b} \tag{2.31}$$

Where Q_r, Q_l, Q_t and Q_b represent the charges created in the surrounding pixels.

2.8.6 Z dependence

The signal in the central pixel takes the form shown in figure 2.9. As the electron/hole pairs drift apart with the influence of the detector bias, they induce complementary

signals. If the electrons reach the anode first, the remaining holes continue to create an induced signal, but now at a lower rate of increase.

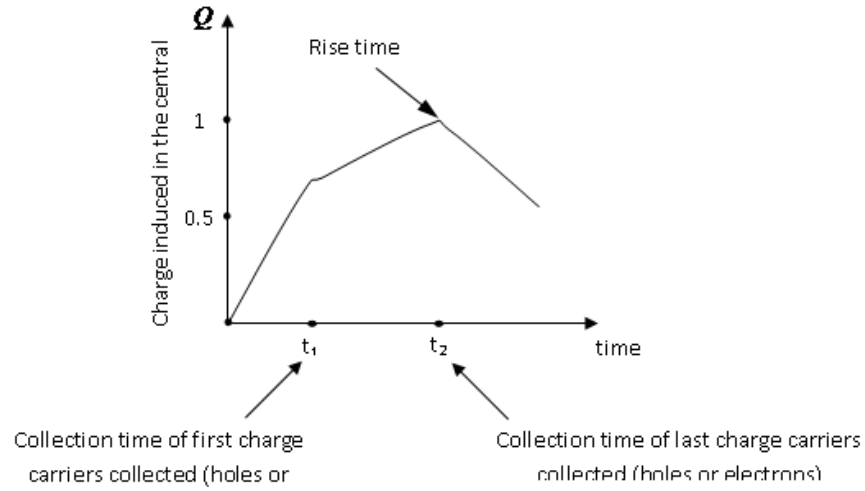

Figure 2.9: Pulse shape of induced charge in the pixel where the interaction happened

The depth information is linked to two factors: The rise time of the charge created in the central pixel where the interaction took place and the polarity of the induced signals in the surrounding pixels.

The rise time quantifies the time took the created charges (electrons and holes) to reach the electrodes. The velocity of electrons and holes at 80 Kelvin is almost equal for Ge. Therefore, because the rise time is equal to the collection time of the last charge carriers to be collected, the relationship between the depth (Z) and the rise time is a symmetrical function. In order to determine the depth information, the polarities of the induced signals can be used to eliminate the problem of this symmetry. The polarities are dependent on the type of charge carriers collected first.

Chapter 3

The UCL Compton Camera, the Readout Electronics and the Trigger System

3.1 Introduction

This chapter describes the UCL Compton camera and the DAQ system used to produce data for this thesis. First, a description of the UCL Compton camera is given starting with the physical dimensions and geometry of the Compton camera; followed by an explanation of the detector technology used to segment the Compton camera. Secondly, the readout electronics system which consists of gamma ray tracking 4 chan-

nels (GRT4s) cards, a Motorola VME PowerPC (PPC) card and a Linux PC running Multi Instance Data Acquisition System (MIDAS) software, are explained. Thirdly, the triggering system is described; it consists of the GRT4s cards, a fan in fan out NIM unit from CAEN Technologies Inc, a PHILIPS logic unit and the XVME260 relay card. Finally, the functioning of the system as a whole is described.

3.2 UCL Compton Camera

The UCL Compton camera was built by ORTEC in 2003 and consists of two HPGe detectors housed within the same cryostat together with their preamplifiers. Figure 3.1 shows a photograph of the UCL Compton camera; next to it on figure is a simplified diagram of the camera. Because the UCL Compton camera is made of HPGe, for the camera to operate at its best, a liquid nitrogen dewar is needed to cool down the germanium. Underneath it is a bank of preamplifiers (only 52 are provided). The HPGe Compton camera front and back detectors are at the bottom, underneath the preamplifiers.

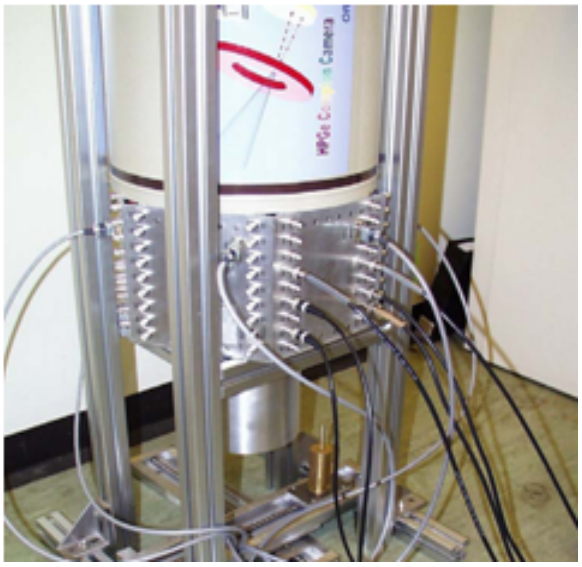

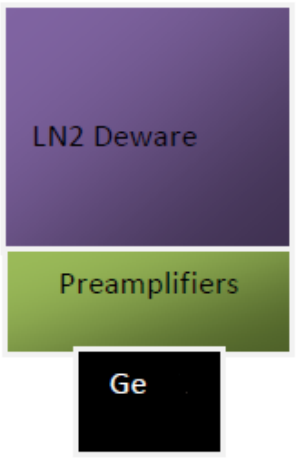

(a) Picture (b) UCL CC Block Diagram

Figure 3.1: UCL Compton camera

3.2.1 UCL Compton Camera Description

The UCL Compton camera is a pixellated high purity germanium (HPGe) camera developed for imaging 511 keV sources in nuclear medicine. It was built by ORTEC and consists of two planar HPGe detectors (the scatter and the absorption detector) housed within the same cryostat together with their preamplifiers. The scatter and absorption detectors have 152 and 25 $4 \times 4mm^2$ pixels respectively- a total of 177 pixels. The scatter detector has an active thickness of $5.4mm$ and an actual thickness of $6.1mm$ and the absorption detector has an active thickness of $10.6mm$ and an actual thickness of 11.3 (table 3.1). The two pixellated germanium detector planes are $97.7mm$ apart in the same vacuum housing. The scatter detector is a pixellated ger-

manium housed within a copper ring of an outer diameter of $10cm$, an inner diameter of $2.8cm$ and a thickness of $1.5cm$. A total of 152 $4 \times 4mm^2$ pixels are distributed in 8 blocks, of 18 or 20 pixels, around the ring. The absorption detector is a pixellated germanium consists of 25 pixels arranged in 5x5 of 4x4 mm2 pixels. The separation between the pixels, in both detectors, is $1mm$. Figure 3.3 represents a 2D cross secion and 3.2 is a 3D diagrams highlighting the camera's geometry and pixels arrangements (pixels in red are the pixels used to produce images for this thesis).

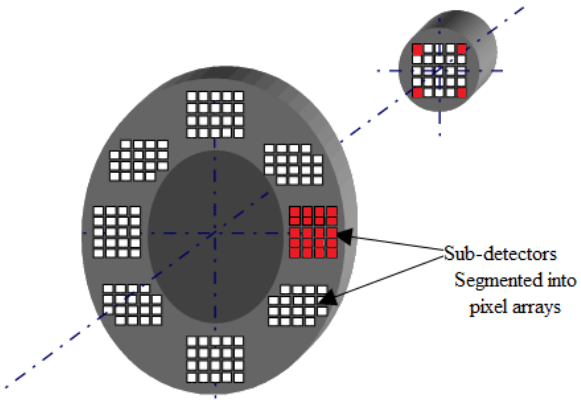

Figure 3.2: 3D diagram of the UCL Compton camera

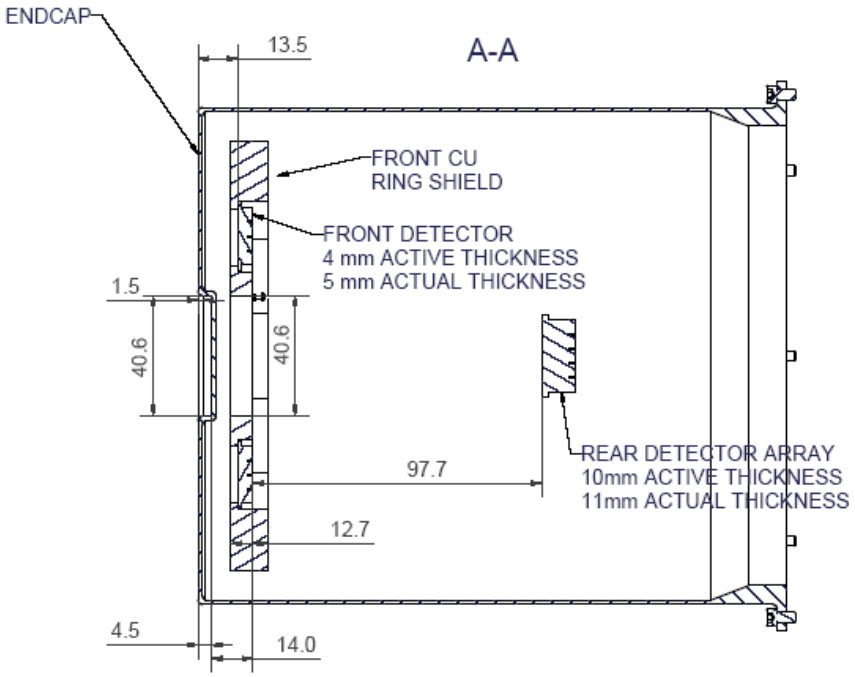

Figure 3.3: Cross section of UCL Compton camera

3.2.2 Geometrical Design

The original purpose of the geometrical arrangement of having a large front detector and a small diameter back detector is to optimize the spatial resolution of the camera by selecting a specific range of event angles (30 and 80 degrees). The camera was developed especially to image small source distribution or small organs like the thyroid. Because of this the approximate distance from the source (organs) to the front detector will be 5 cm. The selection of broader angles will maximize depth resolution in the image. This is due to the principle of image reconstruction in Compton cameras.

The front detector ring has an inner diameter of 6 cm and an outer diameter of

10 cm. Therefore for a point source at a distance of 5 cm from the camera placed on the central detector axis, gamma rays that are emitted in a cone between 30 and 45 degree will pass through the detector ring.

The distance between the front and back detector planes is 97.7 mm. The diameters of the detector planes and their separation means that a gamma ray emitted from a point source at a distance of 5 cm from the front detector along the central camera axis must scatter within the angular range of 40 to 80 degrees. This range will extend either way for a point source off centre or for an extended source. Differentiating the Compton equation with respect to angle shows that maximum energy deposition per unit angle occurs within an angular range of approximately 20 to 80 degrees. Translating this to the Compton camera principle means that angular measurement of the scattered photon is more accurate in this range.

3.2.3 Physical Detector Design

The UCL Compton camera is HPGe semiconductor pixellated into 4 by 4 mm pixel size. The space between the pixels is 1mm. The thickness of the different arrays is given in table 3.1. An array of pixels (there are 8 at the front and 1 at the back) has a continuous cathode and a pixellated anode (figure 3.4), and only the signals from the anode are read which will limit the options that can be used to enhance the depth of interaction as is seen in the previous chapter. The applied bias voltage at Vb is

Table 3.1: Active and actual thickness of all the array detectors

Detector	Front	Back
Active Depth (mm)	5.4	10.6
Actual Thickness	6.1	11.3

500V.

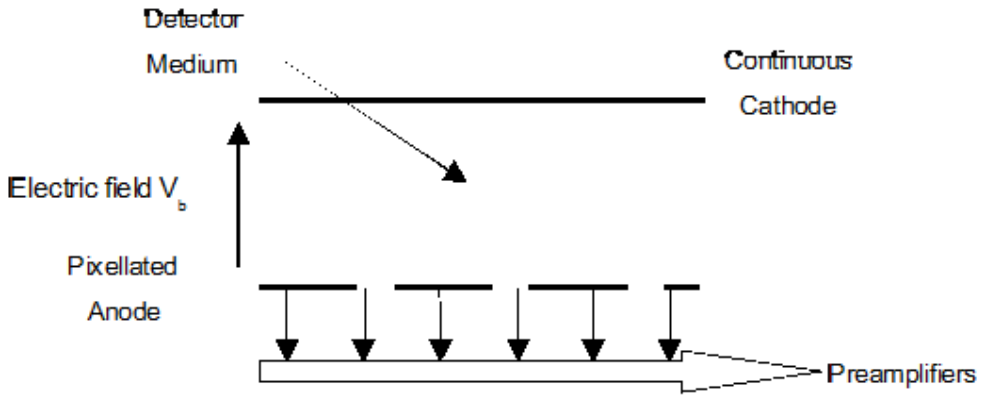

Figure 3.4: Detector design of the UCL Compton camera

3.2.4 Mini UCL Compton Camera

Due to limitation in the readout electronics (PPC's small memory of 64kb) only 20 pixels can be used. Therefore, choosing the best combination of pixels to operate as a Compton camera is important. This choice, most importantly, must allow to study the effects of enhancing the position sensitivity on images and hence the need to acquire signals from neighboring pixels of where an interaction happened. Another important aspect is choosing the pixels combination to give a variety of the cones directions on the image plane. The image plane was chosen underneath the front detector (Center

Right pixel array) at a distance of about 20mm from the front detector.

To be able to use the induced charges from the neighboring pixels to improve the x-y-z position sensitivity, two options, which fulfills the criteria to choose the best pixel combination explained above, are thought to be the best; use 4 pixels from the front and 16 pixels from the back detector or vice versa with the condition that the four pixels should be those of the corners of a cluster to have broader angles. Because the front detector is smaller than the back detector and has only 16 out of 20 pixels active (connected to the preamplifiers) which prevents using two of the corner pixels, the latter option, 4 pixels at the back and 16 on the front, was chosen.

3.3 Readout Electronics

The readout electronics (figure 3.5) consists of three main parts: Gamma Ray Tracking 4 channel (GRT4) cards [Lazarus, 2004], a Motorola VME PowerPC, and a Linux PC running MIDAS software for data acquisition. The PowerPC is the interface between the PC and the GRT4s. This provides a route for communication between pixels. The data is sent to the PC via an Ethernet protocol, where it is stored for offline processing using IDL software.

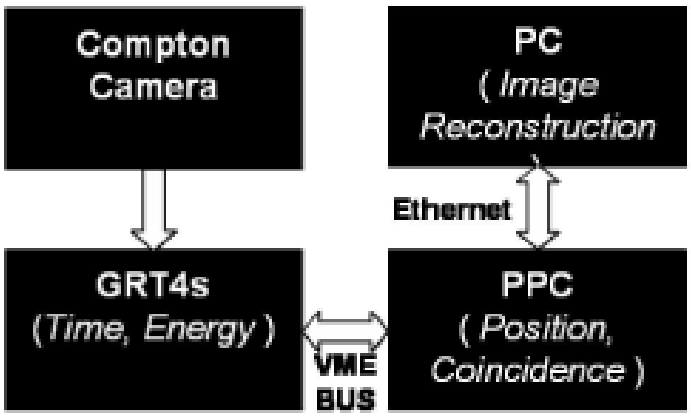

Figure 3.5: Readout electronics diagram and the trigger system

The Linux PC controls the readout electronics using MIDAS software (Multi Instance Data Acquisition System). It is a software developed by Daresbury laboratory UK for data acquisition and controls of the POWERPC,the GRT4 cards and data acquisition. Data processing was carried out using the Interactive Data Language (IDL) from Research System Incorporation.

3.3.1 Gamma Ray Tracking 4 Channel (GRT4)

The GRT4 card (Gamma-Ray Tracking 4 channel) was designed for the UK Gamma-Ray Tracking and Digital Pulse Processing project (a joint research project between CCLRC Daresbury Laboratory, University of Liverpool and University of Surrey). The aim was to do gamma ray tracking. The GRT4 was designed for nuclear physics applications, characterization scanning and for in-beam tests [Lazarus, 2004].

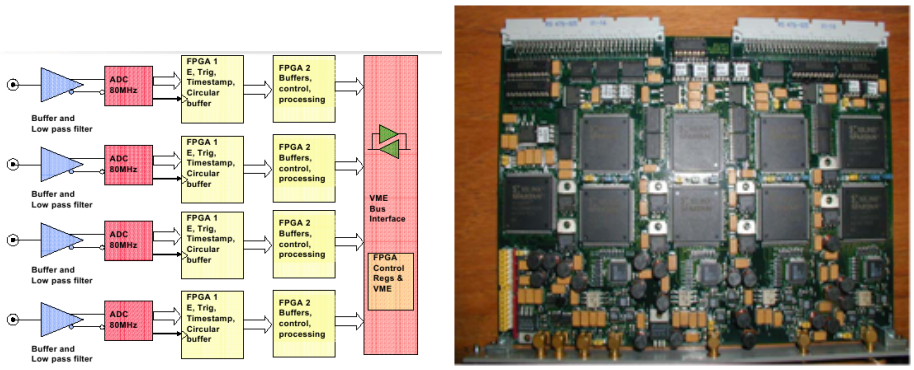

(a) Block diagram of the GRT4 (b) GRT4 picture

Figure 3.6: GRT 4 internal block diagram and a picture

Figure 3.6a highlights the different parts of a GRT4 card, and figure 3.6b shows a photograph of the card. The GRT4 card has four channels operating in parallel. Each channel has an SMA input terminated by 50ohms internally, an amplifier of gain 2, a 40MHz low pass filter and a 14 bit 80MHz (12.5ns sampling time) bipolar flash ADC (AD6645 from Analog Devices) with peak to peak range 1.1V so the input limit is 550mV. There are two 200k gate Xilinx Spartan2 field programmable gate arrays (FPGA) per channel for data processing. The first FPGA contains (figure 3.7) a circular buffer (6.4us) with programmable pretrigger register delay (controlled from the Linux PC using MIDAS), a digital self trigger algorithm; a Constant Fraction Discriminator (CFD), and an energy determination algorithm, Moving Window Deconvolution (MWD). Each trace in this buffer is tagged with a 16-bit header (eight ID bits are programmable, eight bits are the trigger counter), and a 48-bit time stamp (12.5 ns/bit) when the trigger occurs [Lazarus, 2004]. The second FPGA manages

the VME bus communication between the GRT4 and the PPC.

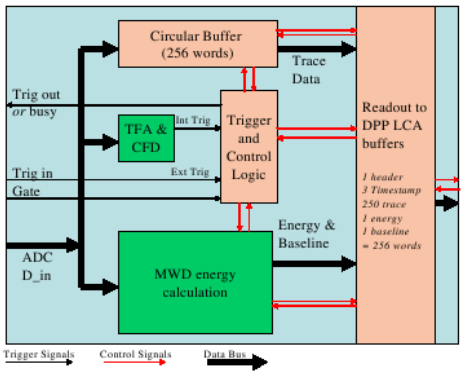

Figure 3.7: A diagram shows the different algorithms implemented in a GRT4 channel's first FPGA

Energy Measurements

The MWD energy measurement is done online inside the first FPGA. The MWD has a set of parameters that must be optimized for any given detector and are programmable via the MIDAS software. Figure 3.8a shows the GUI from which the parameters should be entered. The parameters are:

- Clock frequency- fixed (80MHz)
- Decimation factor- fixed (4)
- Shaping time- programmable 0 to 12.8us
- Peaking time2- programmable 0 to 12.8us
- Peak separation- programmable 0 to 800us

- Decay time constant (PZ)- programmable nominally 50us
- Peak sample time- programmable 0-800us
- Baseline update time- programmable 0-12.8us
- Baseline average- programmable 0-16, (bits 4-7 ignored)
- Mode- should normally be 0 (other values are 1,2,3)

Figure 3.8 explains the meaning of some of the parameters. For more details on how to set these parameters refer to the GRT4 manual.

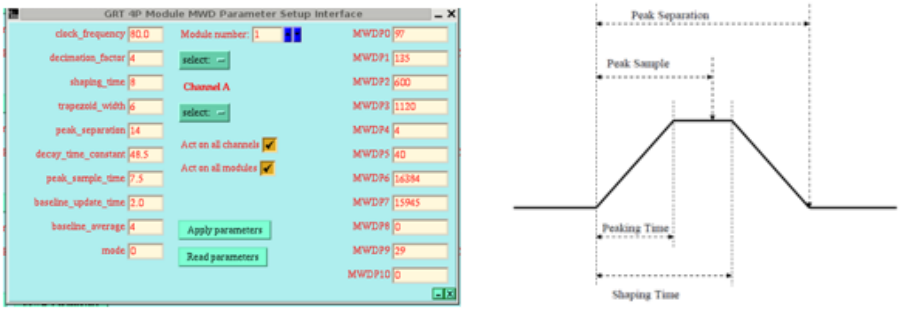

(a) MIDAS GUI shows the setting of the MWD parameters

(b) Trapzoidal explanation

Figure 3.8: MWD parameters and the meaning of its parameter

GRT4 Modes

The GRT4 has two modes of operation: oscilloscope mode and processing mode.

Oscilloscope mode: On this mode the signals from the camera are just digitized and stored on the PC. In this case all the traces are read out to a PC and stored for

offline analysis and algorithm development. The traces can be replayed many times to fine-tune algorithms. In this mode the PC is used to perform online analysis to extract energy spectra and show rise time distribution plots in real time so that results can be visualized while data are written to the PC.

Processing mode: Running in this mode pulse processing is done on board and a small part of the digitized trace is sent out along with the derived parameter(s). This would normally function by determining the energy from a trace length of about 10us (800 samples) and then passing on the energy and a shorter trace with just the leading edge of the pulse (250 samples, 3.125us) for offline pulse shape analysis or analysis in the second FPGA. The processing mode was used to obtain the results for this thesis.

3.3.2 MIDAS Software and the PowerPC

MIDAS is the software which manages all the DAQ operations. It runs on a Linux PC and at start up it loads a number of routines into the PPC; these routines manage the GRT4s and the XVME260 relay card via a VME bus. The communication between the PC and the PPC is via an Ethernet communication. Using the GUI of MIDAS, all the programmable registers of the GRT4 can be accessed and configured as required. The GRT4 uses one common data bus internally to access registers and also to transfer data between the 2 FPGAs. The two most important registers are the Pretrigger

Register and the ADC CTRL Register. The pretrigger register controls the length of the trace before the start of the interaction when the external or internal trigger is activated. This has to be long enough to account for the delay of the electronics. The ADC CTRL register controls individual channel's signal polarities (positive in the case of the UCL Compton camera) and source of trigger (internal or external).

3.3.3 Trigger System

The GRT4 can be triggered externally from a common trigger or internally from the CFD in each channel. This is selected by the ADC Trigger Register which can be programmed using the GUI within MIDAS. The GRT4 can deal with either positive or negative inputs, however the logic must be programmed to tell it which to expect both for trigger and for MWD energy calculation. The signal polarity is selected in the ADC Trigger Register..

The triggers (internal or external) may optionally be gated by the front panel gate input. Each channel has its own enable/disable bit, but these cannot all be programmed at once, so if the enable/disable bit in the ADC Control registers is used to control acquisition, then there is a delay from the first channel enable to the final channel enabled determined by the VME write times. To overcome this with common external triggers the GRT4 common trigger input is wired via an XVME260 VME relay card which is only enabled after the last channel enable.

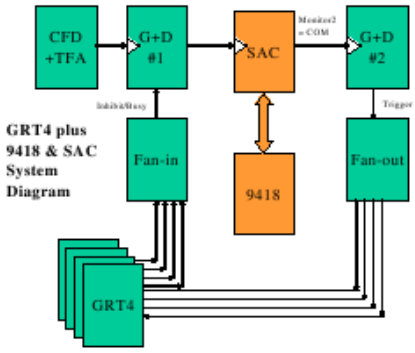

Figure 3.9: Trigger system used with the UCL Compton camera and the DAQ system

The GRT4 cards have a single fast NIM output which can be programmed to be either Trigger Out or Inhibit/Busy. The Inhibit/Busy signal is used for flow control when a common external trigger is in use. The Inhibit/busy signals are fanned in to the inhibit signal on a NIM gate and delay card. The diagrams (figure 3.9) show the trigger system used with DAQ and the UCL Compton camera. The GRT4s are programmed using the ADC Trigger Register to send a trigger out signal if an interaction in one of the triggering channels occurs. Therefore, all the GRT4s Trigger Out outputs are connected to the Fan In (from CAEN), and into the Philips gate and delay NIM unit (G+D 1 and 2). The relay card, the XVME260, which is controlled by the PPC via the VME bus is switched on only if all the GRT4 cards are enabled and ready to accept another trigger.

3.3.4 DAQ System Mode of Operation

Gamma rays interactions inside the pixels generate charges which are conditioned and preamplified. The signals from the preamplifiers are then sent to the GRT4 cards for digitization and energy measurements. Data is then sent to the PPC to be sent via an ethernet connection to a PC running MIDAS software where it is stored for off-line analysis. The off-line analysis implements time and energy coincidence, alternative energy measurements, gamma ray position determination, image reconstruction and finally image filtering algorithms on the back-projection images. Figure 3.10 shows a simplified diagram of the whole system.

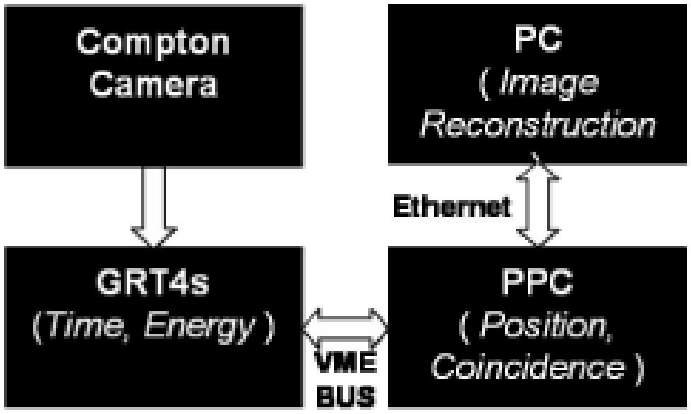

Figure 3.10: a diagram shows the UCL Compton camera and, DAQ and the trigger system

The four back detector pixels are connected to channel D of four GRT4s, a total of 5 cards was used to operate the Mini-Compton camera explained earlier in this chapter. The remaining 16 pixels from the front detector were connected to the

remaining GRT4s channels. The back detector channels were configured to trigger internally and send a trigger out signal. The front detector pixels are configured to expect an external trigger through the Trigger In inputs of the GRT4 cards. The DAQ system sends data to the PC in the format explained below where each event contains 20 traces from each pixel and their corresponding energy.

Data Format

A simplified description of the data format is given in this section; however, for more details refer to (MIDAS web page). Each file has a number of events where an event represents the data acquired from all the channels each time a trigger is activated. On our case an event constitutes of 20 channels (pixels), and this is due to a limitation on the electronics. Each event has a header specifies the number of channels within it (20 in our case); after that follows the first channel data: it starts with a header that includes an identifier referencing that channel, and after that follows the trace of that channel (250 samples) and at the end there is a tale header which contains the MWD energy. After that follows the 2nd channel, 3rd until the 20th channel. The events end with a tale header.

3.4 Coincidence Algorithm

The DAQ gives no indication of whether an event originates from coincident photons; in fact, the events provided are not always events, as we will see in the following sections. The readout electronics does not indicate which pixels the interactions took place nor does it give the time of the interactions. So the coincidence algorithm determines where the interactions happened (position of interactions), determines the time of each interaction and finally checks whether the time difference between the two interactions falls within the acceptable window to be considered as a good event.

3.4.1 Definitions

An event

An event is a data packet that contains all the traces acquired after each readout electronics trigger (the number of traces is 20 which corresponds to the pixels used).

Good Event

Two interactions from the same photon; one in the front and one in the back detector, where the time difference is within the acceptable range; in theory there should not be any difference in time between the two interactions because the photons travel with the speed of light, but due to detector design and charge collection, and mainly to readout electronics trigger delay, a delay between the coincident interactions exist.

Possible Good Event

A possible good event is any event which contains an interaction in the back and one in the front (the time is not considered at this point).

False Event

Is an event with one interaction in the back detector and none in the front (the interaction in the back originated from a direct hit from the source).

3.4.2 Interaction Position

To find the position of an interaction, the algorithm finds the amplitude of the trace and if it is above a threshold (which is twice the amplitude of the noise) the algorithm steps 20 ADC channels and finds the amplitude of the trace at that point; if it is above the noise, it is an interaction, if it is not, the trace is ignored. The algorithm moves to next trace until it finds where the interaction happened. When the pixels where the interactions happened is defined, the algorithm then applies the x, y and z position sensitivity improvements as explained in details in the position sensitivity (chapter 5).

3.4.3 Energy Window

The coincidence algorithm used to produce the images of this thesis does not apply an energy window; it does, however, reject the events where the sum of the front and the back detector exceeds 662kev (the energy used to produce images). Using an energy window would increase the confidence of the coincidence algorithm, but because about 99% of photons are not absorbed in the back detector, it is impossible to get enough events for the reconstruction algorithms.

3.5 Conclusion

Although, the UCL Compton camera has 177 pixels of which 25 are in the back detector, only 20 pixels were used (16 from the front and 4 from the back) to produce the images for this thesis due to limitations on the readout electronics. The four pixels at the back are configured to trigger the camera; the trigger occurs whenever there is an interaction in one of the four pixels in the back detector.

The GRT4 implements the MWD algorithm online to calculate the energy of incident gamma rays. This energy is provided with the data sent to the PC at the back of each trace's pixel. Also for each pixel a trace of 250 samples in length is provided. In the next chapter, in addition to the given energy, another two alternative energy algorithms are implemented to study the effects of energy resolution on images. The traces of the pixels are used to find the coincident photons by using a time window.

Chapter 4

Energy Resolution Optimization

Data from the camera is provided by the DAQ system in the format described in section (3.3.4) where traces of 3.125us and MWD energy value are given for each pixel used. Although the energy is provided, to study the effects of energy resolution on images from the UCL Compton camera, two offline algorithms were developed; they are named the UnFiltered and the Filtered energy enhancement algorithms. Another reason on developing these two algorithms is to investigate the possibility of getting good energy resolution using short traces (1us as opposed to MWD which integrates for much longer times). This can improve the efficiency of the Compton camera and reduce dead time of the electronics, providing of course that the achievable energy resolution using such algorithms does not affect the spatial resolution for the given application.

To obtain the energy resolution for the three algorithms, experiments were con-

ducted using Cs137, Ba133 and Am241 gamma ray sources. These experiments were conducted for each pixel of the camera's 52 active pixels (pixels which are connected to preamplifiers).

The UnFilterd algorithm simply measures the amplitude of a pulse from the camera which is not filtered as shown on figure 4.1 in black. The energy resolution at 356kev is 4%. The second enhancement algorithm (named Filtered) uses a ready to use function of IDL software. The function is the SMOOTH function which is an implementation of the boxcar average algorithm with user controlled width (w).

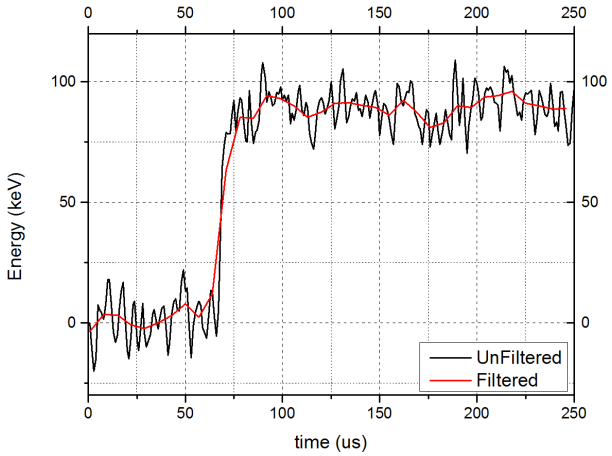

Figure 4.1: A pulse from the camera, in black is the unfiltered pulse and in red is the filtered pulse

To achieve the best energy resolution that the SMOOTH function could achieve, the width W was varied and for each value the energy resolution was measured at 356kev. The graph on figure 4.2 shows the relationship between the width w and the energy resolution. From the graph we can conclude that the energy resolution gets

better as the width increases up to 30.

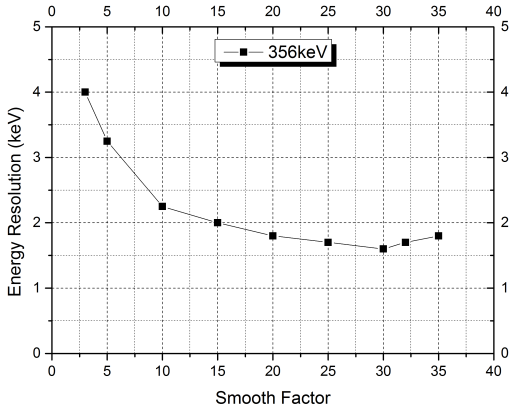

Figure 4.2: Effects of the smooth factor on energy resolution

4.1 Moving Window Deconvolution Energy Measurements

The moving window deconvolution (MWD) (see section 2.6.3 and 3.3.1) is implemented in the GRT4s FPGAs and the energy measurements are done in real time. The MWD use a set of parameters which are set by the user via the MIDAS software on the PC. The parameters selection affects directly the energy resolution. Figure 4.3 shows an energy spectrum using the MWD algorithm.

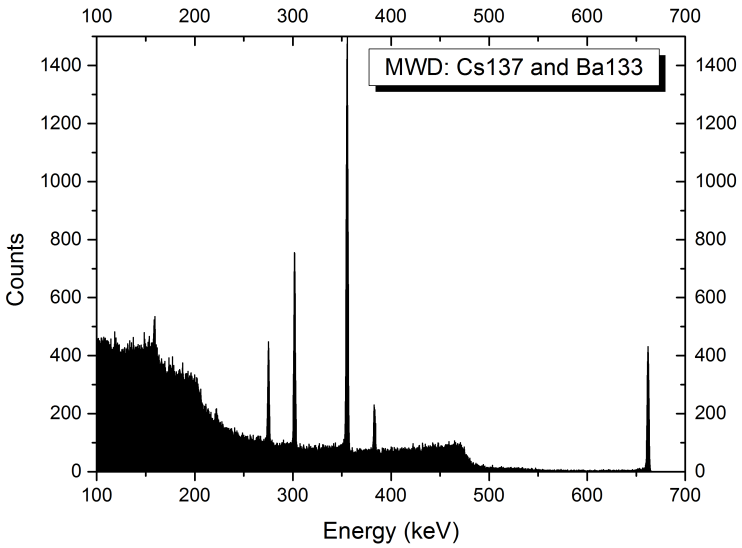

Figure 4.3: MWD algorithm energy spectra

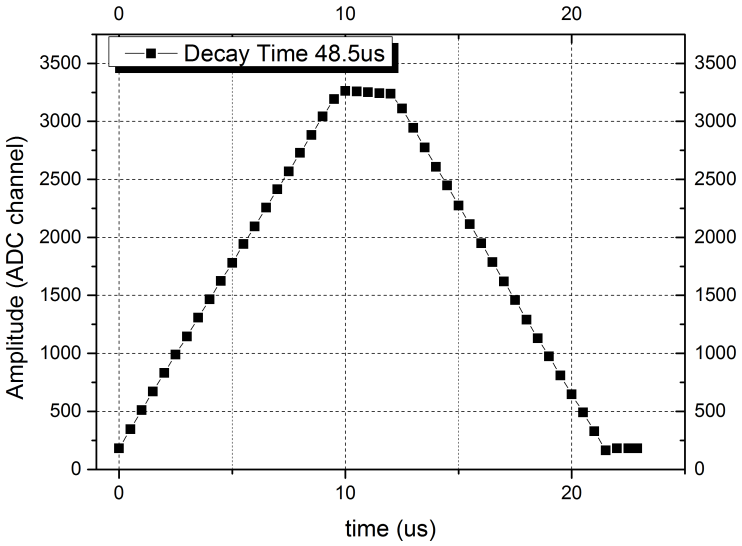

Figure 4.4: Trapezoid plot

To choose the best parameters, shaping time and flat top width, for the UCL

Compton camera, a set of experiments were conducted. The experiments were designed to vary the flat top width from 1us up the maximum value possible for each shaping time. Shaping times were set from 1.7us to the maximum of 12.7us. Figure 4.4 represents the trapezoid output of the MWD algorithm for a Decay time of 48.5us. This is the value which was used for the UCL Compton camera. Results of the relationship between the shaping time, flat top width and energy resolution are presented in the graphs of figure 4.5 and 4.6

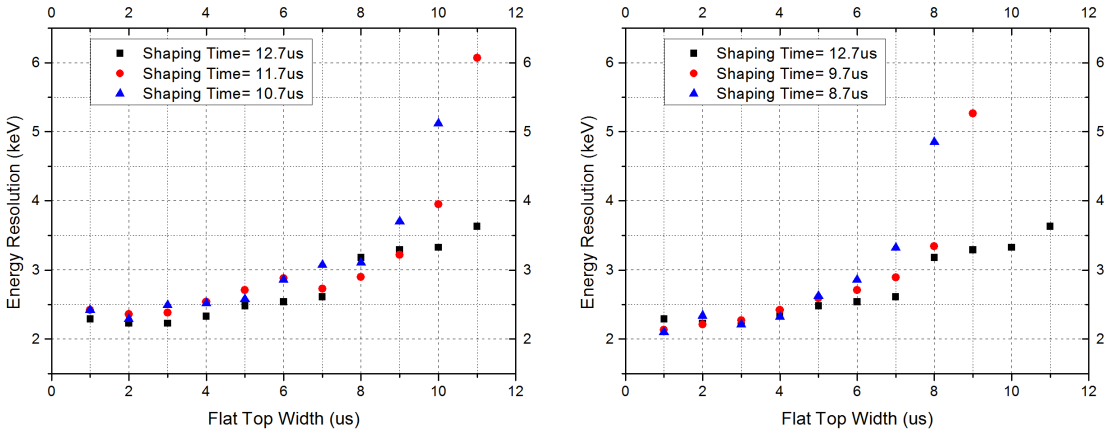

(a) Shaping time 10.7 to 12.7us

(b) Shaping time 8.7, 9.7 and 12.7 us

Figure 4.5: Effects of shaping time (8.7us to 12.7us) and flat top width on the energy resolution of the UCL Compton camera

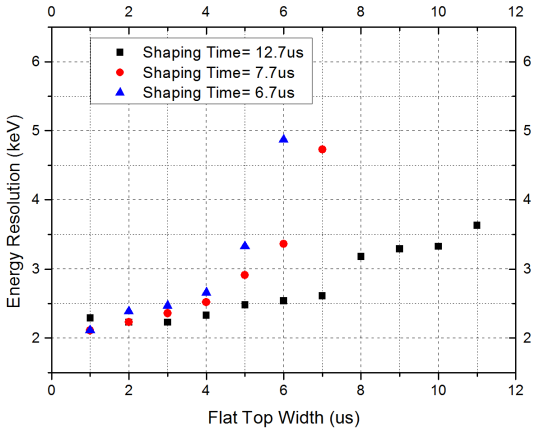

(a) Shaping time 6.7, 7.7 and 12.7 us

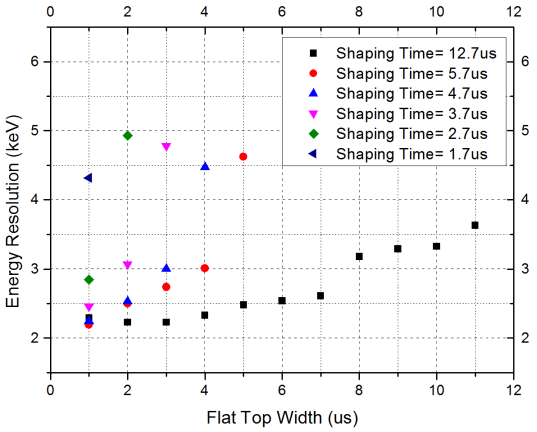

(b) Shaping time 1.7 to 5.7 and 12.7 us

Figure 4.6: Effects of shaping time (1.7us to 7.7us) and flat top width on the energy resolution of the UCL Compton camera

From the graphs of 4.5 and 4.6, the shaping time of 12.7us to 6.7us gives almost the same energy resolution for flat top widths of 2 to 4 us. For shaping times below 6.7us, the energy resolution gets worse as the shaping time decreases and the flat top width increases. The MWD parameters that were chosen for the camera were 12.7us shaping time and 2.6us flat top width.

4.2 Energy Resolution Results

Energy resolutions of all the active pixels of the UCL Compton camera were measured for a range of gamma ray energies using an analog NIM amplifier and the three energy resolution algorithms: MWD, Filtered and UnFiltered algorithms. The energies at which the energy resolution was measured were 32keV, 60keV, 80keV, 276keV 303keV, 356keV, 384keV and 662keV. The energy resolution at 662keV for the 20 pixels used

to produce images for this thesis is given in the table of figure 4.7 in percentages and 4.8 in keV. The table presents energy resolution from the three algorithms as well as results from using an analog shaping NIM amplifier.

Pixel	NIM (%)	MWD (%)	Filtered (%)	UnFiltered (%)
CR11	0.30	0.31	0.73	1.33
CR12	0.29	0.34	0.68	1.34
CR14	0.27	0.33	0.70	1.01
CR21	0.31	0.34	0.66	1.25
CR22	0.30	0.37	0.70	1.32
CR23	0.29	0.50	0.87	1.38
CR24	0.30	0.44	0.75	1.29
CR33	0.27	0.34	0.72	1.28
CR34	0.29	0.34	0.66	1.22
CR42	0.31	0.32	0.74	1.53
CR43	0.29	0.32	0.76	1.29
CR44	0.29	0.45	0.62	1.42
BC11	0.35	0.40	0.70	1.33
BC15	0.31	0.31	0.72	1.34
BC51	0.36	0.35	0.71	1.29
BC55	-	0.50	0.71	1.38

Figure 4.7: Energy resolution at 662keV (given in percentage) for all the CR and BC pixels used to produce images

Pixel	NIM (keV)	MWD (keV)	Filtered (keV)	UnFiltered (keV)
CR11	1.96	2.03	4.85	8.83
CR12	1.93	2.27	4.47	8.88
CR14	1.82	2.20	4.66	6.71
CR21	2.04	2.28	4.39	8.27
CR22	2.01	2.42	4.61	8.77
CR23	1.94	3.33	5.79	9.15
CR24	1.96	2.93	4.98	8.54
CR33	1.82	2.28	4.35	8.45
CR34	1.92	2.28	4.87	8.09
CR42	2.03	2.12	5.04	10.13
CR43	1.93	2.15	4.47	8.51
CR44	1.91	2.99	4.10	9.40
BC11	2.33	2.66	4.64	8.78
BC15	2.05	2.08	4.77	8.90
BC51	2.41	2.33	4.67	8.52
BC55	3.01	3.30	4.68	9.13

Figure 4.8: Energy resolution at 662keV (given in keV)for all the CR and BC pixels used to produce images

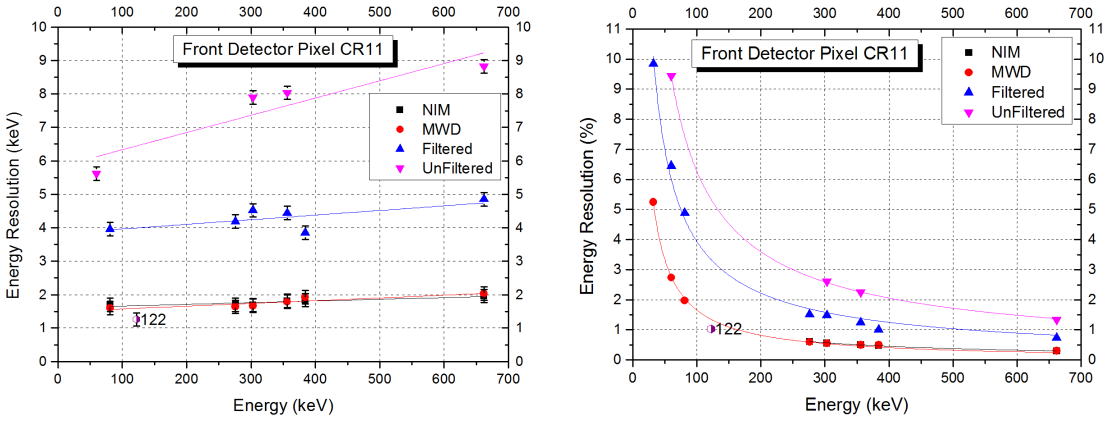

(a) Energy resolution expressed in keV (b) Energy resolution expressed in percentage

Figure 4.9: Energy resolution of CR11 pixel from the front detector for different gamma ray energies

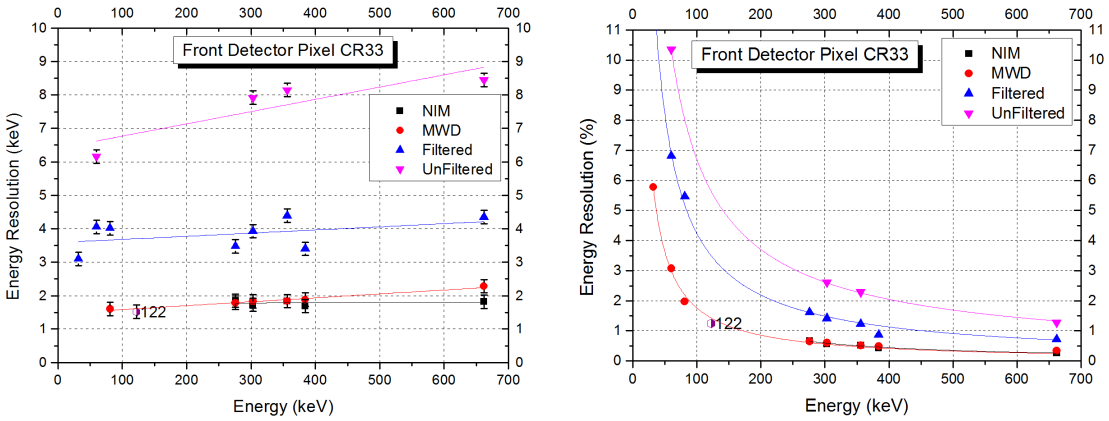

(a) Energy resolution expressed in keV (b) Energy resolution expressed in percentage

Figure 4.10: Energy resolution of CR33 pixel from the front detector for different gamma ray energies

An example of energy resolution results of four pixels, two from the front and two from the back detectors is given in the graphs of figures 4.9, 4.10, and 4.11, 4.12. The energy resolutions done by ORTEC were done only for the energy 122keV and are marked in the graphs with the label 122. The MWD algorithm gives close readings of energy resolutions of the NIM analog shaping amplifier, and from the interpolation of the energy resolutions on the graphs, the MWD and the NIM measurements seem to give very close values to the ones provided by ORTEC.

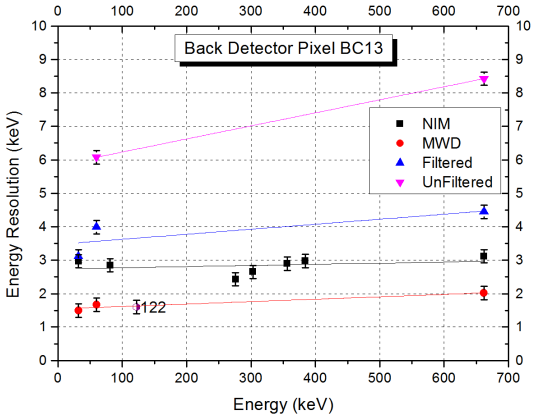

(a) Energy resolution expressed in keV

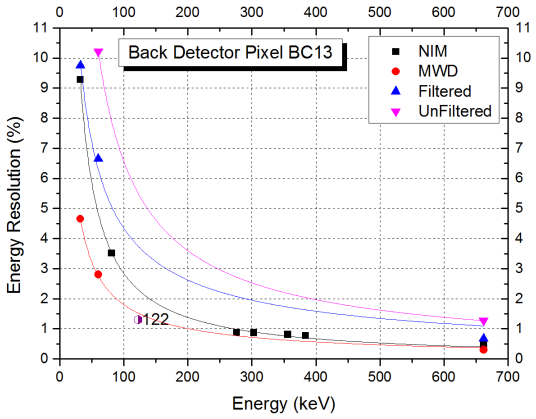

(b) Energy resolution expressed in percentage

Figure 4.11: Energy resolution of BC13 pixel from the back detector for different gamma ray energies

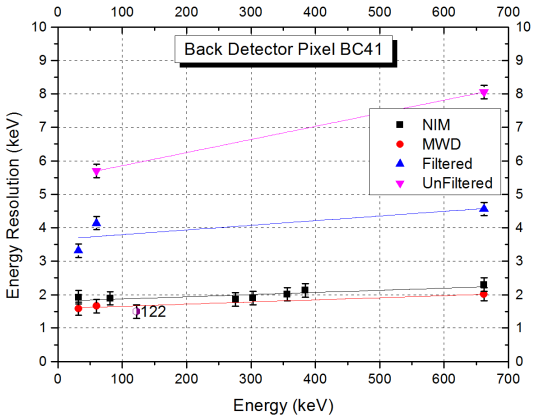

(a) Energy resolution expressed in keV

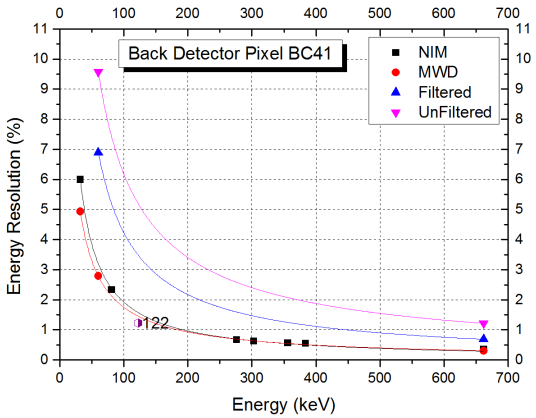

(b) Energy resolution expressed in percentage

Figure 4.12: Energy resolution BC41 pixel from the back detector for different gamma ray energies

The energy resolution of the UCL Compton camera, even though is made of a HPGe, does not much the predicted energy resolution expected from a high purity germanium detector. Its energy resolution is about a factor of two worse than a commercially available germanium detector. Possible reasons for this is that the

preamplifiers for the UCL Compton camera are installed faraway from the pixels which will increase the noise, as the preamplifiers always are connected very close to the detectors.

Appendix A presented all the results of energy resolution for all the UCL Compton camera active pixels from the BC, CR and LC arrays as well as the amplitude noise measurements done from the back detector.

4.3 Energy Uncertainty Contribution to Angular and Spatial Resolution

The effects of energy resolution of the UCL Compton camera on the angular and spatial resolutions were studied using the mathematical models equations developed in section (2.7.1). The effects of energy resolution were plotted for the following energies: 662keV, 511keV, 364keV and 140keV. The graphs of figure 4.13 were used to interpolate the unknown energy resolutions of 511keV, 364keV and 140kev because the measurements of energy resolutions in section (4.2) were not done for these energies.

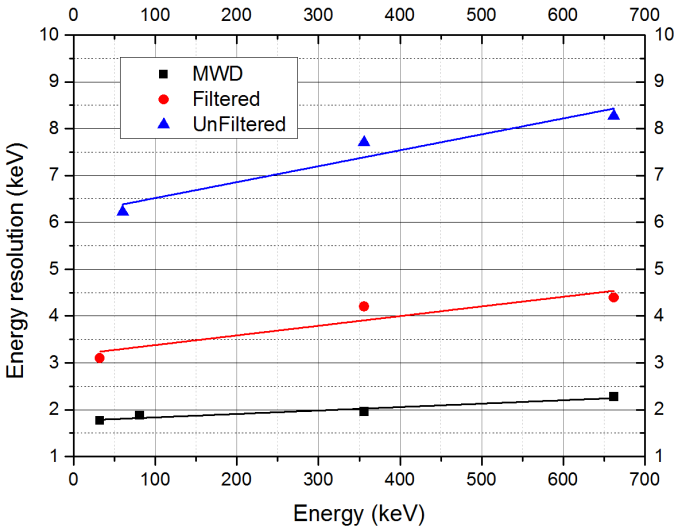

Figure 4.13: Energy Resolution for the UCL HPGe Compton camera given for the MWD, Filtered and UnFiltered Algorithms

4.3.1 Energy Resolution Contribution

For an incident energy of 662kev, the angular and spatial resolution for energy resolutions of MWD, Filtered and UnFiltered are shown in figure 4.14. In the case of energy resolution of the MWD, for scattering angles between 5° and 105° the angular resolution is less than 1° and the spatial resolution is below 1mm; for scattering angles below 5° the angular resolution goes up to 7° and the spatial resolution goes up to 7mm; and for scattering angles above 105° the angular resolution goes up to 100° and the spatial resolution up to 100mm. In the instance of energy resolution of the Filtered, for scattering angles between 15° and 75° the angular resolution is below 1° and the spatial resolution is below 1mm; for scattering angles below 15° the angular

resolution goes up to 10° and the spatial resolution up to 10mm; and for scattering angles above 75° the angular resolution goes up to 100° and the spatial resolution to 100mm. For UnFiltered algorithm, for scattering angles between 0° and 140° the angular resolution is from 1° to 10° and the spatial resolution is between 1mm and 10mm.

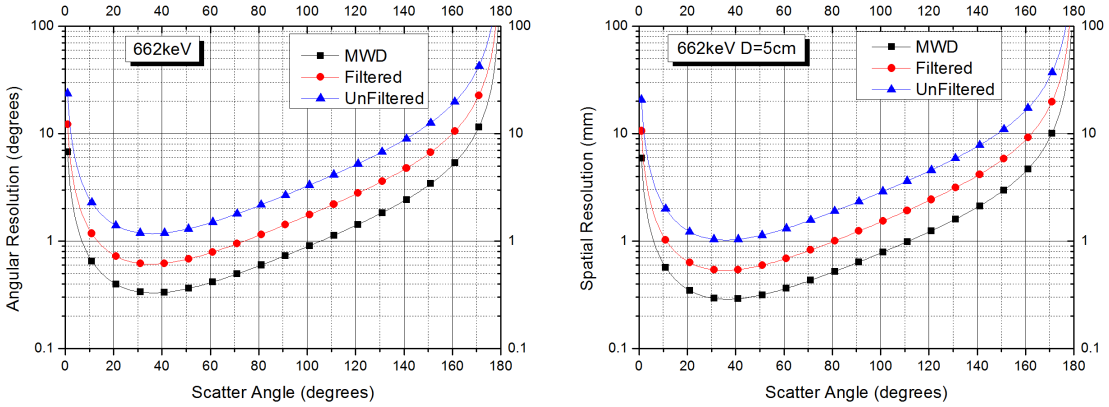

(a) ER effects on angular resolution at 662keV (b) ER effects on Spatial resolution at 662keV

Figure 4.14: Effects of Energy Resolution on angular and spatial resolution for a 662keV gamma ray source

Figure 4.15 shows the angular and spatial resolutions for an incident energy of 511keV and energy resolutions of MWD, Filtered and UnFiltered. For scattering angles between 10° and 100, between 20° and 60°, and between 5° and 140° the angular and spatial resolution is below 1° and below 1mm, below 1° and below 1mm, and from 1° to 10° and from 1.5mm to 10mm for MWD, Filtered and UnFiltered algorithms respectively.

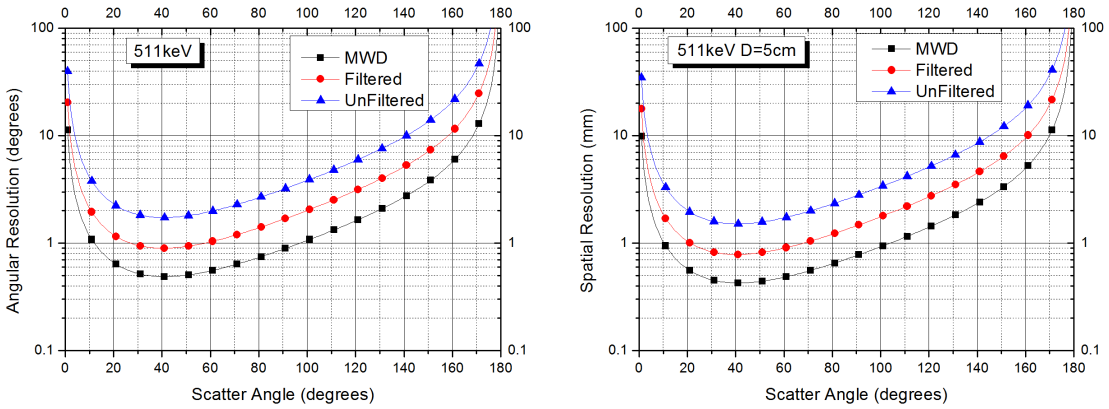

(a) ER effects on angular resolution at 511keV (b) ER effects on Spatial resolution at 511keV

Figure 4.15: Effects of Energy Resolution on angular and spatial resolution for a 511keV gamma ray source

Figure 4.16 depicts the angular and spatial resolution for an incident gamma ray of 364keV for the three energy enhancements algorithms. For scattering angles between 10° and 120°, the angular resolution is between 0.8° and 2° and the spatial resolution is between 0.7mm and 2mm for MWD algorithm; the angular resolution is between 1.5° and 4° and the spatial resolution is between 1.3mm and 3mm for Filtered algorithm; the angular resolution is between 3° and 6° and the spatial resolution is between 2.5mm and 6mm for the UnFilterd algorithm.

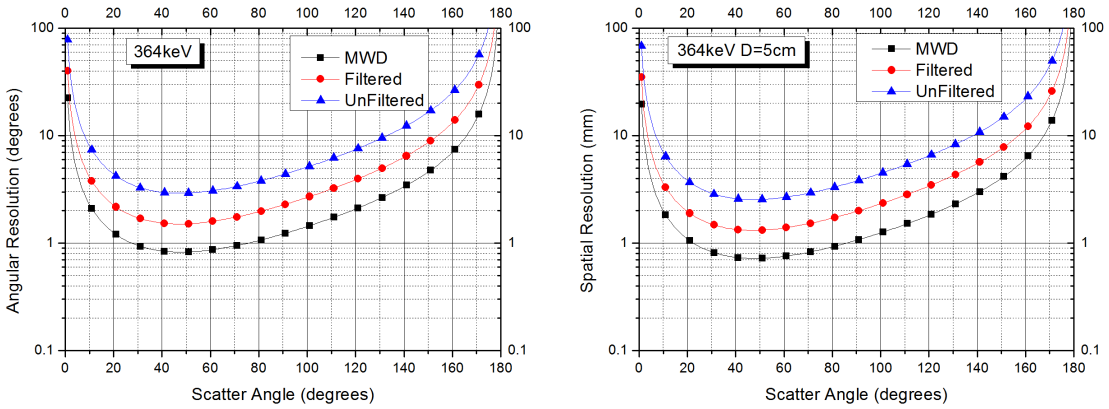

(a) ER effects on angular resolution at 364keV (b) ER effects on Spatial resolution at 364keV

Figure 4.16: Effects of Energy Resolution on angular and spatial resolution for a 364keV gamma ray source

For an incident gamma ray energy of 140keV and energy resolutions of the three energy resolution algorithms, angular and spatial resolution related to these camera parameters are plotted in figure 4.17. For scattering angles between 15° and 145°, the angular resolution and the spatial resolution is between 4° and 10°, and between 3mm and 10mm respectively for MWD; the angular resolution and the spatial resolution is between 7° and 11°, and between 6mm and 11mm respectively for Filtered; the angular resolution and the spatial resolution is between 10.5° and 13°, and between 10.2mm and 13mm respectively for UnFiltered algorithm.

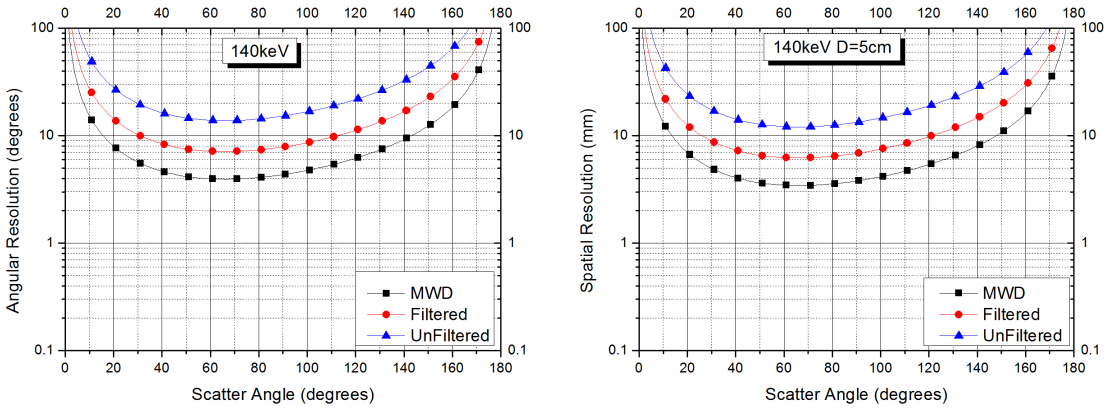

(a) ER effects on angular resolution at 140keV (b) ER effects on Spatial resolution at 140keV

Figure 4.17: Effects of Energy Resolution on angular and spatial resolution for a 140keV gamma ray source

4.3.2 Incident Energy Contribution

Figure 4.18 shows the effects of the incident gamma ray energy for MWD energy resolution and gamma ray energies of 662keV, 511keV, 364keV and 140keV. For 662keV gamma ray source and scattering angle between 5° and 110°, for 511keV and scattering angle between 10° and 100°, for 364keV and scattering angle between 20° and 90°, for 140keV and scattering angle between 15° and 150°; the corresponding spatial resolutions are below 1mm for 662keV, 511keV and 364keV; however, for 140keV the spatial resolution is between 2mm and 10mm.

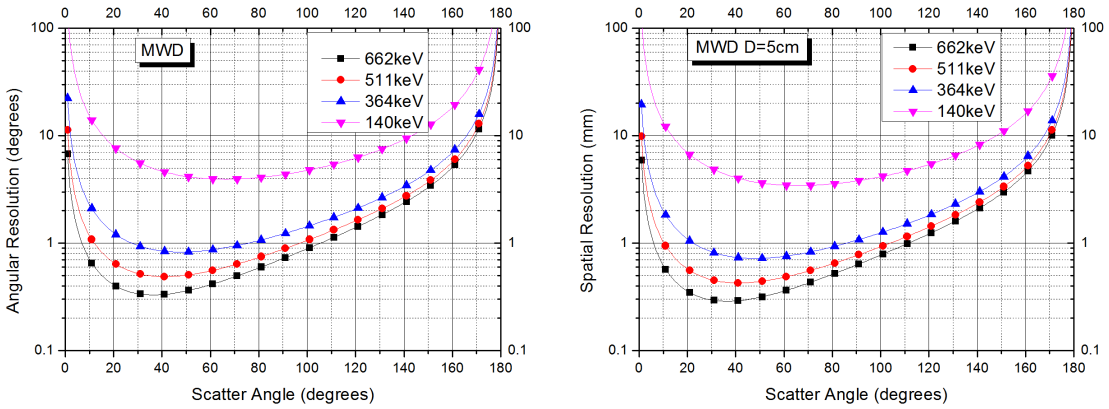

(a) Eg effects on angular resolution for MWD (b) Eg effects on spatial resolution for MWD

Figure 4.18: Effects of Incident Energy on angular and spatial resolution for MWD and D=5cm

Figure 4.19 shows the effects of the incident gamma ray energy for Filtered algorithm energy resolution and gamma ray energies of 662keV, 511keV, 364keV and 140keV. For 662keV gamma ray source and scattering angle between 10° and 80°, for 511keV and scattering angle between 20° and 70°, for 364keV and scattering angle between 20° and 90°, for 140keV and scattering angle between 25° and 120°; the corresponding spatial resolutions are below 1mm for 662keV and 511keV and between 1mm and 2mm for 364keV; however, for 140keV the spatial resolution is between 2mm and 10mm.

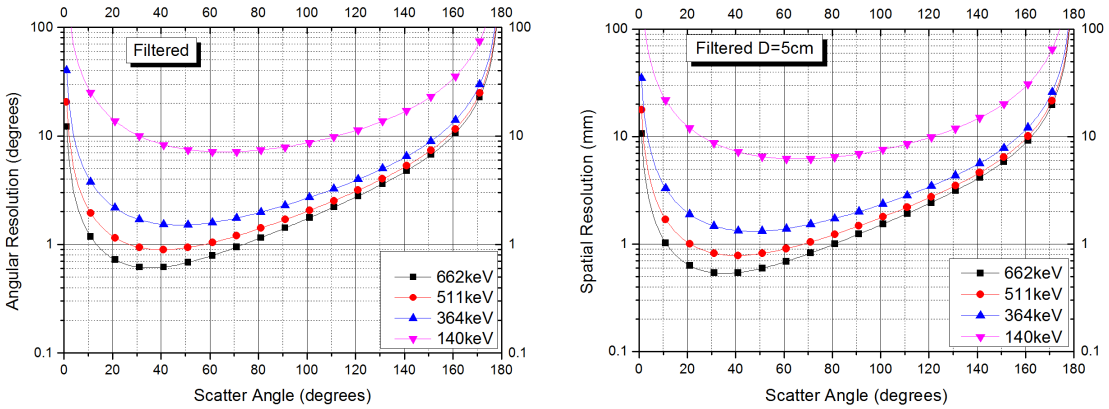

(a) Eg effects on angular resolution for Filtered (b) Eg effects on spatial resolution for Filtered

Figure 4.19: Effects of Incident Energy on angular and spatial resolution for filtered and D=5cm

Figure 4.20 shows the effects of the incident gamma ray energy for Filtered algorithm energy resolution and gamma ray energies of 662keV, 511keV, 364keV and 140keV. For 662keV gamma ray source and scattering angle between 10° and 85°, for 511keV and scattering angle between 10° and 100°, for 364keV and scattering angle between 10° and 120°, for 140keV and scattering angle between 10° and 160°; the corresponding spatial resolutions are between 1mm and 2mm for 662keV, between 1.5mm and 3mm for 511keV and between 2.5mm and 7mm for 364keV; however, for 140keV the spatial resolution is between 10mm and 14mm.

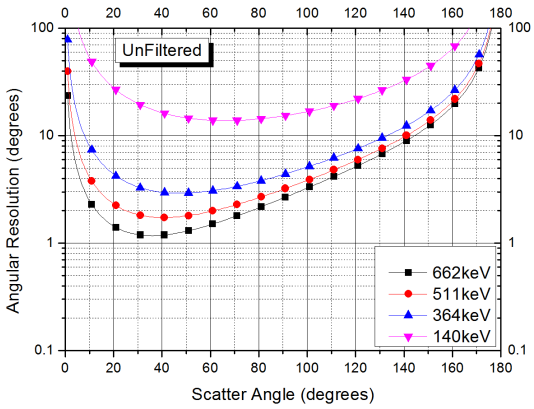

(a) Eg effects on angular resolution for UnFiltered

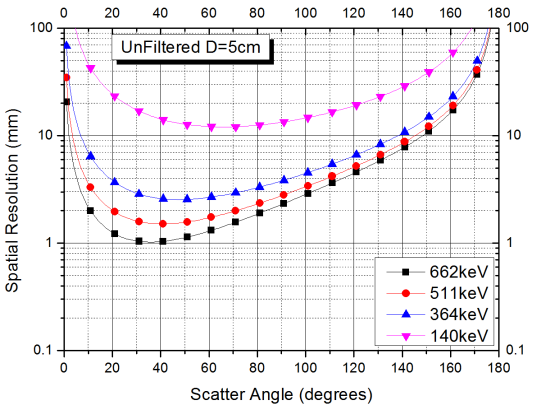

(b) Eg effects on spatial resolution for UnFiltered

Figure 4.20: Effects of Incident Energy on angular and spatial resolution for Unfiltered and D=5cm

It is clear from the graphs that the angular and spatial resolutions are directly proportional to the energy resolution and the gamma ray incident energy which means that the better the energy resolution of the camera the better its angular and spatial resolutions, and also the higher the incident energy the better is the angular and the spatial resolutions. Also, an important characteristic of the effects of the energy on angular and spatial resolutions is that for the same values of resolutions, the scattering angles ranges changes; it shrinks as the energy resolution get worse and the incident gamma ray energy gets smaller.

4.3.3 Source Distance Contribution

The effects of source distance from the Compton camera on the spatial resolution due to the energy uncertainty are presented on the graphs 4.21, 4.22 and 4.23. Source

distances chosen to study this effect are 2.5cm, 5cm, 10cm, 20cm and 40cm.

Figure 4.21 highlights the effects of source distance from the camera on spatial resolution for energy resolutions of MWD and incident gamma ray of 662keV. The minimum spatial resolution given by the graphs for the different source distances from the camera vary between 0.15mm for 2.5cm, 0.2mm for 5cm, 0.6mm for 10cm, 1.2mm for 20cm and 2.3mm for 40cm.

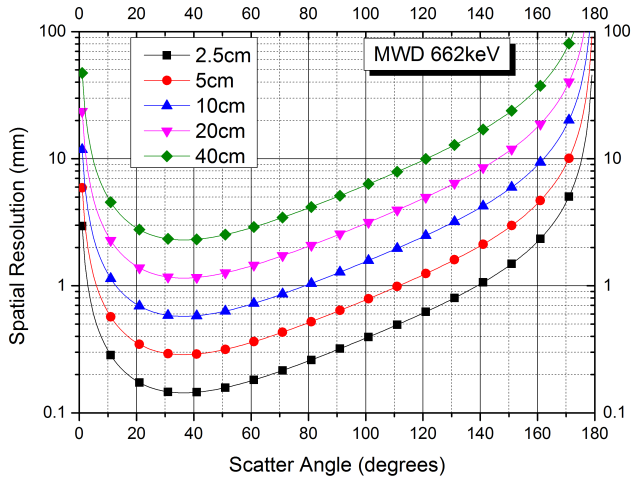

Figure 4.21: Effects of source distance on the spatial resolution due to energy uncertainty for MWD

Figure 4.22 highlights the effects of source distance from the camera on spatial resolution for energy resolutions of the Filtered algorithm and incident gamma ray of 662keV. The minimum spatial resolution given by the graphs for the different source distances from the camera vary between 0.27mm for 2.5cm, 0.5mm for 5cm, 1.1mm for 10cm, 2.1mm for 20cm and 4.1mm for 40cm.

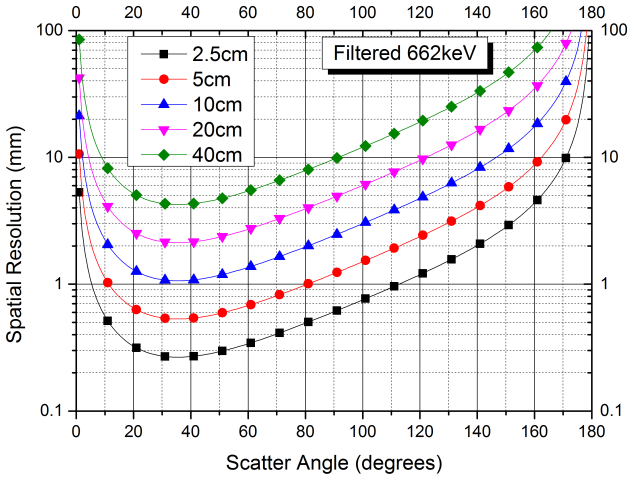

Figure 4.22: Effects of source distance on the spatial resolution due to energy uncertainty for Filtered

Figure 4.23 highlights the effects of source distance from the camera on spatial resolution for energy resolutions of the UnFiltered algorithm and incident gamma ray of 662keV. The minimum spatial resolution given by the graphs for the different source distances from the camera vary between 0.5mm for 2.5cm, 1mm for 5cm, 2mm for 10cm, 4mm for 20cm and 8mm for 40cm.

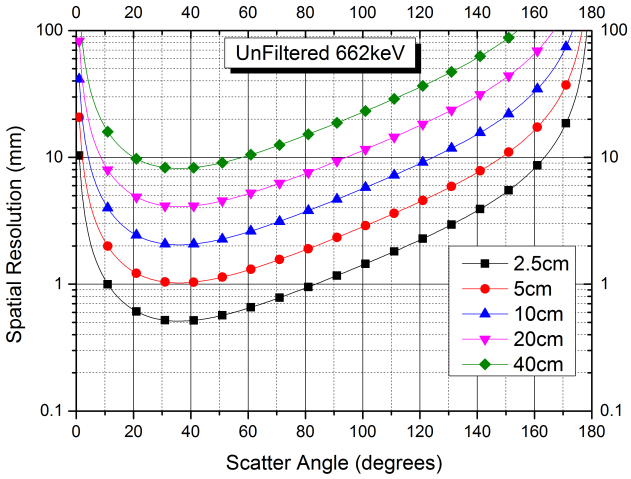

Figure 4.23: Effects of source distance on the spatial resolution due to energy uncertainty for UnFiltered

4.4 Doppler Broadening Contribution to Angular and Spatial Resolution

4.4.1 Compton Profiles

Values of $J_n(p_z)$ (see chapter 2) as a function of p_z have been tabulated for all the elements on a subshell-by-subshell basis [Biggs *et al.*, 1975] using calculations of the electrons' quantum mechanical wave functions. These tabulations, however, neglect the additional momentum states that can arise due to atomic binding effects within a crystalline lattice which were measured by [Reed & Eisenberger, 1972] for Ge, Si and diamond. For comparisons reasons the study of Doppler broadening conducted

on this thesis uses both but eventually because of the small differences for the UCL Compton camera uses [Biggs *et al.*, 1975]. The Figures below shows the $J_n(p_z)$ as a function of p_z.

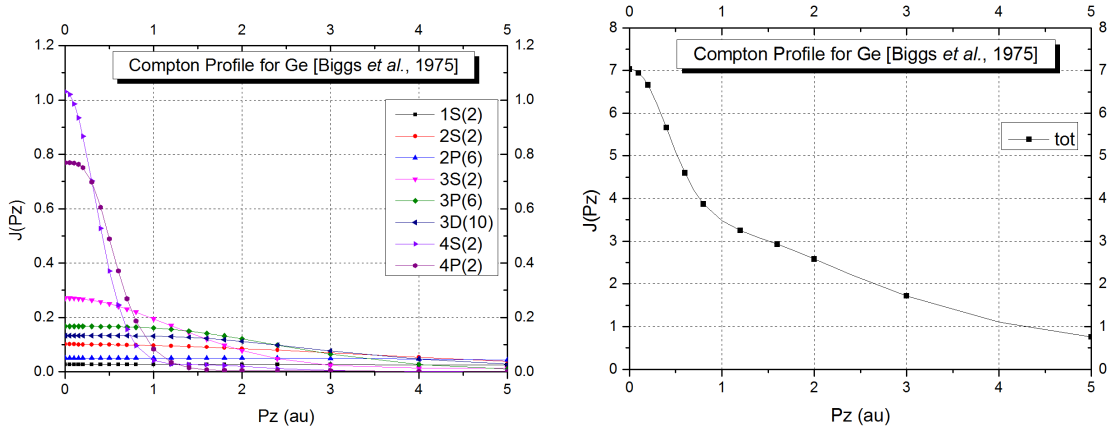

(a) Sub Shell Compton profiles for Ge

(b) Total Compton profile for Ge

Figure 4.24: Compton profile for Ge [Biggs *et al.*, 1975]

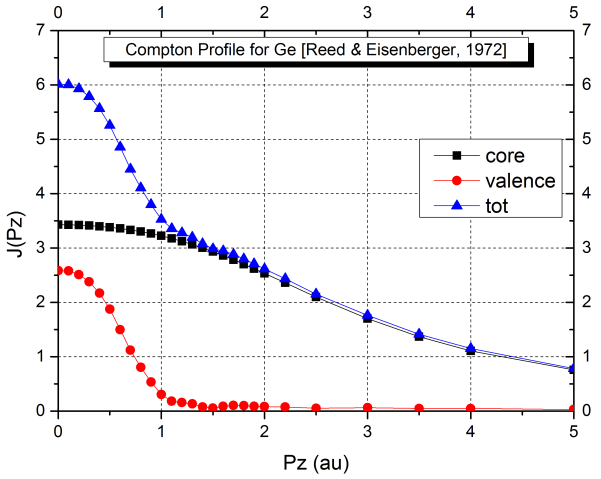

Figure 4.25: Compton profile for Ge [Reed & Eisenberger, 1972]

Figures 4.26 and 4.27 show the effects of Doppler broadening on angular and

spatial resolution using Biggs and Reeds Compton profiles, the difference between the two is not big. The spatial resolution for scattering angles of 0 to 90 is below 3mm.

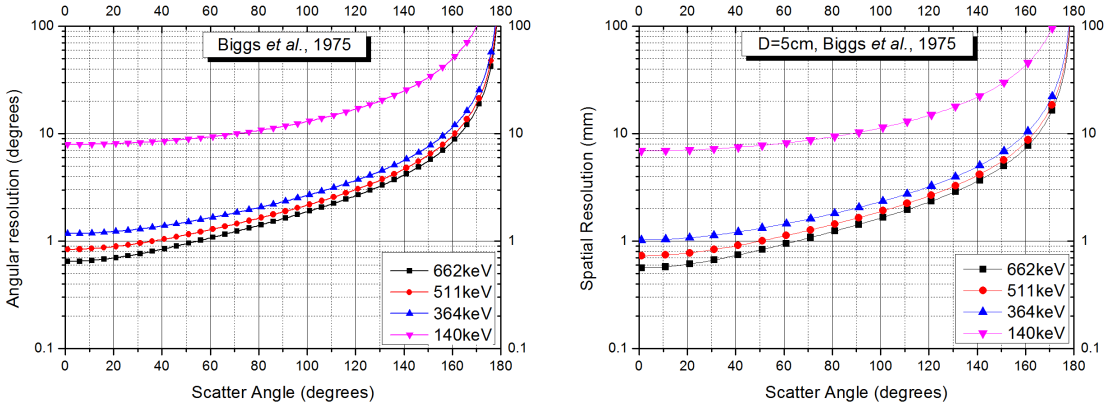

(a) Angular Resolution Effects (b) Spatial Resolution Effects

Figure 4.26: Doppler Broadening Effects on Angular and Spatial Resolution for Germanium. $\sigma_{p_z} = 2au$ [Biggs *et al.*, 1975]

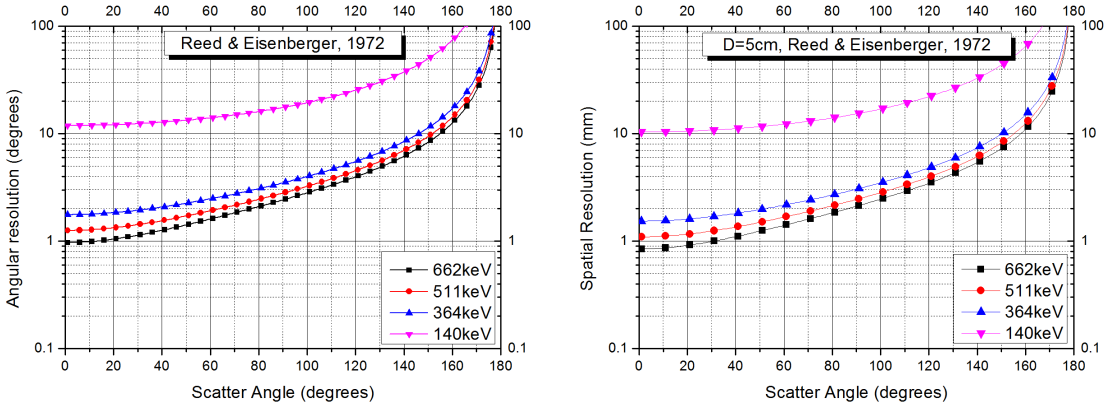

(a) Angular Resolution Effects (b) Spatial Resolution Effects

Figure 4.27: Doppler Broadening Effects on Angular and Spatial Resolution for Germanium. $\sigma_{p_z} = 3au$ [Reed & Eisenberger, 1972]

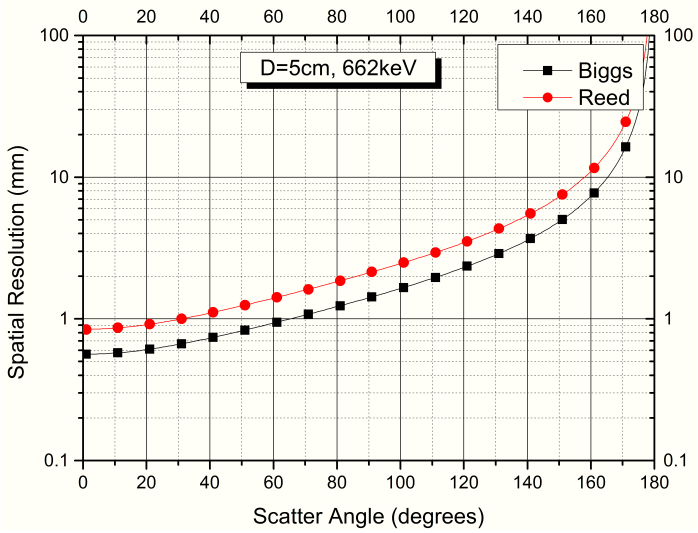

Figure 4.28: Doppler Broadening Effects on Spatial Resolution for Germanium given for Biggs' and Reed's Compton profiles at 662keV and source distance of D=5cm.

Chapter 5

Position Sensitivity Optimization

The position sensitivity enhancements in the X, Y and Z axis are implemented using the knowledge of the physics of charge creation in a pixellated detector. To improve the x-y position sensitivity, the induced charges in neighboring pixels to the pixel where the interaction happened are used; to improve the depth (Z), the polarity of the induced charges are used.

5.1 X-Y Position Sensitivity Optimization

The polarity of the induced charge in the central pixel depends on the location of the interaction. It is bigger on the surrounding pixels that are close to the interaction and gets smaller in the pixels further away; the closest the neighbouring pixel to the interaction the biggest the induced charges. Therefore, an algorithm that determines

where these induced charges are induced and simply compares their amplitudes to determine the pixel that has the biggest induced charges, will improve the position sensitivity in the x/y axis by a factor of two. The pixel size is 4 by 4mm and the gap between the adjacent pixels is 1mm, so without considering the induced charges, the intrinsic position sensitivity of the camera is 2.5mm in the x-y axis; considering the induced charges, however, improves the position sensitivity to 1.25mm.

Figure 5.1 shows traces from the 16 CR pixels and the 4 back detector pixels (the last column the lower 4 traces). This event shows coincident photons in red and a negative induced charge in green in the front detector. Whereas the event on figure 5.2 shows a positive induced charge in the front detector.

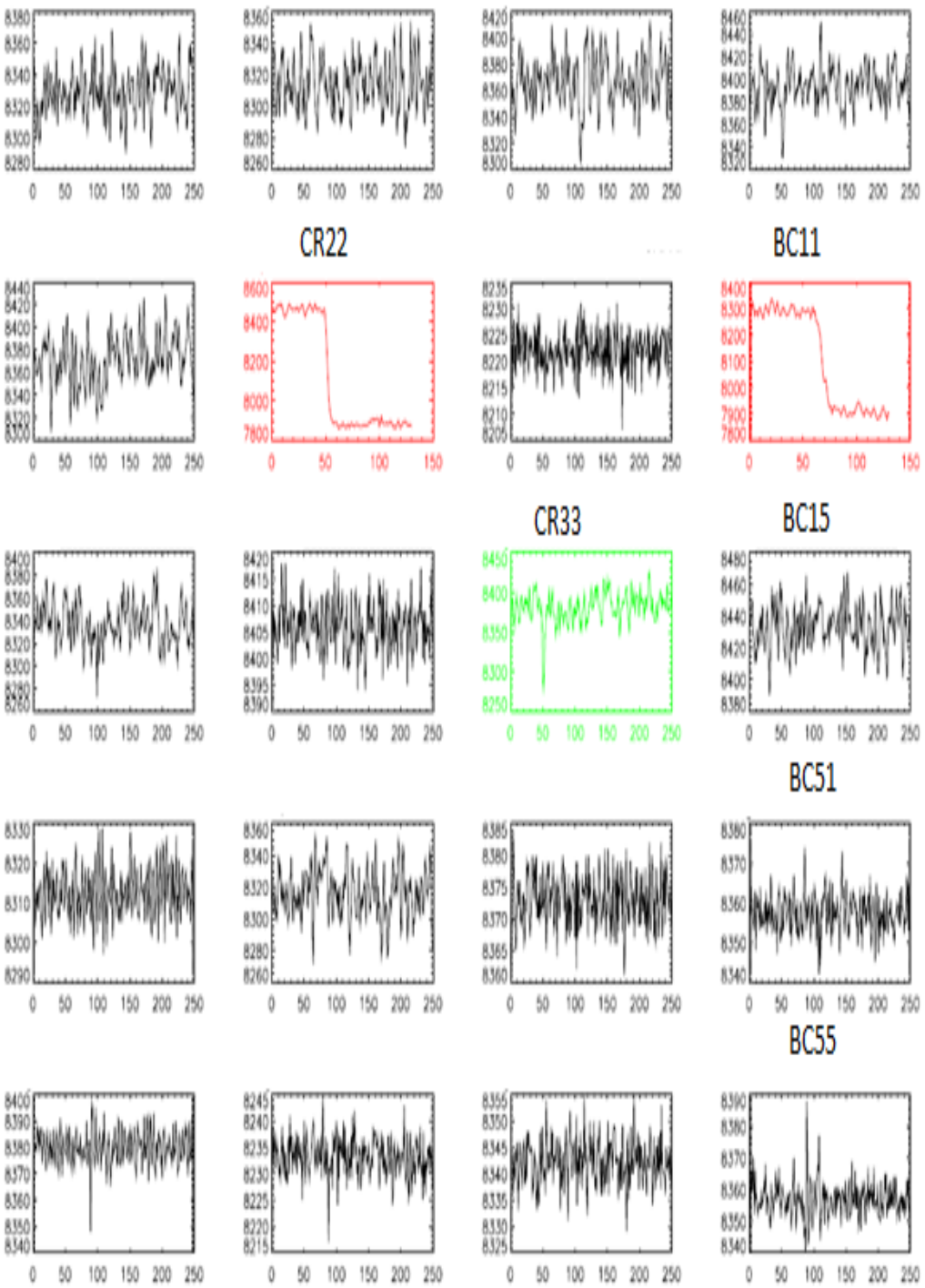

Figure 5.1: An event showing a negative induced charge in green and the coincident photons in red

From this event, the algorithm defines the interaction position in the front detector in pixel CR22 but halfway between CR22 and pixel CR33.

The above event also defines the interaction to happen in the CR33 but halfway between CR33 and CR22. The implementation of this algorithm to improve the x-y position sensitivity is the one which was used to study the effects of x-y position sensitivity on images for this thesis, and it is presented in the following chapter.

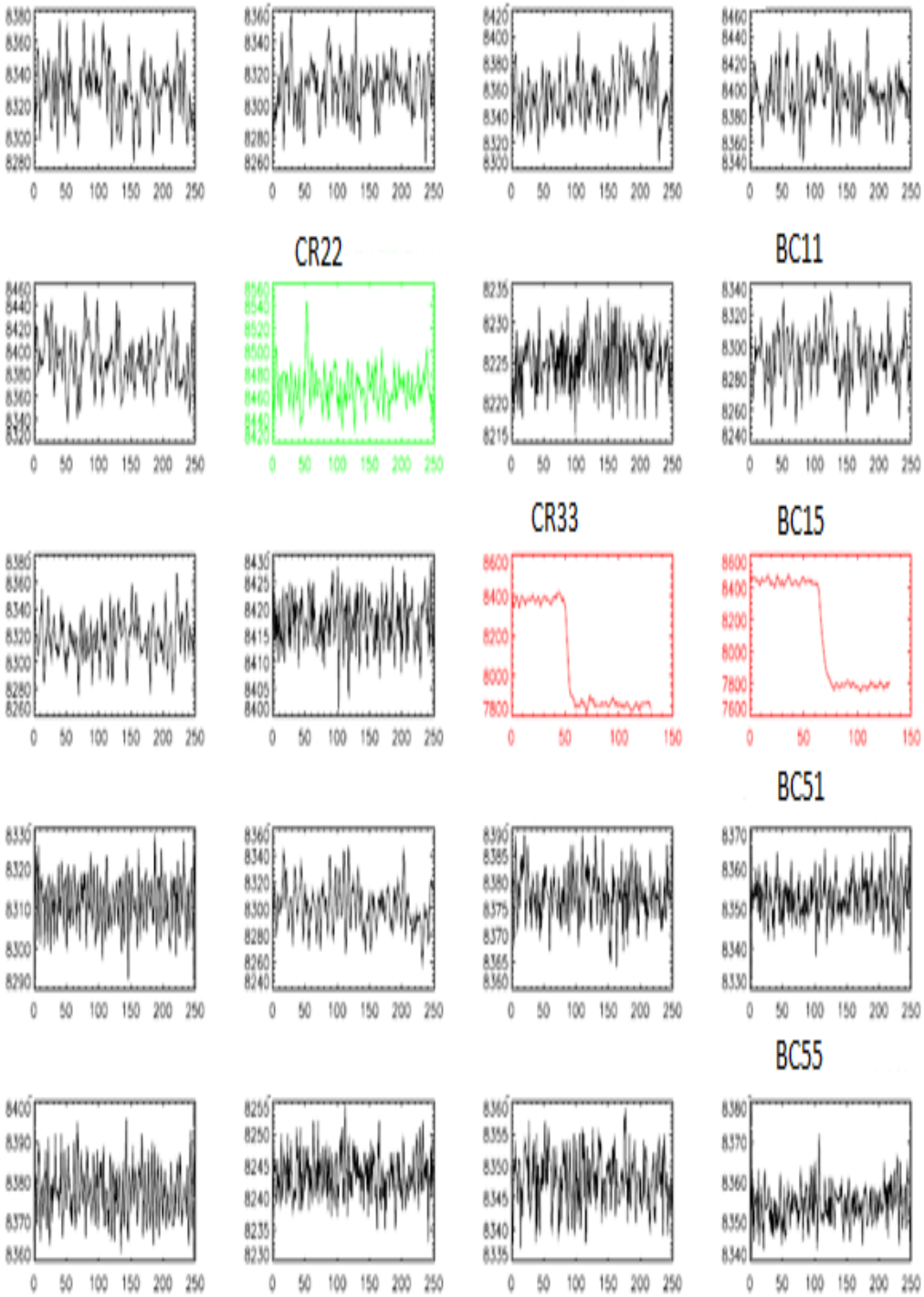

Figure 5.2: An event showing a negative induced charge in green and the coincident photons in red

5.2 Further Improving the X-Y Position Sensitivity

An experiment was conducted to study the possibility of improving the x-y position sensitivity beyond the 1.25mm.

5.3 Experimental set up

In order to test the X-Y position sensitivity, an experimental set up (figure 5.3) has been used. A collimated source of Am-241 and Cs-137 of diameter 2mm on the surface of the pixel plane was used to locate and scan pixels. The Am-241 source was used to locate the edges of the pixels and the Cs-137 source was used to scan the pixel from side to side. The source was moved across the pixel in the x-y directions in steps of 0.5mm. The time required to collect enough events is 24 hours (150 thousands events) of which 40% are accepted by the algorithm. The data is stored in a PC; each position of the source in a separate file, approximately 1.5GB in size. An offline algorithm written in IDL language then processed the data and produced a histogram of position versus number of events for each position. The position sensitivity was quantified by measuring the FHWM of the histograms.

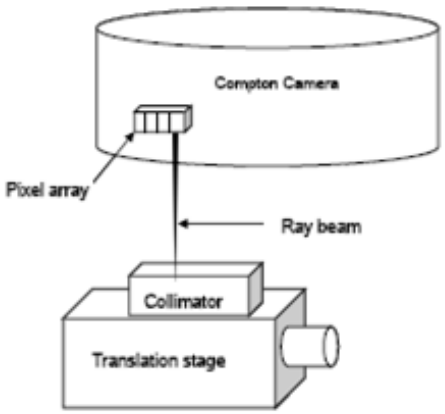

Figure 5.3: experimental setup for studying further improvements in the x-y position sensitivity

5.4 Collimator Characteristics

To find the edges of a pixel, a collimated radiation source of Am-241 of activity 7.4GBq was used. In order to test and enhance the position sensitivity a collimated Cs-137 source was used. The gamma ray energy emitted by the Cs137 source is 662keV. The collimator diameters are highlighted in the figure below. The distance between the collimator and the front pixel surface is 14.5mm and that between the collimator and the surface at the end of the pixel is 20mm.

The collimator acceptance distance at the pixel surface is 0.25mm and is 0.5mm at the surface at the back of the pixel.

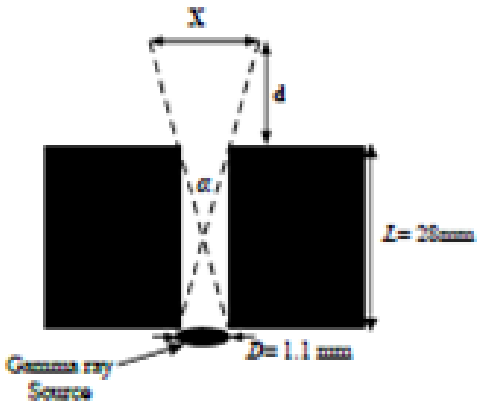

Figure 5.4: collimator characteristics used to improve the x-y position sensitivity

5.5 Pixel edge determination

Although, the camera has a map attached underneath it that shows the location of the pixels, It is important before running experiments on the position sensitivity to double check the accuracy of the map. An experiment was run to find the edges of the pixels using the collimator mentioned above with the Am-241 source was set up. Figure 5.5 plots a measured sensitivity profile across three adjacent pixels obtained by scanning a collimated source. The diagram below shows how the edges are defined. The information obtained from this experiment was used to define the variation of sensitivity across the pixels in order to calibrate the camera. Also, it was used to measure the true sensitive size of the pixels as well as the separation between the pixels.

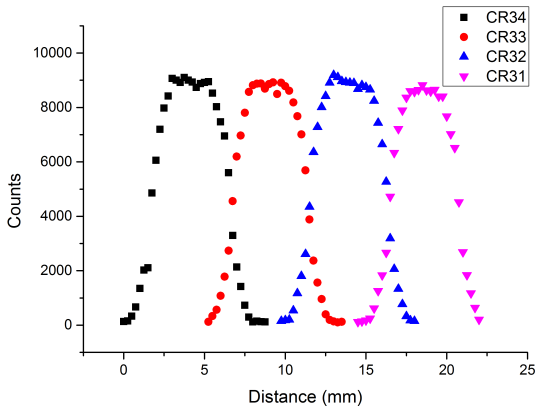

Figure 5.5: Scan of 4 adjacent pixels

5.6 Explanation

In order to test the position sensitivity in the X-Y axis, a pixel was irradiated at calibrated locations with a collimated Cs137 source. The collimated source irradiated a 2.7 mm diameter region of the pixel. The source was scanned in 1 mm steps across the pixel surface and 15104 interactions were recorded at each step.

A simple equation was implemented to weight the relative amplitude of these pulses in order to determine an interaction position. For an interaction in the central pixel, the interaction position is given by:

$$X = \frac{Q_r - Q_l}{Q_r + Q_l} \tag{5.1}$$

$$Y = \frac{Q_t - Q_b}{Q_t + Q_b} \tag{5.2}$$

Where Q_r, Q_l, Q_t and Q_b represent the charges created in the surrounding pixels.

5.7 Position Sensitivity Optimization Results

Figure 5.6 shows X position sensitivity spectra for two source position, one at the right hand side of the pixel and the other at the left hand side.

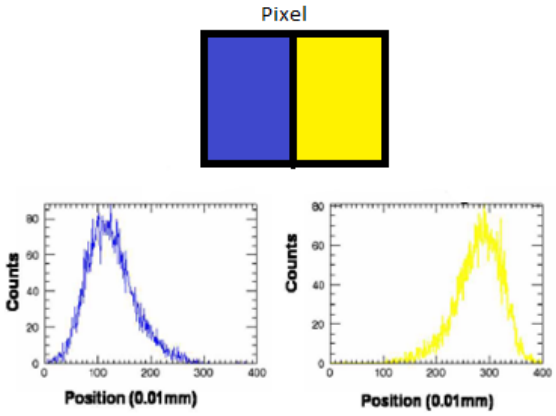

Figure 5.6: x-y position sensitivity results

5.8 Geometry Contribution to Angular and Spatial Resolution

5.8.1 Position Sensitivity Contribution

The following is a set of graphs depicting the predicted geometry contribution for the UCL Compton camera. It studies the effects of enhancing the position sensitivity of the camera beyond its intrinsic position sensitivity which is dictated by the pixels size. On the following graphs and the rest of the thesis, the positions sensitivity is referred to as *PS*, the front detector is referred to as the *front* or abrieviated as *F*, the back detector is referred to as *Back* or simply *B*, The letter *Z* means the position sensitivity are done only in the Z axis, and the same applies for the letters X and Y. Although, the graphs shows the angular and the spatial resolutions effects, the explanation is focused, most of the time on the spatial resolution.

The intrinsic and the front position sensitivity (in the Z, X-Y and X-Y-Z directions) effects on angular and spatial resolution is shown in figure 5.7. The intrinsic spatial resolution is 5.75mm at 0° and goes down as the scattering angles increase to reach 3.25mm at 180°. For scattering angles up to 90°, the effects of enhancing the front's detector position sensitivity on the spatial resolution is more significant in the Z axis and less significant in the X-Y direction. The intrinsic spatial resolution improves by 0.5mm from 5.75mm to 5.25mm in the X-Y direction, but the improvement is

1.25mm when the depth (Z) position sensitivity is implemented. When the position sensitivity enhanced in the three axis, X-Y-Z, the spatial resolution goes down to 4mm. As the scattering angles increases beyond the 90°, the spatial resolution for intrinsic and the front detectors PS enhancements converges to virtually be the same at larger scattering angles.

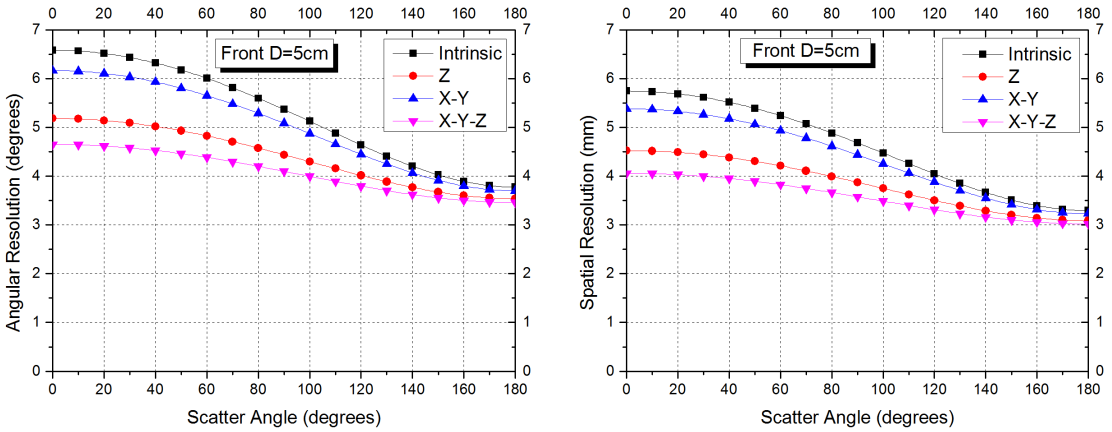

(a) Effects on Angular Resolution (b) Effects on Spatial Resolution

Figure 5.7: Effects of position sensitivity enhancements on angular and spatial resolutions of the front detector compared with the intrinsic detector position sensitivity. Source 5cm from the camera

The intrinsic and the back position sensitivity (in the Z, X-Y and X-Y-Z directions) effects on angular and spatial resolution is shown in figure 5.8. There is no effects of enhancing the back's detector position sensitivity on the spatial resolution in the X-Y axis and the effects are small in the Z direction, but relatively significant compared with the PS effects on the X-Y directions. The intrinsic spatial resolution improves by 0.5mm from 5.75mm to 5.25mm in the Z direction. As opposed to the improvements to the front's detector position sensitivity, the spatial resolution is small for small

scattering angles and slightly larger for bigger scattering angles. For example, for a scattering angles of 20° and scattering angles 140°, the difference between the intrinsic and the back detector's PS enhancement is 0.5mm and about 1mm respectively.

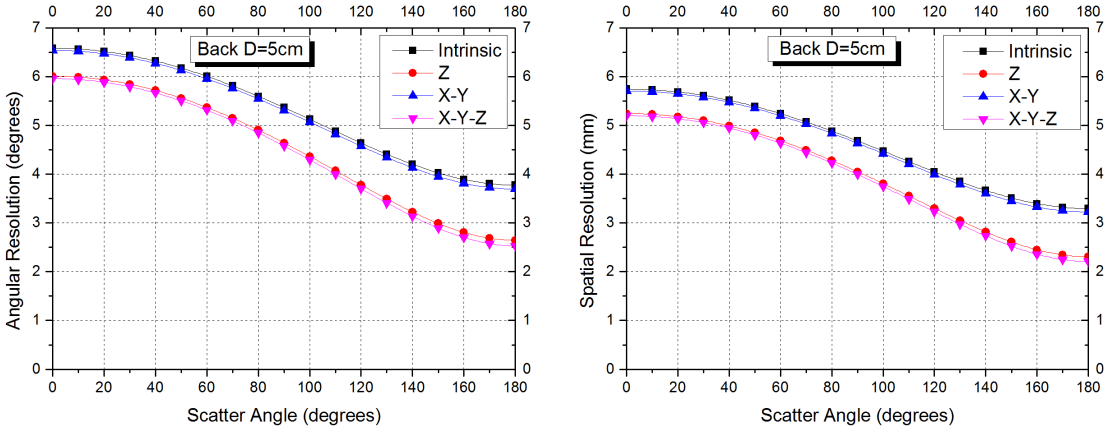

(a) Effects on Angular Resolution

(b) Effects on Spatial Resolution

Figure 5.8: Effects of position sensitivity enhancements on angular and spatial resolutions of the back detector compared with the intrinsic detector position sensitivity. Source 5cm from the camera

The intrinsic, and the front's and back's position sensitivity (in the Z, X-Y and X-Y-Z directions) effects on angular and spatial resolution is shown in figure 5.9. The effects of enhancing the front's and the back's detectors position sensitivity on the spatial resolution in the X-Y axis are small, and the effects are larger in the Z direction. The intrinsic spatial resolution improves by 0.5mm from 5.75mm to 5.25 in the Z direction for small scattering angles and from 3.25mm to 2.25mm for bigger scattering angles. The intrinsic spatial resolution improves by 2mm from 5.75mm to 3.75mm in the X-Y direction, and the improvement is 2.5mm when the depth (Z) position sensitivity is included.

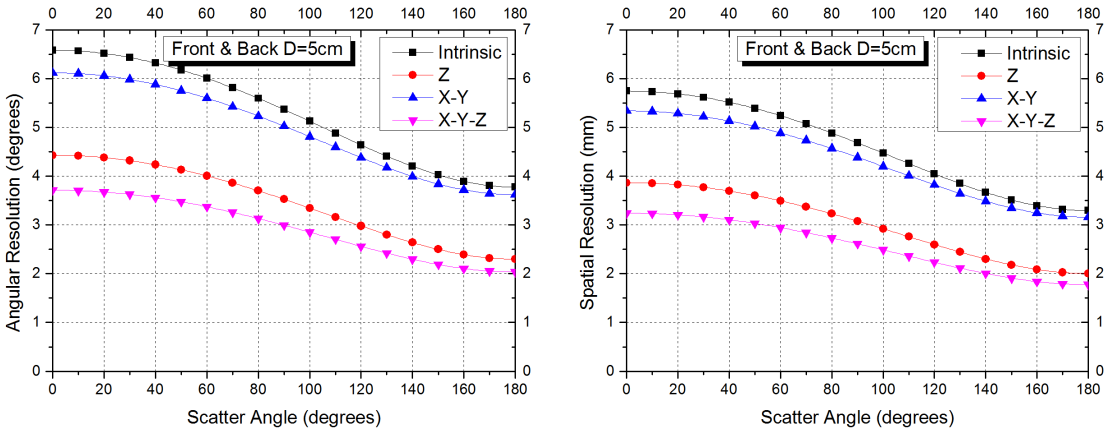

(a) Effects on Angular Resolution

(b) Effects on Spatial Resolution

Figure 5.9: Effects of position sensitivity enhancements on angular and spatial resolutions of the front and back detectors compared with the intrinsic detector position sensitivity. Source 5cm from the camera

From the explanation of the graphs above, it is concluded that the effects of improving the depth are more significant that those of improving the position sensitivity in the X-Y directions, and the effects of improving the front's detectors position sensitivity are significant to those of the back detector, in fact the back detector's position sensitivity effects are negligible in the X-Y axis but small in the Z axis. Therefore, to optimize the spatial resolution of the UCL Compton camera, the work should focus on mainly improving the depth position sensitivity, and to a less importance to improving the X-Y position sensitivity of the front detector and should ignore the back detectors X-Y position sensitivity.

5.8.2 Source Position Contribution

The effects of source distance for the Compton camera on the spatial resolution due to the position sensitivity enhancements are presented on the graphs 5.10, 5.11, 5.12 and 5.13. Source distances chosen to study this effect are 2.5cm, 5cm, 10cm, 20cm and 40cm.

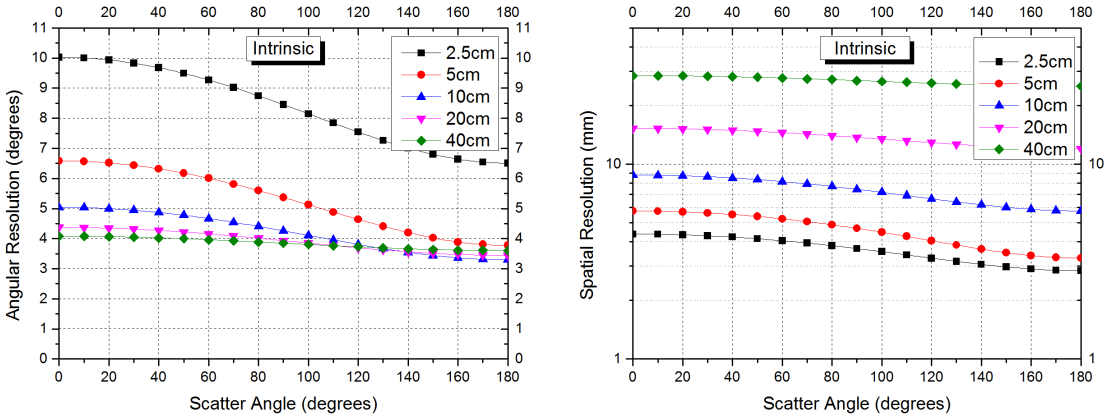

(a) Effects on Angular Resolution (b) Effects on Spatial Resolution

Figure 5.10: Effects of source position on angular and spatial resolution for the intrinsic geometry (no PS enhancements)

Figures 5.10 shows the effects of source position distances from the camera on the UCL Compton camera with no PS optimization. For a scattering angle of 80°, the spatial resolution of the UCL Compton camera vary between 3.5mm for 2.5cm source distance, 5mm for 5cm, 7.5mm for 10cm, 10.5mm for 20cm and 12mm for 40cm distances.

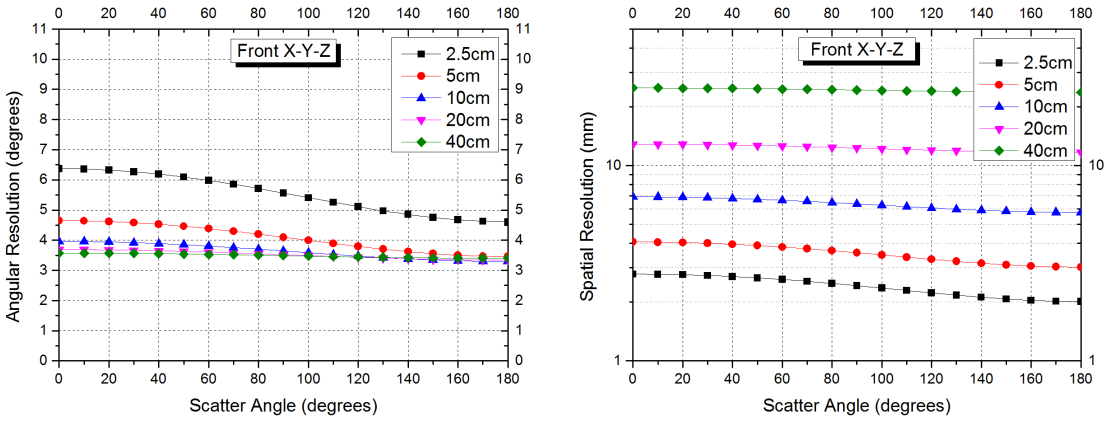

(a) Effects on Angular Resolution (b) Effects on Spatial Resolution

Figure 5.11: Effects of source position on angular and spatial resolution for X-Y-Z PS enhancements on the front detector

Figures 5.11 shows the effects of source position distances from the camera on the UCL Compton camera with the front's detector optimization in the X-Y-Z directions. For a scattering angle of 80°, the spatial resolution of the UCL Compton camera vary between 2.5mm for 2.5cm source distance, 3.8mm for 5cm, 6.5mm for 10cm, 10.3mm for 20cm and 11.5mm for 40cm distances.

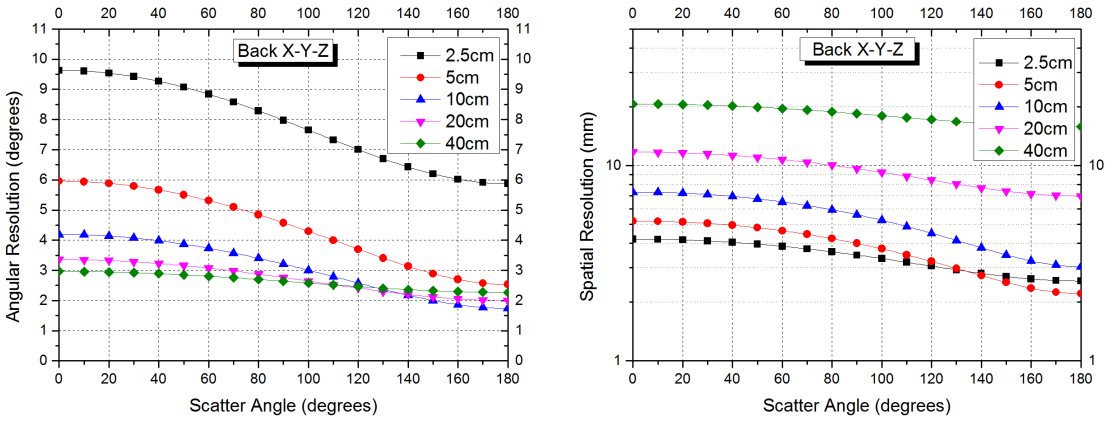

(a) Effects on Angular Resolution (b) Effects on Spatial Resolution

Figure 5.12: Effects of source position on angular and spatial resolution for X-Y-Z PS enhancements on the back detector

Figures 5.12 shows the effects of source position distances from the camera on the UCL Compton camera with the back's detector optimization in the X-Y-Z directions. For a scattering angle of 80°, the spatial resolution of the UCL Compton camera vary between 3.8mm for 2.5cm source distance, 4.2mm for 5cm, 5.2mm for 10cm, 9mm for 20cm and 10.8mm for 40cm distances.

Figures 5.12 shows the effects of source position distances from the camera on the UCL Compton camera with the front's and the back's detectors optimization in the X-Y-Z directions. For a scattering angle of 80°, the spatial resolution of the UCL Compton camera vary between 2.2mm for 2.5cm source distance, 2.5mm for 5cm, 4mm for 10cm, 7.2mm for 20cm and 10.5mm for 40cm distances.

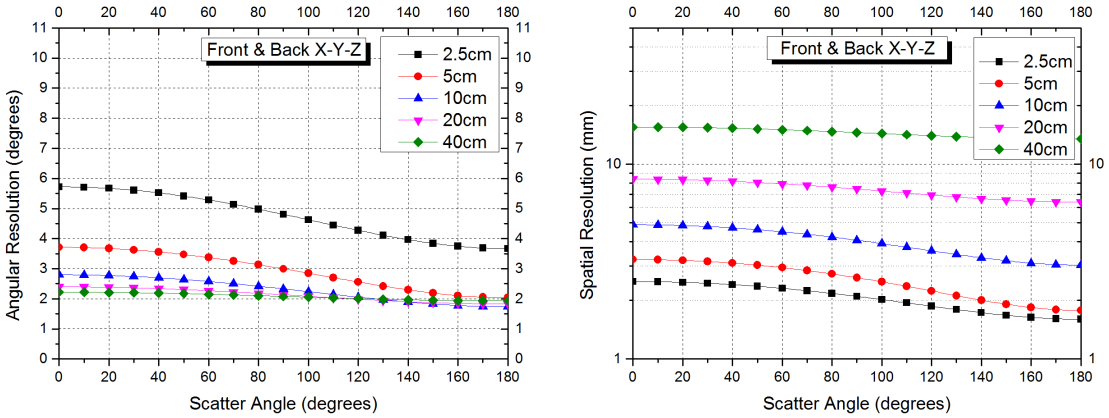

(a) Effects on Angular Resolution (b) Effects on Spatial Resolution

Figure 5.13: Effects of source position on angular and spatial resolution for X-Y-Z PS enhancements on the front and back detectors

Chapter 6

Efficiency and Spatial Resolution

This chapter presents the theoretical and the measured efficiency and why the theoretical is significantly higher than the measured. The chapter presents the predicted and the measured spatial resolution of point sources.

6.1 Efficiency of Individual Pixels

Efficiency for individual pixels of the UCL Compton camera were measured using a Cs137 gamma source of activity 3.7MBq. An analog NIM pulse shape amplifier and a multi channel analyzer (MCA) interfaced to a PC running ORTECs MAESTRO software were used to acquire energy spectra for each pixel. The number of recoded photons is then read out of the energy spectra. The gamma ray source was placed 1.35cm from the front detector and 11.5cm from the back detector. To correct for the

source decay, equation (6.1) was used.

$$A = A_0 exp - (t/\tau) \tag{6.1}$$

The Cs137 gamma source has a half-life of 30.07 years and the source was calibrated 7.5 years ago; $t = 7.5$years, $\tau = 30.07$years $\times$ 1.4427 which equals to 43.38 years. Therefore, $A/A_0 = exp - (7.5/43.38) = 0.84$ shows that the source lost 16% of its activity and the current activity is 3.108MBq.

The intrinsic efficiency of a detector is defined by:

$$\text{Intrinsic Efficiency} = \frac{\text{number of photons recorded}}{\text{number of incident photons}} \tag{6.2}$$

The number of recorded photons was read out of the energy spectra acquired; to calculate the number of incident photons, the space subtended by a pixel of $l \times l = 4mm \times 4mm$ for a gamma ray source at a distance of R is calculated using equation (6.3):

$$\text{space subtended by a pixel} = (l^2)/(4\pi R^2) \tag{6.3}$$

Where l^2 is the area of the pixels face, and $4\pi R^2$ is the area of the sphere with a radius R equal to the source to detector distance. For the front detector ($R = 1.35cm$), a pixels intercepts 0.70% of all space; for the back detctor ($R = 11.17cm$), a pixel

Table 6.1: CR front detector intrinsic efficiency

Pixels	Count Rate (662keV)	Count Rate (all)	Source Activity (MBq)	Photons Emitted	Efficiency (662keV)	Efficiency (all)
CR11	30	1867	3.108	21713	0.00137	0.086
CR12	40	2195	3.108	21713	0.00185	0.101
CR14	39	2540	3.108	21713	0.00183	0.117
CR21	31	1715	3.108	21713	0.00144	0.079
CR22	37	2068	3.108	21713	0.00173	0.095
CR23	40	2317	3.108	21713	0.00186	0.107
CR24	36	2212	3.108	21713	0.00170	0.102
CR31	30	1768	3.108	21713	0.00140	0.081
CR32	42	2453	3.108	21713	0.00196	0.113
CR33	40	2321	3.108	21713	0.00188	0.107
CR34	40	2444	3.108	21713	0.00186	0.113
CR41	29	2480	3.108	21713	0.00133	0.114
CR42	35	1906	3.108	21713	0.00163	0.088
CR43	36	2087	3.108	21713	0.00167	0.096
CR44	34	2073	3.108	21713	0.00159	0.096

intercepts only 0.01% of all space.

This means that the number of incident photons for the front detector is equal to $3.108 \times 10^6 \times 0.70/100$ and for the back detector is $3.108 \times 10^6 \times 0.01/100$; that is 21713 photons/second and 317 photons/second for the front and the back detectors respectively.

The intrinsic efficiency measured for each pixel are presented in table (6.1) for CR front detector pixels, table (6.2) for the LC front detector pixels and table (6.3) for the BC back detector pixels.

Table 6.2: LC front detector intrinsic efficiency

Pixels	Count Rate (662keV)	Count Rate (all)	Source Activity (MBq)	Photons Emitted	Efficiency (662keV)	Efficiency (all)
LC11	27	1641	3.108	21713	0.0013	0.076
LC12	34	2039	3.108	21713	0.0016	0.094
LC13	37	1842	3.108	21713	0.0017	0.085
LC14	32	1773	3.108	21713	0.0015	0.082
LC21	31	1723	3.108	21713	0.0014	0.079
LC22	39	2071	3.108	21713	0.0018	0.095
LC23	41	2127	3.108	21713	0.0019	0.098
LC24	41	2140	3.108	21713	0.0019	0.099
LC31	32	1904	3.108	21713	0.0015	0.088
LC32	44	2253	3.108	21713	0.002	0.104
LC33	39	2776	3.108	21713	0.0018	0.128

Table 6.3: BC Back detector intrinsic efficiency

Pixels	Count Rate (662keV)	Count Rate (all)	Source Activity (MBq)	Photons Emitted	Efficiency (662keV)	Efficiency (all)
BC11	3.4	223	3.108	317.16	0.01073	0.706
BC12	3.4	201	3.108	317.16	0.01083	0.636
BC13	3.4	200	3.108	317.16	0.01072	0.632
BC14	3.2	217	3.108	317.16	0.01037	0.687
BC15	3.4	244	3.108	317.16	0.01083	0.769
BC21	3.4	224	3.108	317.16	0.01082	0.708
BC22	3.5	204	3.108	317.16	0.01124	0.645
BC23	3.6	254	3.108	317.16	0.01158	0.803
BC25	3.2	251	3.108	317.16	0.01028	0.793
BC32	3.2	240	3.108	317.16	0.01038	0.759
BC34	3.3	212	3.108	317.16	0.01052	0.671
BC35	3.9	244	3.108	317.16	0.01233	0.772
BC41	3.4	245	3.108	317.16	0.01071	0.774
BC42	3.3	194	3.108	317.16	0.01062	0.613
BC43	3.6	279	3.108	317.16	0.01146	0.880
BC51	3.3	244	3.108	317.16	0.01056	0.772
BC52	3.3	217	3.108	317.16	0.0106	0.687
BC53	3.2	190	3.108	317.16	0.01009	0.602
BC54	3.3	206	3.108	317.16	0.01055	0.652
BC55	3.5	192	3.108	317.16	0.01109	0.607

6.2 UCL Compton Camera Efficiency

The intrinsic efficiency ε_{icc} for a Compton camera is defined as the fraction of photons entering the first detector that undergo only one Compton scattering in the first detector and then undergo photoelectric absorption [1] in the second detector for a point source can be expressed as in equation (6.4):

$$\varepsilon_{icc} = \frac{1}{\Omega_1} \int_{det1} \mathrm{d}V_1 \int_{det2} \mathrm{d}V_2 \Delta\Omega_1 \mu_c(E_0) \mathrm{e}^{(-\mu_t(E_0)L_1)} \times \frac{\mathrm{d}\sigma}{\mathrm{d}\Omega}(\theta_{12}) \Delta\Omega_2 \mathrm{e}^{(-\mu_t(E_1)L_{12})} \mu_p(E_1) \tag{6.4}$$

where Ω_1 is the solid angle subtended by the first detector, $\Delta\Omega_1$ is the solid angle for a differential volume element $\mathrm{d}V_1$ in the first detector, L_1 is the attenuation length in the first detector between the source and $\mathrm{d}V_1$, μ_t , μ_c , and μ_p are the total, Compton scatter, and photoelectric coefficients, respectively, L_{12} is the attenuation length between the two elements $\mathrm{d}V_1$ and $\mathrm{d}V_2$.

6.2.1 Simulated Efficiency

The intrinsic efficiency of the UCL Compton camera were calculated for energy gamma sources of 140, 350, 392, 511 and 662keV at a distance of 5cm from the center of the camera using Monte-Carlo simulations 6.4:

[1] As noted in section (2.1), in nuclear medicine applications where the incident energy is known, the scattered photon need not to be absorbed by the back detector.

Table 6.4: UCL Compton camera intrinsic efficiency [Royle *et al.*, 2003]

Source Energy (keV)	Intrinsic Efficiency
140	1.91×10^{-04}
350	3.91×10^{-05}
392	2.70×10^{-05}
511	1.09×10^{-05}
662	6.86×10^{-06}

The intrinsic efficiency values given in table (6.4) are efficiencies of events which originates from photons that add up to 662keV. As mentioned in section (2.1), in nuclear medicine applications the incident gamma ray source energy is known and therefore events that does not add up to 662keV (events that has one Compton interaction in the front detector and one in the back) should be taken into considerations when calculating the efficiency of Compton cameras designed for nuclear medicine.

6.2.2 Measured Efficiency

The intrinsic efficiency of the UCL Compton camera was measured for a Cs137 point source at a distance of 5cm from the center of the camera using the DAQ described in section (3.3). The experiment involved 31 pixels and was run for 15 hours. The number of good events (including all types of events) counted was 15500 (0.287 event/second) and the number of good events that add up to 662keV were 418 (7.74×10^{-3} events/second) events. Therefore, out of the total events acquired during this experiment, this represents 0.11% and 2.99×10^{-3}% for all types of good events and for good events that add up to 662keV respectively.

In order to compare the simulated intrinsic efficiency with the measured, the number of good events expected from when all the 177 pixels of the camera are operational has to be calculated. Assuming a linear relationship between the solid angle and the number of good events, the ratio of the total solid angle subtended by all the camera's pixels over the solid angle subtended by the 31 pixels was calculated which equals to 5.7. Therefore, the number of all good events would be 86800 (1.6074 events/second) and for the events that add up to 662keV would be 2340 events (0.043 events/second) in 15 hours.

The intrinsic efficiency is calculated using equation (6.2), where, for a Compton camera, the number of photons recorded represents the number of good events. The number of incident photons is the number of photons subtended by the first detector every second. For a point source at a distance of 5cm from the camera, the front detector subtends 9.19% of all the space, and the number of incident photon is therefore, equals to 285711. Table (6.5) shows the measured intrinsic efficiency of the UCL Compton camera for 31 pixels and the predicted one for all the 177 pixels of the camera. Therefore, the expected improvements in the UCL Compton camera intrinsic efficiency is a factor of 5 times when the remaining pixels are activated. The difference between the simulated and the measured efficiencies is quiet large for good events that add up to 662keV: the measured efficiency is about 45 times worse than the simulated. However, if all types of good events are considered, the meausred

efficiency is comparabale to the simulated efficiency.

Table 6.5: UCL Compton camera measured intrinsic efficiency

number of pixels	All event's types	Events add up to 662keV
31	1.01×10^{-6}	2.71×10^{-8}
177	5.62×10^{-6}	1.50×10^{-7}

However, in reality no matter how many pixels are activated, the efficiency will not improve; in fact, the more pixels activated, the worse the efficiency it gets. This is due to the way the readout electronics is configured and its data rate limitation of 4MB/s; hence, even the value of 45 times worse than the simulated prediction of the intrinsic efficiency is not possible. The readout electronics is configured to send a trace of length 3.125us and its related headers for each channel (or pixel) used to the PC. The trace of 3.125us represents 250 words of data and each word represents 2 bytes; that is 500 bytes plus about 20 bytes of headers. The number of total events Ne_t every second can be calculated by the equation (6.5), where 4×10^6 is the data rate of the electronics in bytes/second, N_{pixels} is the number of pixels used and 520 is the size of a trace and its headers in bytes.

$$Ne_t = \frac{4 \times 10^6}{N_{pixels} \times 520} \tag{6.5}$$

Therefore, for 31 pixels, one event would generate 248 events every second of which only 0.287 event/s represent all types of good events and 7.74×10^{-3} event/s are good events that add up to 662keV. This represents 0.11% and 2.99×10^{-3}% for all types

of good events and events that add up to 662keV respectively. Assuming that the percentages of good events are linearly related to the number of events collected every second, for 177 pixels, the number of total events (using equation 6.5) is equal to 43 event/s which would generate 4.78×10^{-2}/s for all good events and 1.299×10^{-3}/s for events that add up to 662keV. The intrinsic efficiency results from this is given in table (6.6):

Table 6.6: UCL Compton camera measured intrinsic efficiency taking the readout electronics effect into consideration

number of pixels	All event's types	Events add up to 662keV
31	1.01×10^{-6}	2.71×10^{-8}
177	1.67×10^{-7}	4.54×10^{-9}

The expected intrinsic efficiency when the effects of the readout electronics are taken into consideration is quiet significant: about 1500 times worse than the simulated for good events that add up to 662keV, and if all types of good events are considered, the difference is about 40 times worse.

The important question to answer is: how can the predicted intrinsic efficiency, calculated using simulation, be achieved or even exceeded? There are three possible solutions: leaving the system with the current configuration but with a better data rate, slightly changing the system's configuration and a better data rate, or completely changing the way the readout electronics is operating with better data rate.

If the system is left unchanged with its current configuration, for the intrinsic efficiency of the simulation to be achieved, using equation (6.2), the number of all

good events should be 72 event/s and the number of events that add up to 662keV should be 1.96 event/s. the read out electronics data rate can be calculated using equation (6.5). If the intrinsic efficiency is defined by only considering the good events that add up to 662keV, the readout electronics data rate should be about 6GB/s; and if the intrinsic efficiency is defined by considering all types of good events, the data rate should be about 160MB/s.

If, however, the system changed slightly and is configured to send only 2us of traces (instead of 3.125us), to achieve the simulated intrinsic efficiency, the data rate should be about 4GB/s if the definition of the intrinsic efficiency considers only the good events that add up to 662keV, and if the definition considers all types of good events, the data rate should be about 100MB/s.

Finally, the last option available to improve the intrinsic efficiency of a Compton camera, is to change completely how the read out electronics is operating. Instead of sending the data of all the pixels of the Compton camera to the processing unit (i.e. PC), only the pixels that have interactions are considered together with their corresponding surrounding pixels (to implement position sensitivity enhancements). This would reduce the number of traces should be transfered to the processing unit to only 18 traces. The data rate for traces of 2us would be about 390MB/s when only good events that add up to 662keV are considered and 10MB/s when all types of good of events are considered. This approach has a huge advantage over the current

setup because no matter how large the number of pixels constitutes the Compton camera, the number of traces need to be send and processed by the processing unit is always 18 traces for cameras with position sensitivity capabilities and only 2 pixels for Compton cameras that does not.

6.3 Theoretical Spatial Resolution

The total spatial resolution of the UCL Compton camera is calculated using equations (2.9) and (2.10) (see section 2.7). The total spatial resolution of a Compton camera equals to the quadratic summation of the spatial resolutions due to Doppler broadening, energy resolution and geometry. The graphs in this section represents the total spatial resolutions for different energy resolutions (MWD, Filtered and UnFiltered algorithms), different position sensitivity improvements (Front, Back and Front&Back X-Y-Z detectors PS enhancements by a factor of two), and Doppler effects calculated using Compton profiles from [Reed & Eisenberger, 1972] and [Biggs *et al.*, 1975] (see section 4.4).

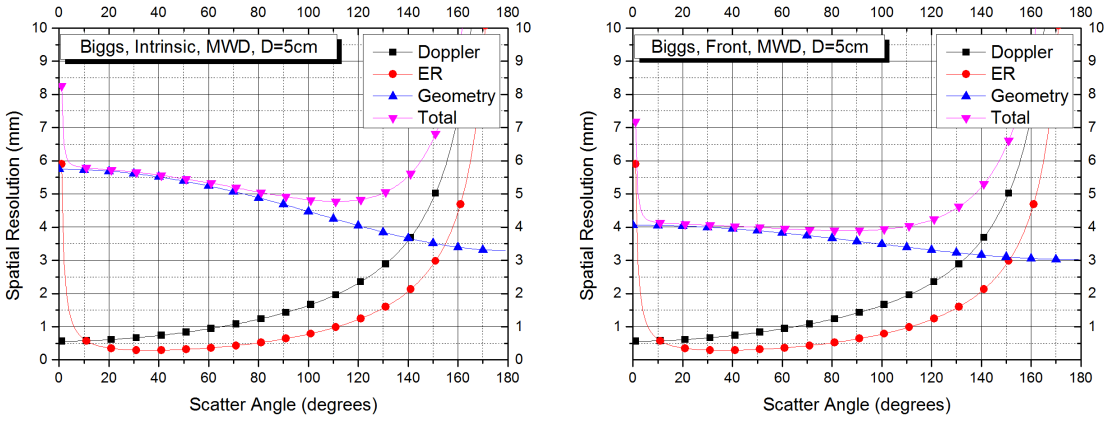

(a) Intrinsic Geometry (b) Front detector PS Enhancement

Figure 6.1: Total spatial resolution with no PS enhancement, and with the front detector PS enhancement. Source is 662keV and 5cm from the camera.

Figures 6.1 and 6.2 represents the total spatial resolution for UCL Compton camera for a source at a distance of 5cm for different position sensitivity: Intrinsic geometry

(no PS enhancements), Front X-Y-Z, Back X-Y-Z, and Front&Back X-Y-Z PS enhancements. The energy resolution was that of the MWD, the Doppler broadening was calculated using Compton profiles from [Biggs *et al.*, 1975]. Figure 6.1a shows the total spatial resolution when no position sensitivity are considered (intrinsic geometry), figure 6.1b is for the front detector X-Y-Z PS enhancements, figure 6.2a is for the back detector X-Y-Z PS enhancements and figure 6.2b is when both detectors (back and front) position sensitivities are improved in the X-Y-Z (the PS enhancements is by a factor of two).

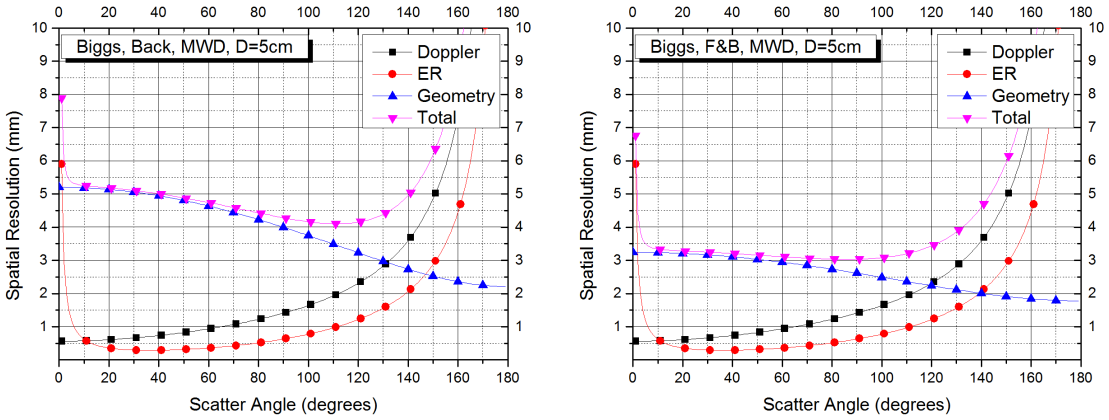

(a) Back detector PS Enhancement (b) Front and Back detectors PS Enhancement

Figure 6.2: Total spatial resolution with the back detector PS enhancement, and with the front and the back detectors PS enhancement. Source is 662keV and 5cm from the camera.

The total spatial resolutions for intrinsic geometry (6.1a) is between 5mm and 6mm for scattering angles 5° and 145°; for the front detector PS enhancements (figure 6.1b) is 4mm for scattering angles between 10° and 120°; for the back detector PS enhancements (6.2a) is between 4mm and 5mm for scattering angles between 10° and

140°; for the PS enhancements of both detectors (6.2b) is 3mm for scattering angles between 10° and 100°.

A very important conclusion from the graphs of figures (6.1a), (6.1b), (6.2a) and (6.2b) is that the total spatial resolution of the UCL Compton camera is dictated by the geometry of the camera for scattering angles between 10° and 100°. For scattering angles above 100° the total spatial resolution starts slowly diverge from the geometry spatial resolution and converge to the spatial resolution of the Doppler broadening at angles above 150°. The spatial resolution due to the energy resolution for the Compton camera has no effect on the total spatial resolution.

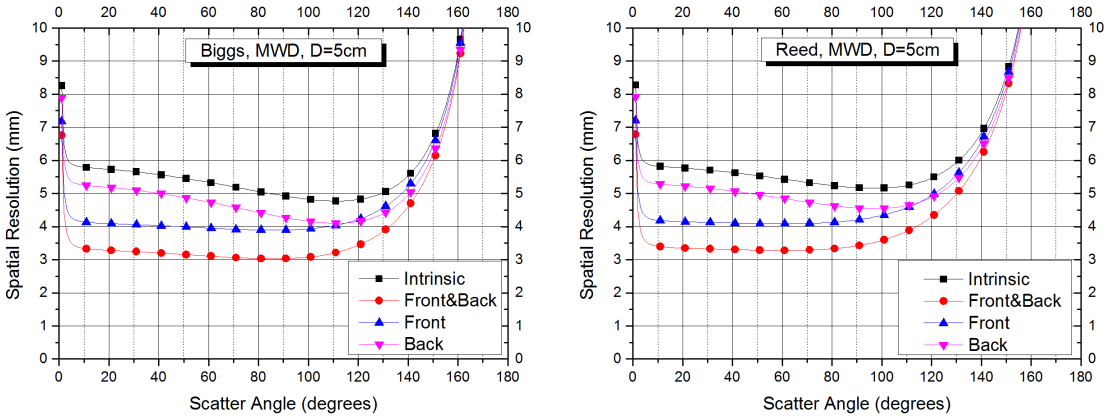

(a) Total spatial resolution using Biggs' (b) Total spatial resolution using Reed's

Figure 6.3: Total spatial resolution comparison between Reed's and Biggs Compton profiles for MWD ER given for intrinsic, front, back, and front and back x-y-z position sensitivity enhancements. Source is 662keV and 5cm from the camera.

Figure (6.3) compares the total spatial resolutions predicted when the spatial resolution due to Doppler broadening use Compton profiles taken from [Biggs *et al.*, 1975] (figure 6.3a) and [Reed & Eisenberger, 1972] (figure 6.3b). The source is at a

distance of 5cm from the camera, the energy resolution used is obtained by the MWD and camera geometry with and without PS enhancements. The graphs show that there is no difference between the two for scattering angles up to 100° and above that there are small differences.

From figures (6.3) and (6.4), the difference between the total spatial resolutions for the different energy resolutions are negligible for scattering angles from 10° and 100°; above 100° the differences for MWD and Filtered energy resolutions are small, but for energy resolutions of the UnFilterd are larger.

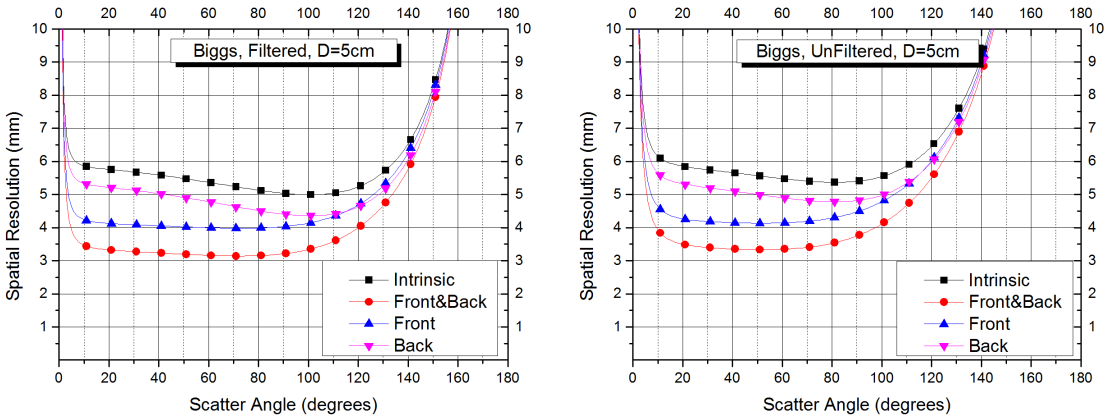

(a) Total spatial resolution with Filtered ER (b) Total spatial resolution with UnFiltered ER

Figure 6.4: Total spatial resolution for a source 5cm from the camera, Filtered and UnFiltered ER given for intrinsic, front, back, and front and back x-y-z position enhancements. Source is 662keV and 5cm from the camera.

For the UCL Compton camera (figure 6.5), the dictating factor to angular and spatial resolutions is the position sensitivity. For the UCL Compton camera the energy resolution no matter how good it is, it has no effect on improving the angular and the spatial resolution. The same applies for Doppler broadening. The position

sensitivity improvements on the X-Y for the back detector has a negligible effect, and the X-Y of the front has a small effect on the total spatial resolution. However, the improvements in the depth (Z) position sensitivity is significant on the front detector, and small for the back.

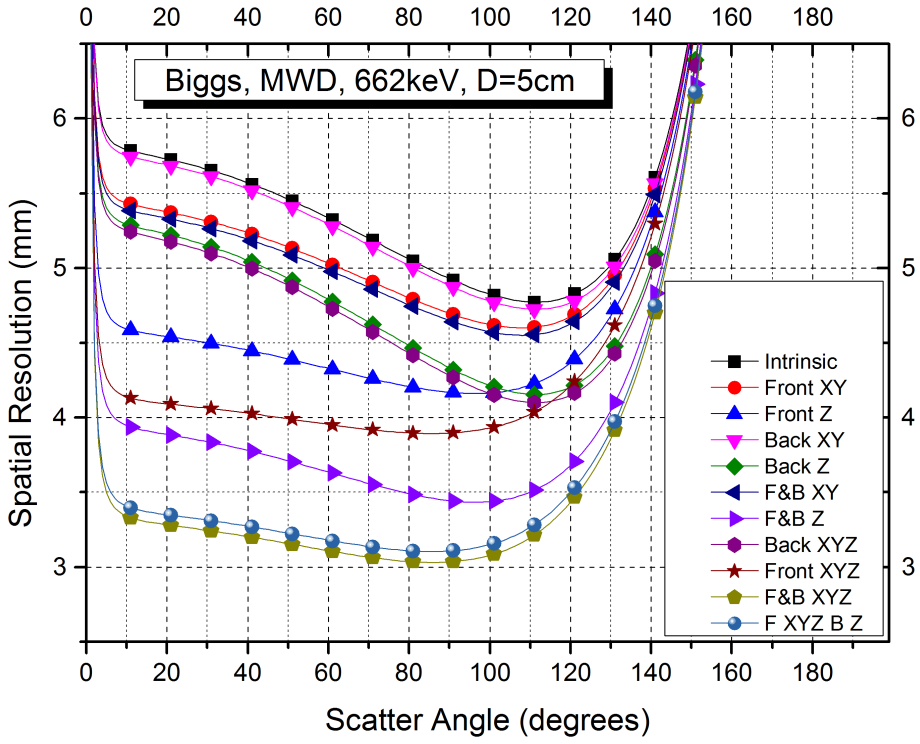

Figure 6.5: Total Spatial Resolution (Biggs, MWD, 662keV, D=5cm)

6.4 Spatial Resolution

The diagram of figure (6.6) shows the positions of six point sources imaged with the UCL Compton camera. All the point sources were at a distance of 1.85cm from the front detector. Although the UCL Compton camera was designed to image objects at a distance of 5cm from the center of the camera, the position of the six point sources were chosen off the center of the camera under the CR pixels and at a closer distance from the camera; this is because the number of pixels available was 20 pixels as noted in section (3.2.4).

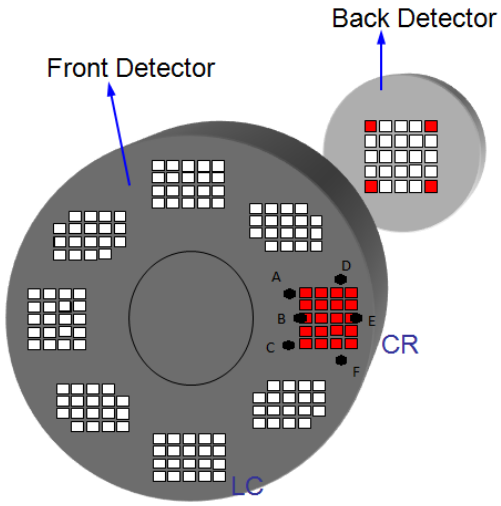

Figure 6.6: Positions of A, B, C, D, E and F point sources

The images obtained from the UCL Compton camera of the six point sources are shown in figures (6.7), (6.8), (6.9) and (6.10). The average error in localizing the point sources is 2mm. The point source E was chosen to study the spatial resolution of the

UCL Compton camera because the source has the largest number of events compared to the other five point sources which makes it more suitable to study the effects of the position sensitivity enhancements of the camera. This is because the number of events that allow position sensitivity enhancements are fewer than the total event number.

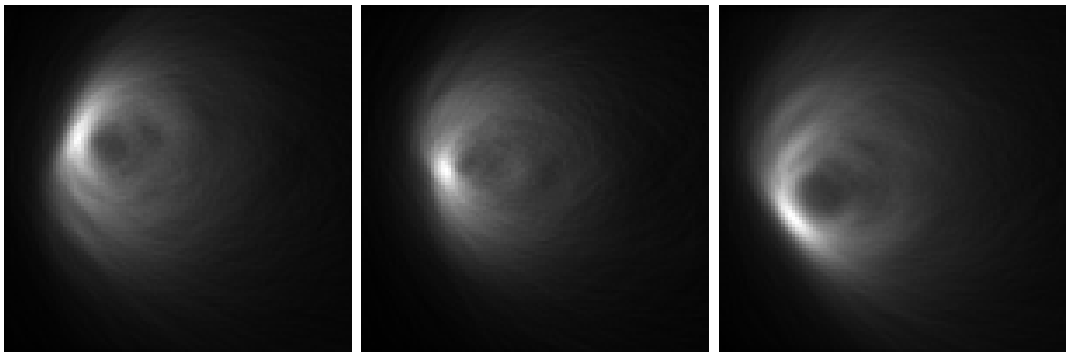

(a) Point Source A (b) Point Source B (c) Point Source C

Figure 6.7: Back projection images of points A, B and C with MWD energy resolution and no position sensitivity enhancements

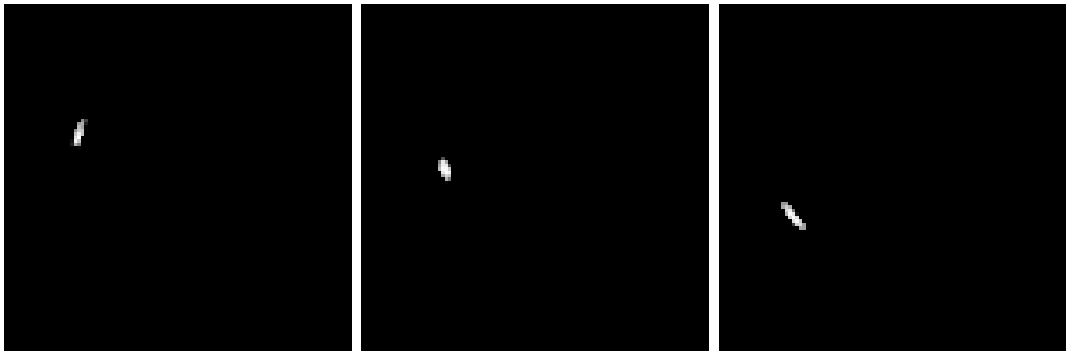

(a) Point Source A (b) Point Source B (c) Point Source C

Figure 6.8: ITEM Reconstruction images of points A, B and C with MWD energy resolution and no position sensitivity enhancements

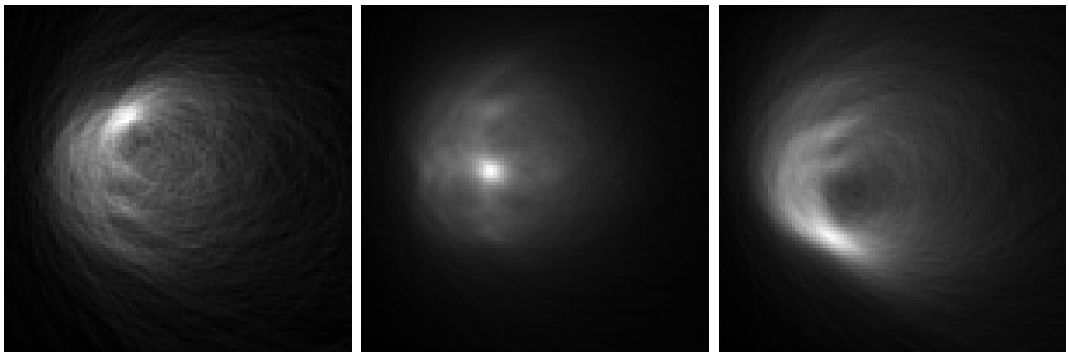

(a) Point Source D (b) Point Source E (c) Point Source F

Figure 6.9: Back projection images of points D, E and F with MWD energy resolution and no position sensitivity enhancements

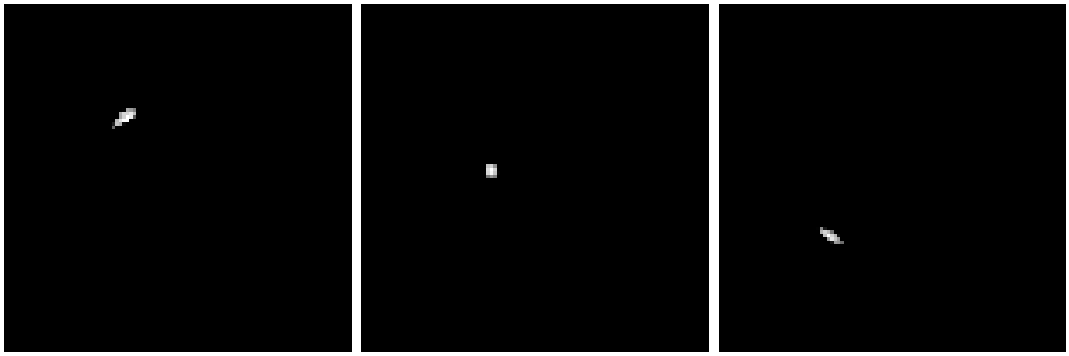

(a) Point Source D (b) Point Source E (c) Point Source F

Figure 6.10: ITEM Reconstruction images of points D, E and F with MWD energy resolution and no position sensitivity enhancements

6.4.1 Predicted Spatial Resolution

The graphs in figures 6.11, 6.12 and 6.13 represents the predicted spatial resolution for a gamma point source of energy 662keV at a distance of 1.85cm from the front detector of the UCL Compton camera. The figures shows graphs of the spatial resolution in function of the scattering angles of intrinsic geometry and the different front detector

position sensitivity enhancements and the three energy resolutions algorithms: MWD, Filtered and UnFiltered.

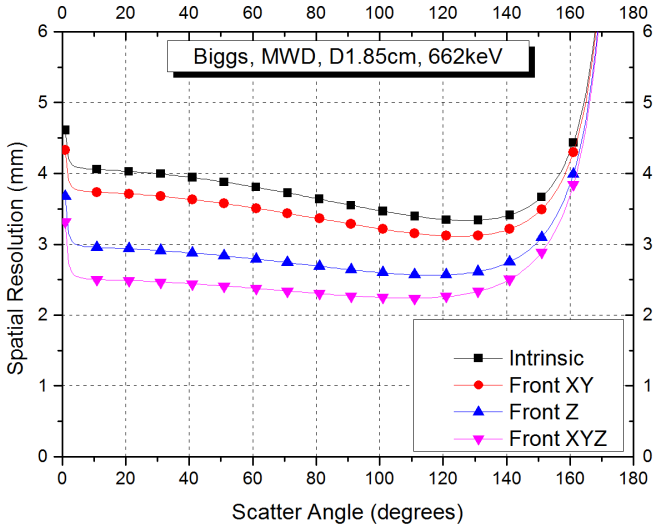

Figure 6.11: Predicted Spatial Resolution (Biggs, MWD, 662keV, D=1.85cm)

Figure 6.11 shows the spatial resolution for the MWD energy resolutions. The average intrinsic spatial resolution for scattering angles between 10° and 150° is about 4mm and by improving the position sensitivity of the front detector by a factor of two, the spatial resolution improves from 4mm to 3.5mm for X-Y improvements, from 4mm to 3mm for the depth PS enhancements and to 2.5mm for X-Y-Z PS enhancements.

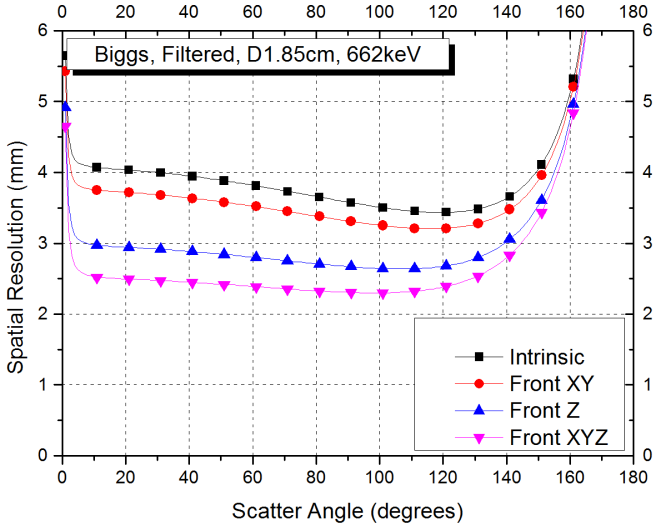

Figure 6.12: Predicted Spatial Resolution (Biggs, Filtered, 662keV, D=1.85cm)

There is no differences between the spatial resolutions for MWD, Filtered and UnFiltered energy resolutions for scattering angles up to 120°. This shows that the UCL Compton camera's spatial resolution is not affected by the energy resolution. The important factor that influences the spatial resolution is the geometry represented in the position sensitivity of the camera.

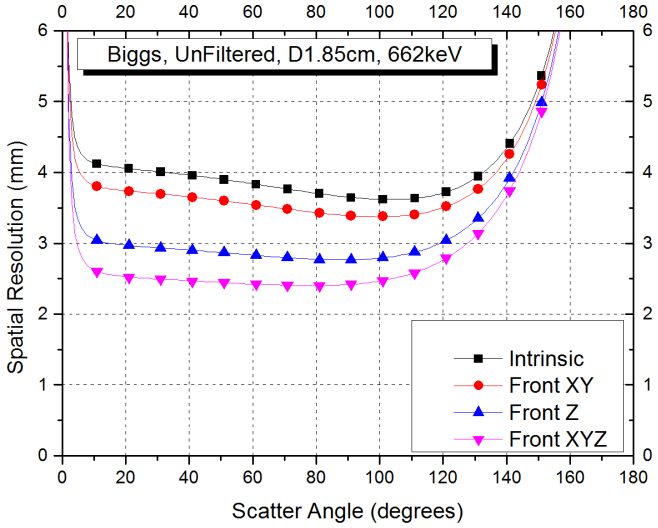

Figure 6.13: Predicted Spatial Resolution (Biggs, UnFiltered, 662keV, D=1.85cm)

6.4.2 Measured Spatial Resolution

Figure 6.14 below shows an image of the E point source with three different energy resolutions. ITEM works very effectively with point sources. All images presented in this thesis it has 100 × 100 pixels with a pixel size of 1 mm. Backprojection and ITEM image are individually normalized to arbitrary scales. The backprojection shows a pronounced intensity maximum within a few mm of the expected position. Most of the artefacts typical to backprojection have been removed by the algorithm. Only the regions with the highest intensity in the backprojection have survived in the ITEM image.

It takes about 14 s to compute the backprojection with 10000 pixels for the 40000 events contained in the data, while the ITEM reconstruction takes about 3 s with

10000 pixels using a 3 GHz Pentium CPU. The reconstruction time is proportional to the number of events and the number of image pixels in the case of backprojection and proportional to the number of image pixels but independent of the number of events in the case of ITEM.

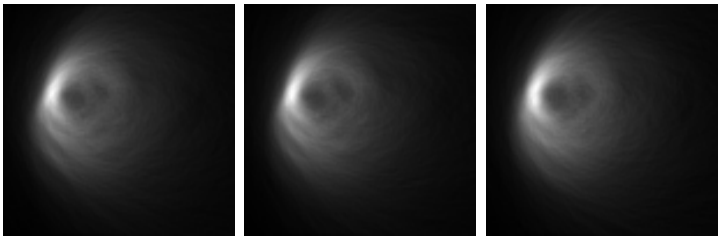

(a) MWD (b) ER=1.7% (c) ER=4%

Figure 6.14: Back projection images of E with three different energy resolutions

(a) MWD (b) ER=1.7% (c) ER=4%

Figure 6.15: ITEM reconstruction images of E with three different energy resolutions

Table 6.7 below summarizes the results obtained when the energy resolution and the position sensitivity are optimized. The spatial resolution of the UCL Compton camera for the point source E has improved by 1.5mm for the energy resolutions of MWD and Filtered. In the case of UnFiltered energy resolutions there is a difference of 1mm between the other two energy resolutions spatial resolutions for the intrinsic

Table 6.7: Point source E Spatial resolution enhancements due to energy resolution and position sensitivity optimization

Energy Resolution	FWHM	FWHM with x-y-z optimization
MWD	9	7.5
Second Algorithm	9	7.5
first Algorithm	10	9

geometry and for the front detector PS enhancements, an improvement of 1mm is seen.

By comparing the predicted spatial resolutions and the measured of the UCL Compton camera, an improvement of 1.5mm in the spatial resolution was seen in both predicted and measured results (for the UnFiltered measured spatial resolution, however, there is only a 1mm improvement). The predictions (section 6.4.1) gave a spatial resolution of only 4mm for the intrinsic and 2.5mm when the position sensitivity on the front detector are implemented; however, the measured spatial resolutions for intrinsic was 9mm and 7mm for the position sensitivity enhancements of the front detector. This big difference between the predicted and the measured spatial resolution is known for all Compton camera's built to date. The explanation agreed on among the Compton camera's researchers is that the reconstruction algorithm has an effect on the spatial resolution which for the UCL Compton camera is dominant.

6.5 Distributed Sources

This section shows the work done using the UCL Compton camera to image distributed and line sources. Two examples are presented to show that the camera is able to image distributed sources. It is worth noting that this section does not promise a detailed study of the imaged distributed sources.

6.5.1 Circular Source

The reconstruction of distributed sources will be discussed with the example of a 270 deg open circle shape with 3 cm diameter. Figures 6.17 and 6.18 represents the backprojection and the ITEM images respectively of the semi circle distributed source. To generate the distributed source a Cs137 point source was mounted onto a rotational stage and continuously moved along a circular path. The path and its relative position in x-y to the front plane pixels (white squares) and the back plane pixels (gray squares) connected to the readout are shown in 6.16.

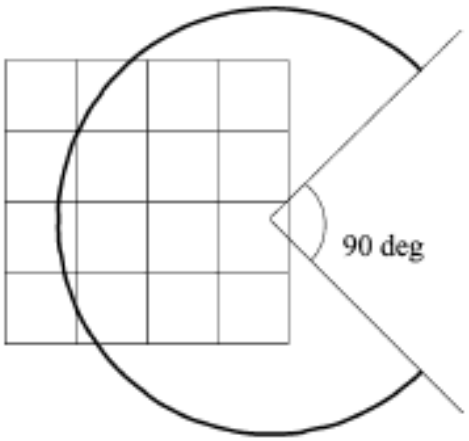

Figure 6.16: Path of the circular source (black line) with respect to the positions of the front pixels

The source distribution was in a plane 2 cm from the front detector. About 70000 events lying in the coincidence window have been collected using the 20 active pixel of the camera. About half of the circular source distribution is reconstructed within a few mm from the expected position. The intensity of the semi circle is fading away along the circular path with increasing distance to the front pixels and decreasing camera sensitivity. In the ITEM image only the parts with the highest contrast with respect to the complex background survived the iterations.

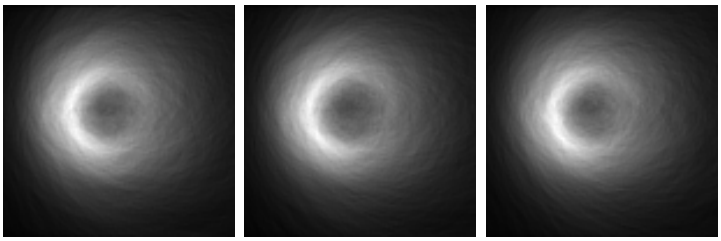

(a) MWD (b) ER=1.7% (c) ER=4%

Figure 6.17: Back projection images of a semi circle distributed source with three different energy resolutions

(a) MWD (b) ER=1.7% (c) ER=4%

Figure 6.18: ITEM reconstruction images of a semi circle distributed source with three different energy resolutions

6.5.2 Line Source

A vertical line source with 4 cm length has been imaged with the UCL Germanium Compton camera. A straight line has been reconstructed at the right position. Figures 6.19 and 6.20 shows the backprojection and the ITEM reconstructed images respectively obtained from the camera. The dimensions of the reconstructed line source are presented in table 6.8. The parts lying in low camera sensitivity regions have low intensity compared to the parts that lay in the regions of high intensity.

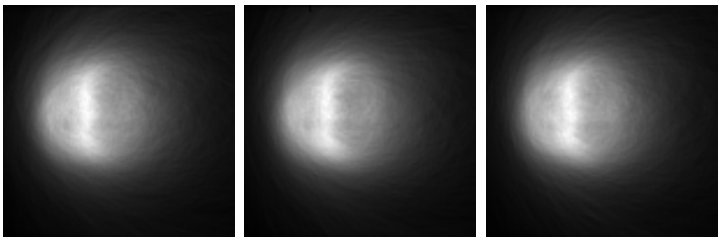

(a) MWD (b) ER=1.7% (c) ER=4%

Figure 6.19: Back projection images of a 4cm line source with three different energy resolutions

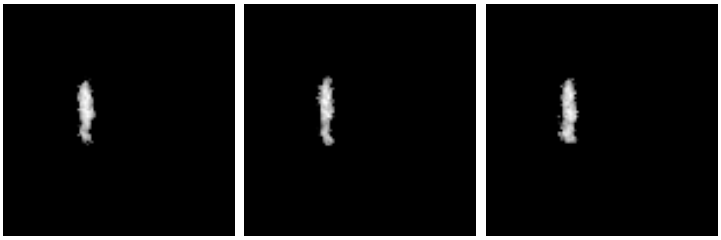

(a) MWD (b) ER=1.7% (c) ER=4%

Figure 6.20: ITEM reconstruction images of a 4cm line source with three different energy resolutions

Table 6.8: Measured dimensions of a vertical 4cm line source for the three energy resolutions algorithms

Energy Resolution	Measured Dimensions
MWD	40
Second Algorithm	39
first Algorithm	40.5

Chapter 7

Conclusions and Future Work

Position sensitivity evaluation of a pixellated germanium Compton camera for nuclear medicine applications is presented. Spatial resolution performances was improved by improving the position sensitivity of the camera in the X-Y by a factor of two from $4 \times 4mm$ to $2 \times 2mm$ for both the front and the back detector and the depth position sensitivity was improved by a factor of two from 5.4mm to 2.27mm for the front detector and from 10.6mm to 5.3mm for the back detector.

Energy resolution of the UCL Compton camera was improved using the MWD algorithm implemented online in the FPGAs of the GRT4 cards. The energy resolution was improved by a factor of of 2 using a simple filter and by a factor of 4 using the MWD. It is proven that for the UCL Compton camera, no matter how good the energy resolution is no improvement was seen (neither from the theoretical predictions nor from the measurements of the PSF of the images of the point sources)on

the spatial resolution of the camera.

Doppler Broadening predicted effects on spatial resolution were presented for the UCL High Purity Germanium Compton camera, and it was shown that, similar to the effects of energy resolution, its effects are negligible on the total spatial resolution of the camera. The geometry of the camera: mainly its pixel size and the separation between the back and the front detector is the dictating factor for the UCL HPGe Compton camera.

To further enhance the spatial resolution for the UCL Compton camera, the work should focus on further enhancing the position sensitivity of the camera, specifically the depth resolution. As seen in the results presented, the depth effects on spatial resolution is dominant compared to the X-Y position sensitivity. Also, the enhancement to the front detector's position sensitivity is more important to that of the back detector because the back detector's position sensitivity only affects the overall spatial resolution by 0.5mm, whereas the enhancement to the front detector's lead to a 2.5mm enhancement to the spatial resolution. To enhance the depth position sensitivity beyond the one presented in this thesis, the pulse shape of the signals from the pixels should be analyzed to find a relationship between depth and the parameters governing the pulse shape: rise time and the gradient at which the signal reaches its maximum. to enhance the X-Y position sensitivity even further, the events where a split charges occurs between adjacent pixels can be used to reconstruct the images;

however, the efficiency of the camera would be decreased if only split charges are considered because the separation between the pixel is 1mm which will reduce the surface area of the front detector to only 31.5% and the back detector to only 33.3%.

To improve the efficiency of the UCL Compton camera, the work should focus on developing faster readout electronics to increase the data rate and reduce dead time. Activating more pixels in addition to the 20 pixels already active will not improve the efficiency any further as the readout electronics maximum data rate transfer of 3.8MB/s is already reached. In fact, for the current setup of the readout electronics, the efficiency will be dramatically decreased.

To improve the spatial resolution of the UCL Compton camera, future work can study the effects of split charges between neighboring pixels. Because the separation between the pixels is 1mm, the expected position sensitivity is 1/2 mm. The remaining of 125 pixels has to be activated to test the whole camera, and for the readout electronics when all the pixels are activated must be redesigned to cope with the high rate of data.

Appendix A

Energy Resolution Measurements

A.1 Back Detector Energy Resolution

Energy	ER	ER	ER	ER
keV	%	%	%	%
	BC11 NIM	BC11 MWD	BC11 Filtered	BC11 UnFiltered
32	7.63	6.38	10.63	18.75
60	--	3.88	7.07	9.73
81	2.98	--	--	--
276	0.79	--	--	--
303	0.81	--	--	--
356	0.70	--	--	--
384	0.60	--	--	--
662	0.35	0.4	0.7	1.33

(a) Tabulated Energy resolution in percentage

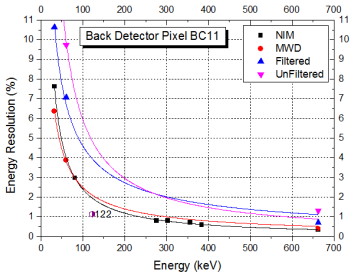

(b) Graphs of energy resolution in percentage

Figure A.1: Energy resolution of BC11

Energy	ER	ER	ER	ER
keV	%	%	%	%
	BC12 NIM	BC12 MWD	BC12 Filtered	BC12 UnFiltered
32	5.59	4.47	10.44	--
60	--	2.86	7.12	9.8
81	2.42	--	--	--
276	0.61	--	--	--
303	0.67	--	--	--
356	0.55	--	--	--
384	0.54	--	--	--
662	0.34	0.32	0.72	1.3

(a) Tabulated Energy resolution in percentage

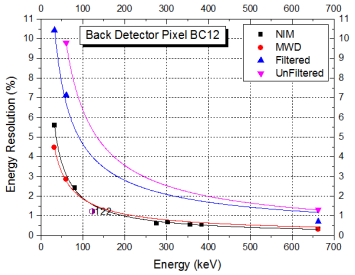

(b) Graphs of energy resolution in percentage

Figure A.2: Energy resolution of BC12

Energy	ER	ER	ER	ER
keV	%	%	%	%
	BC13 NIM	BC13 MWD	BC13 Filtered	BC13 UnFiltered
32	9.28	4.66	9.75	
60	--	2.81	6.65	10.22
81	3.52	--	--	--
276	0.88	--	--	--
303	0.87	--	--	--
356	0.81	--	--	--
384	0.78	--	--	--
662	0.47	0.31	0.67	1.27

(a) Tabulated Energy resolution in percentage

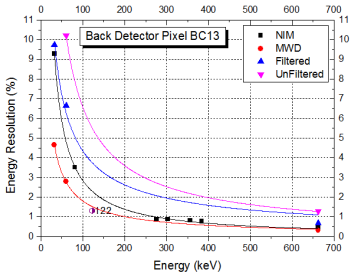

(b) Graphs of energy resolution in percentage

Figure A.3: Energy resolution of BC13

Energy	ER	ER	ER	ER
keV	%	%	%	%
	BC15 NIM	BC15 MWD	BC15 Filtered	BC15 UnFiltered
32	5.63	4.53		
60	--	2.81	6.83	9.7
81	2.17	--	--	--
276	0.7	--	--	--
303	0.55	--	--	--
356	0.57		--	--
384	0.52	--	--	--
662	0.31	0.31	0.72	1.34

(a) Tabulated Energy resolution in percentage

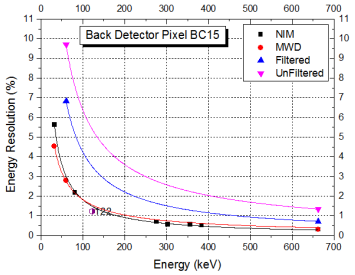

(b) Graphs of energy resolution in percentage

Figure A.4: Energy resolution of BC15

Energy	ER	ER	ER	ER
keV	%	%	%	%
	BC21 NIM	BC21 MWD	BC21 Filtered	BC21 UnFiltered
32	6.41	4.84		
60	--	2.82	7.03	9.26
81	2.41	--	--	--
276	0.74	--	--	--
303	0.64	--	--	--
356	0.57	--	--	--
384	0.45	--	--	--
662	0.3	0.31	0.69	1.31

(a) Tabulated Energy resolution in percentage

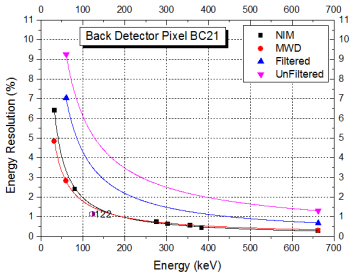

(b) Graphs of energy resolution in percentage

Figure A.5: Energy resolution of BC21

Energy	ER	ER	ER	ER
keV	%	%	%	%
	BC22 NIM	BC22 MWD	BC22 Filtered	BC22 UnFiltered
32	9.34	4.84		
60	--	2.71	6.75	9.26
81	3.33	--	--	--
276	1.04	--	--	--
303	0.96	--	--	--
356	0.8	--	--	--
384	0.92	--	--	--
662	0.55	0.32	0.71	1.3

(a) Tabulated Energy resolution in percentage

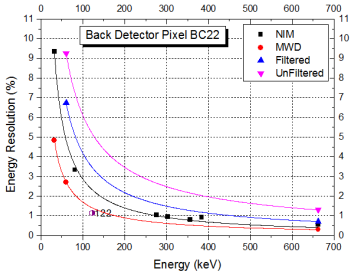

(b) Graphs of energy resolution in percentage

Figure A.6: Energy resolution of BC22

Energy	ER	ER	ER	ER
keV	%	%	%	%
	BC25 NIM	BC25 MWD	BC25 Filtered	BC25 UnFiltered
32	6.28	4.69		
60	--	2.96	7.22	9.88
81	2.3	--	--	--
276	0.79	--	--	--
303	0.68	--	--	--
356	0.59	--	--	--
384	0.52	--	--	--
662	0.34	0.32	0.69	1.4

(a) Tabulated Energy resolution in percentage

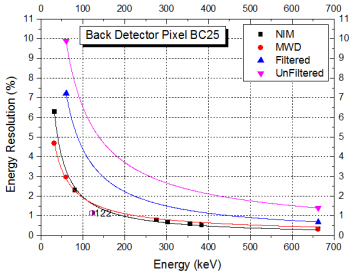

(b) Graphs of energy resolution in percentage

Figure A.7: Energy resolution of BC25

Energy	ER	ER	ER	ER
keV	%	%	%	%
	BC32 NIM	BC32 MWD	BC32 Filtered	BC32 UnFiltered
32	6.75	6.25		
60	--	3.98	6.82	9.48
81	2.62	--	--	--
276	0.73	--	--	--
303	0.72	--	--	--
356	0.62	--	--	--
384	0.61	--	--	--
662	0.37	0.39	0.68	1.2

(a) Tabulated Energy resolution in percentage

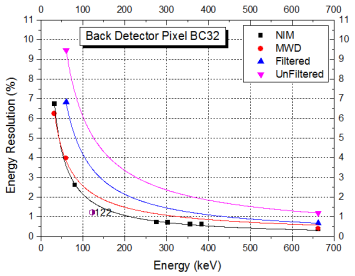

(b) Graphs of energy resolution in percentage

Figure A.8: Energy resolution of BC32

Energy	ER	ER	ER	ER
keV	%	%	%	%
	BC35 NIM	BC35 MWD	BC35 Filtered	BC35 UnFiltered
32	6.69	4.59		
60	--	2.99	8.25	10.27
81	2.57	--	--	--
276	0.82	--	--	--
303	0.72	--	--	--
356	0.59	--	--	--
384	0.51	--	--	--
662	0.32	0.31	0.87	1.34

(a) Tabulated Energy resolution in percentage

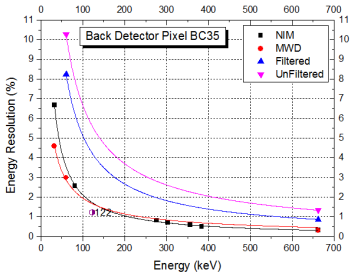

(b) Graphs of energy resolution in percentage

Figure A.9: Energy resolution of BC35

Energy	ER	ER	ER	ER
keV	%	%	%	%
	BC41 NIM	BC41 MWD	BC41 Filtered	BC41 UnFiltered
32	6	4.94		
60	--	2.79	6.9	9.58
81	2.33	--	--	--
276	0.67	--	--	--
303	0.63	--	--	--
356	0.56	--	--	--
384	0.55	--	--	--
662	0.35	0.3	0.69	1.22

(a) Tabulated Energy resolution in percentage

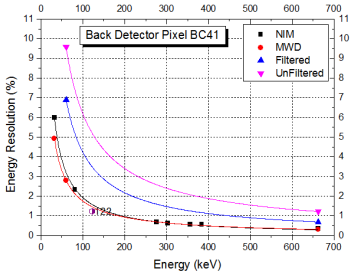

(b) Graphs of energy resolution in percentage

Figure A.10: Energy resolution of BC41

Energy	ER	ER	ER	ER
keV	%	%	%	%
	BC42 NIM	BC42 MWD	BC42 Filtered	BC42 UnFiltered
32	9	4.97		
60	--	2.79	6.95	9.13
81	3.38	--	--	--
276	1.01	--	--	--
303	0.96	--	--	--
356	0.81	--	--	--
384	0.68	--	--	--
662	0.42	0.35	0.74	1.16

(a) Tabulated Energy resolution in percentage

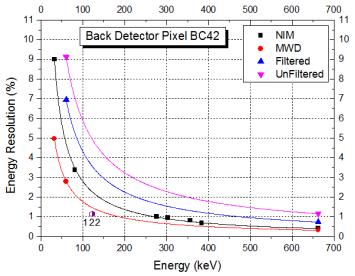

(b) Graphs of energy resolution in percentage

Figure A.11: Energy resolution of BC42

Energy	ER	ER	ER	ER
keV	%	%	%	%
	BC43 NIM	BC43 MWD	BC43 Filtered	BC43 UnFiltered
32	6.19	4.88		
60	--	2.84	7.02	9.88
81	2.43	--	--	--
276	0.77	--	--	--
303	0.64	--	--	--
356	0.56	--	--	--
384	0.54	--	--	--
662	0.34	0.35	0.74	1.24

(a) Tabulated Energy resolution in percentage

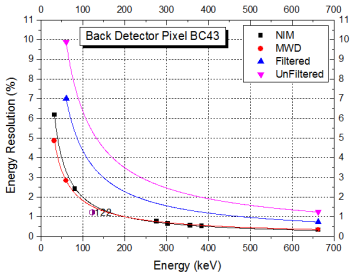

(b) Graphs of energy resolution in percentage

Figure A.12: Energy resolution of BC43

Energy	ER	ER	ER	ER
keV	%	%	%	%
	BC51 NIM	BC51 MWD	BC51 Filtered	BC51 UnFiltere
32	6.53	6.25		
60	--	3.01	6.68	8.94
81	2.44	--	--	--
276	0.75	--	--	--
303	0.68	--	--	--
356	0.6	--	--	--
384	0.59	--	--	--
662	0.36	0.35	0.71	1.29

(a) Tabulated Energy resolution in percentage

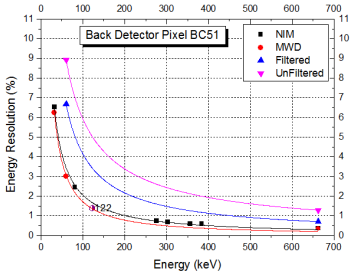

(b) Graphs of energy resolution in percentage

Figure A.13: Energy resolution of BC51

Energy	ER	ER	ER	ER
keV	%	%	%	%
	BC52 NIM	BC52 MWD	BC52 Filtered	BC52 UnFiltered
32	7.06	4.97		
60	--	3.28	7.08	9.93
81	2.6	--	--	--
276	0.83	--	--	--
303	0.75	--	--	--
356	0.68	--	--	--
384	0.66	--	--	--
662	0.4	0.42	0.73	1.34

(a) Tabulated Energy resolution in percentage

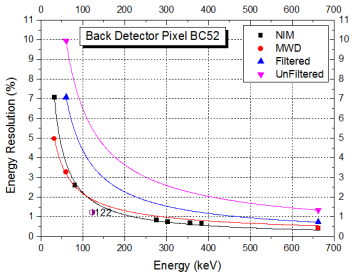

(b) Graphs of energy resolution in percentage

Figure A.14: Energy resolution of BC52

Energy	ER	ER	ER	ER
keV	%	%	%	%
	BC53 NIM	BC53 MWD	BC53 Filtered	BC53 UnFiltered
32	8.91	4.59		
60	--	2.67	6.57	8.67
81	3.37	--	--	--
276	0.64	--	--	--
303	0.97	--	--	--
356	0.86	--	--	--
384	0.83	--	--	--
662	0.49	0.41	0.73	1.17

(a) Tabulated Energy resolution in percentage

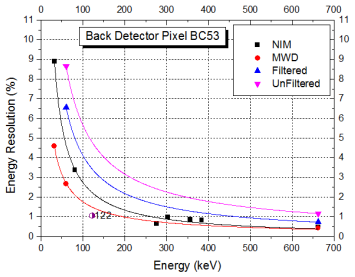

(b) Graphs of energy resolution in percentage

Figure A.15: Energy resolution of BC53

Energy	ER	ER	ER	ER
keV	%	%	%	%
	BC54 NIM	BC54 MWD	BC54 Filtered	BC54 UnFiltered
32	8.44	8.34		
60	--	4.96	7.15	9.82
81	3.58	--	--	--
276	1.04	--	--	--
303	0.97	--	--	--
356	0.84	--	--	--
384	0.76	--	--	--
662	0.45	0.49	0.72	1.26

(a) Tabulated Energy resolution in percentage

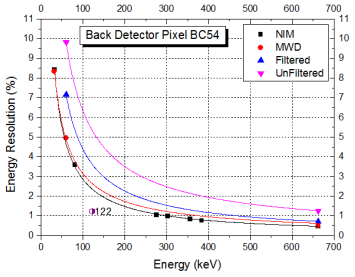

(b) Graphs of energy resolution in percentage

Figure A.16: Energy resolution of BC54

A.2 Front Detector Energy Resolution

Energy keV	ER % CR11 NIM	ER % CR11 MWD	ER % CR11 Filtered	ER % CR11 UnFiltered
32	--	5.25	9.84	--
60	--	2.74	6.45	9.45
81	--	1.98	4.89	--
276	0.62	0.59	1.52	--
303	0.56	0.55	1.49	2.61
356	0.51	0.5	1.25	2.26
384	0.48	0.5	1	--
662	0.3	0.31	0.73	1.33

(a) Tabulated Energy resolution in percentage

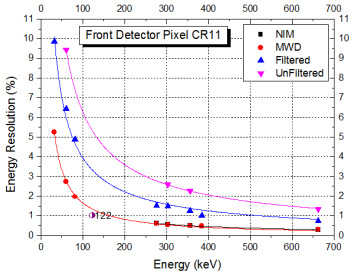

(b) Graphs of energy resolution in percentage

Figure A.17: Energy resolution of CR11

Energy keV	ER % CR12 NIM	ER % CR12 MWD	ER % CR12 Filtered	ER % CR12 UnFiltered
32	--	5.84	10.16	--
60	--	3.13	7.18	10.2
81	--	2.35	4.99	--
276	0.6	0.72	1.59	--
303	0.55	0.65	1.46	2.42
356	0.5	0.55	1.28	2.26
384	0.47	0.51	1.04	--
662	0.29	0.34	0.68	1.34

(a) Tabulated Energy resolution in percentage

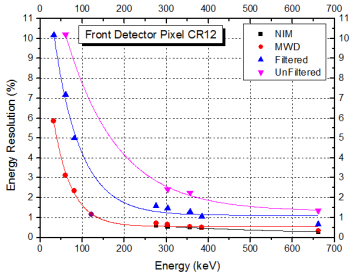

(b) Graphs of energy resolution in percentage

Figure A.18: Energy resolution of CR12

Energy keV	ER % CR14 NIM	ER % CR14 MWD	ER % CR14 Filtered	ER % CR14 UnFiltered
32		6.03	11.56	
60		3.34	7.24	10.05
81		2.32	5.01	--
276	0.61	0.7	1.44	--
303	0.58	0.66	1.5	1.95
356	0.5	0.57	1.2	2.09
384	0.42	0.52	1.05	--
662	0.27	0.33	0.7	1.01

(a) Tabulated Energy resolution in percentage

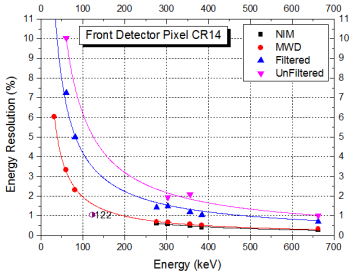

(b) Graphs of energy resolution in percentage

Figure A.19: Energy resolution of CR14

Energy	ER	ER	ER	ER
keV	%	%	%	%
	CR21 NIM	CR21 MWD	CR21 Filtered	CR21 UnFiltered
32		5.53	9.69	
60		3.28	7.11	10.45
81		2.32	5.15	--
276	0.65	0.69	1.46	--
303	0.58	0.64	1.38	2.17
356	0.51	0.55	1.29	2.17
384	0.54	0.52	1.13	--
662	0.31	0.34	0.66	1.25

(a) Tabulated Energy resolution in percentage

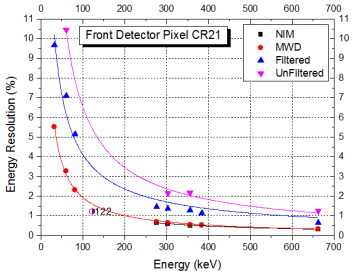

(b) Graphs of energy resolution in percentage

Figure A.20: Energy resolution of CR21

Energy	ER	ER	ER	ER
keV	%	%	%	%
	CR22 NIM	CR22 MWD	CR22 Filtered	CR22 UnFiltered
32		5.78	10	
60		3.71	8.57	10.44
81		2.43	5.04	--
276	0.62	0.73	1.55	--
303	0.62	0.72	1.29	2.47
356	0.54	0.62	1.26	2.24
384	0.49	0.57	1.09	--
662	0.3	0.37	0.7	1.32

(a) Tabulated Energy resolution in percentage

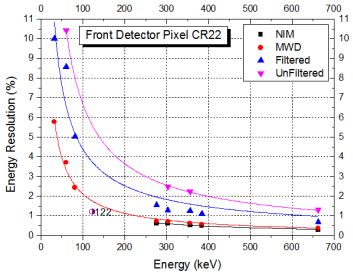

(b) Graphs of energy resolution in percentage

Figure A.21: Energy resolution of CR22

Energy	ER	ER	ER	ER
keV	%	%	%	%
	CR23 NIM	CR23 MWD	CR23 Filtered	CR23 UnFiltered
32	--	9.22	12.81	
60	--	5.41	8.57	10.61
81	--	3.95	5.8	--
276	0.69	1.11	1.75	--
303	0.64	1.09	1.78	2.47
356	0.55	0.85	1.52	2.27
384	0.49	0.83	1.38	--
662	0.29	0.5	0.87	1.38

(a) Tabulated Energy resolution in percentage

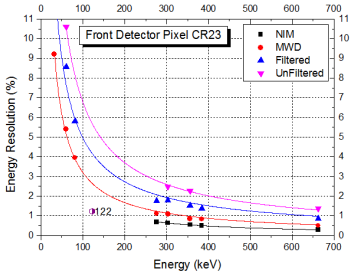

(b) Graphs of energy resolution in percentage

Figure A.22: Energy resolution of CR23

Energy	ER	ER	ER	ER
keV	%	%	%	%
	CR24 NIM	CR24 MWD	CR24 Filtered	CR24 UnFiltered
32		7.5	10.25	
60		4.03	7.5	10.79
81		3.05	5.23	--
276	0.66	0.87	1.62	--
303	0.57	0.79	1.42	2.69
356	0.51	0.72	1.34	2.52
384	0.48	0.72	1.23	--
662	0.3	0.44	0.75	1.29

(a) Tabulated Energy resolution in percentage

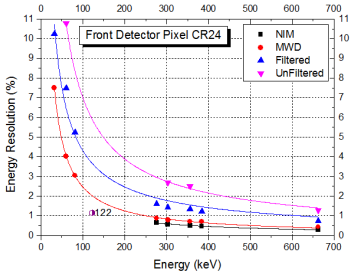

(b) Graphs of energy resolution in percentage

Figure A.23: Energy resolution of CR24

Energy	ER	ER	ER	ER
keV	%	%	%	%
	CR33 NIM	CR33 MWD	CR33 Filtered	CR33 UnFiltered
32		5.78	12.5	
60		3.08	6.82	10.35
81		1.98	5.47	--
276	0.67	0.65	1.62	--
303	0.57	0.6	1.42	2.61
356	0.52	0.52	1.24	2.29
384	0.44	0.49	0.88	--
662	0.27	0.34	0.72	1.28

(a) Tabulated Energy resolution in percentage

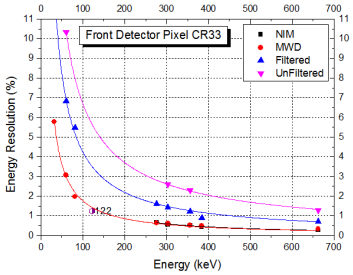

(b) Graphs of energy resolution in percentage

Figure A.24: Energy resolution of CR33

Energy	ER	ER	ER	ER
keV	%	%	%	%
	CR34 NIM	CR34 MWD	CR34 Filtered	CR34 UnFiltered
32		5.81	9.69	
60		3.39	7.36	11.26
81		2.31	4.96	--
276	0.66	0.65	1.26	--
303	0.61	0.66	1.3	2.68
356	0.5	0.57	1.23	2.56
384	0.53	0.53	0.89	--
662	0.29	0.34	0.66	1.22

(a) Tabulated Energy resolution in percentage

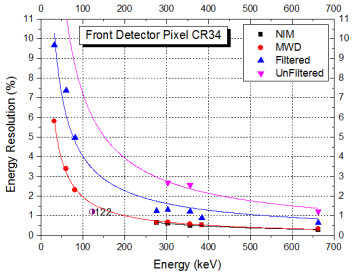

(b) Graphs of energy resolution in percentage

Figure A.25: Energy resolution of CR34

Energy	ER	ER	ER	ER
keV	%	%	%	%
	CR42 NIM	CR42 MWD	CR42 Filtered	CR42 UnFiltered
32		5.22	9.41	
60		2.97	7.7	11.58
81		2.12	5.23	--
276	0.64	0.64	1.67	--
303	0.56	0.62	1.24	2.48
356	0.54	0.52	1.27	2.63
384	0.5	0.45	1.02	--
662	0.31	0.32	0.74	1.53

(a) Tabulated Energy resolution in percentage

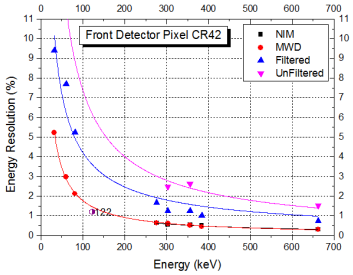

(b) Graphs of energy resolution in percentage

Figure A.26: Energy resolution of CR42

Energy	ER	ER	ER	ER
keV	%	%	%	%
	CR43 NIM	CR43 MWD	CR43 Filtered	CR43 UnFiltered
32		5.53	12.66	
60		3.29	6.54	9.95
81		2.25	5.8	--
276	0.65	0.75	1.57	--
303	0.59	0.67	1.54	2.47
356	0.48	0.57	1.32	2.37
384	0.45	0.5	1.04	--
662	0.29	0.32	0.76	1.29

(a) Tabulated Energy resolution in percentage

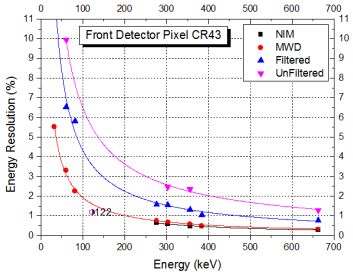

(b) Graphs of energy resolution in percentage

Figure A.27: Energy resolution of CR43

Energy	ER	ER	ER	ER
keV	%	%	%	%
	CR44 NIM	CR44 MWD	CR44 Filtered	CR44 UnFiltered
32		7.06	10.5	
60		4.79	7.11	10.87
81		3.25	5.01	--
276	0.67	0.97	1.61	--
303	0.58	0.99	1.34	2.58
356	0.5	0.77	1.24	2.28
384	0.51	0.55	1	--
662	0.29	0.45	0.62	1.42

(a) Tabulated Energy resolution in percentage

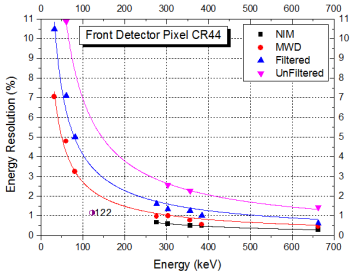

(b) Graphs of energy resolution in percentage

Figure A.28: Energy resolution of CR44

Energy	ER	ER	ER	ER
keV	%	%	%	%
	LC11 NIM	LC11 MWD	LC11 Filtered	LC11 UnFiltered
32		6.69	11.69	29.16
60		3.7	6.99	11.06
81	2.93	--	--	--
276	0.88	--	--	--
303	0.76	--	--	--
356	0.68	--	--	--
384	0.63	--	--	--
662	0.35	0.4	0.71	1.24

(a) Tabulated Energy resolution in percentage

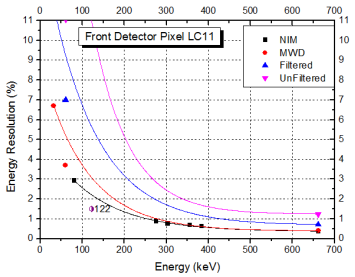

(b) Graphs of energy resolution in percentage

Figure A.29: Energy resolution of LC11

Energy	ER	ER	ER	ER
keV	%	%	%	%
	LC12 NIM	LC12 MWD	LC12 Filtered	LC12 UnFiltered
32		--	10.75	28.59
60		--	6.86	10.02
81	2.54	--	--	--
276	0.74	--	--	--
303	0.66	--	--	--
356	0.59	--	--	--
384	0.57	--	--	--
662	0.6	--	0.68	1.26

(a) Tabulated Energy resolution in percentage

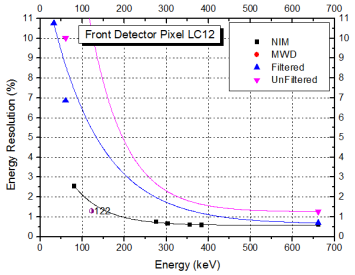

(b) Graphs of energy resolution in percentage

Figure A.30: Energy resolution of LC12

Energy	ER	ER	ER	ER
keV	%	%	%	%
	LC13 NIM	LC13 MWD	LC13 Filtered	LC13 UnFiltered
32		5.66	10.28	28.69
60		2.76	7.01	10.69
81	2.43	--	--	--
276	0.61	--	--	--
303	0.66	--	--	--
356	0.57	--	--	--
384	0.53	--	--	--
662	0.39	0.38	0.75	1.37

(a) Tabulated Energy resolution in percentage

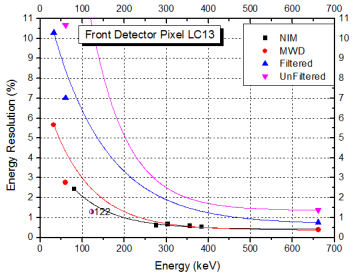

(b) Graphs of energy resolution in percentage

Figure A.31: Energy resolution of LC13

Energy	ER	ER	ER	ER
keV	%	%	%	%
	LC14 NIM	LC14 MWD	LC14 Filtered	LC14 UnFiltered
32		8.56	10.41	29.38
60		6.34	7.09	10.44
81	2.84	--	--	--
276	0.79	--	--	--
303	0.7	--	--	--
356	0.63	--	--	--
384	0.61	--	--	--
662	0.57	0.55	0.73	1.28

(a) Tabulated Energy resolution in percentage

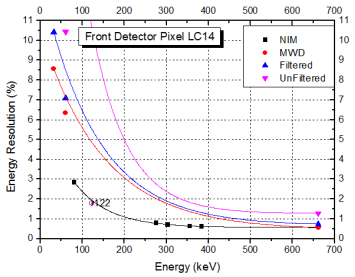

(b) Graphs of energy resolution in percentage

Figure A.32: Energy resolution of LC14

Energy	ER	ER	ER	ER
keV	%	%	%	%
	LC21 NIM	LC21 MWD	LC21 Filtered	LC21 UnFiltered
32		5.59	10.53	29.66
60		2.81	6.94	10.25
81	2.22	--	--	--
276	0.74	--	--	--
303	0.66	--	--	--
356	0.58	--	--	--
384	0.47	--	--	--
662	0.32	0.34	0.69	1.29

(a) Tabulated Energy resolution in percentage

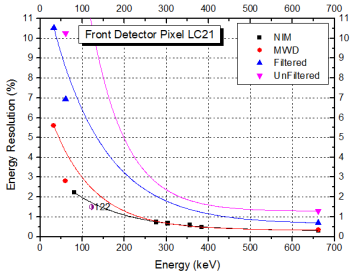

(b) Graphs of energy resolution in percentage

Figure A.33: Energy resolution of LC21

Energy	ER	ER	ER	ER
keV	%	%	%	%
	LC22 NIM	LC22 MWD	LC22 Filtered	LC22 UnFiltered
32		5.56	11.44	25.28
60		2.76	6.59	9.88
81	2.17	--	--	--
276	0.52	--	--	--
303	0.6	--	--	--
356	0.53	--	--	--
384	0.43	--	--	--
662	0.32	0.32	0.68	1.18

(a) Tabulated Energy resolution in percentage

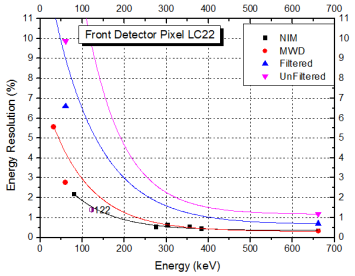

(b) Graphs of energy resolution in percentage

Figure A.34: Energy resolution of LC22

Energy	ER	ER	ER	ER
keV	%	%	%	%
	LC23 NIM	LC23 MWD	LC23 Filtered	LC23 UnFiltered
32		9.44	10.44	29.47
60		6.55	7.26	10.22
81	2.72	--	--	--
276	0.77	--	--	--
303	0.72	--	--	--
356	0.63	--	--	--
384	0.56	--	--	--
662	0.61	0.59	0.74	1.35

(a) Tabulated Energy resolution in percentage

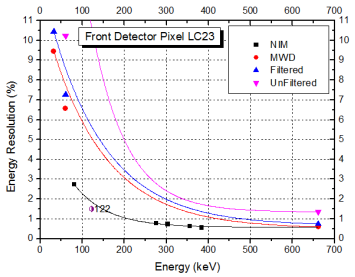

(b) Graphs of energy resolution in percentage

Figure A.35: Energy resolution of LC23

Energy	ER	ER	ER	ER
keV	%	%	%	%
	LC31 NIM	LC31 MWD	LC31 Filtered	LC31 UnFiltered
32		5.72	10.16	27.81
60		2.89	6.67	10.59
81	2.54	--	--	--
276	0.71	--	--	--
303	0.67	--	--	--
356	0.58	--	--	--
384	0.53	--	--	--
662	0.34	0.34	0.71	1.29

(a) Tabulated Energy resolution in percentage

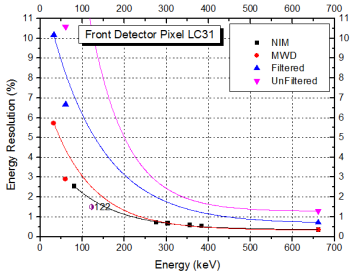

(b) Graphs of energy resolution in percentage

Figure A.36: Energy resolution of LC31

Energy	ER	ER	ER	ER
keV	%	%	%	%
	LC32 NIM	LC32 MWD	LC32 Filtered	LC32 UnFiltered
32		5.66	10.13	29.13
60		2.84	6.86	10.18
81	2.21	--	--	--
276	0.73	--	--	--
303	0.69	--	--	--
356	0.58	--	--	--
384	0.52	--	--	--
662	0.33	0.35	0.71	1.3

(a) Tabulated Energy resolution in percentage

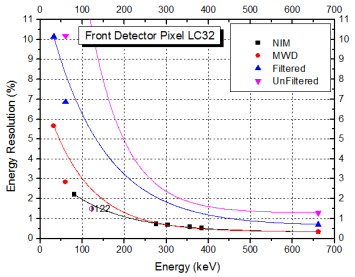

(b) Graphs of energy resolution in percentage

Figure A.37: Energy resolution of LC32

Energy keV	ER % LC33 NIM	ER % LC33 MWD	ER % LC33 Filtered	ER % LC33 UnFiltered
32		6.31	12.09	26.88
60		2.82	6.52	9.71
81	2.17	--	--	--
276	0.67	--	--	--
303	0.64	--	--	--
356	0.53	--	--	--
384	0.46	--	--	--
662	0.32	0.35	0.67	1.17

(a) Tabulated Energy resolution in percentage

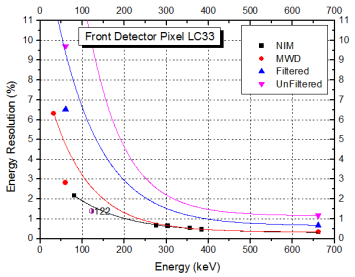

(b) Graphs of energy resolution in percentage

Figure A.38: Energy resolution of LC33

A.3 Back Detector Noise Measurements

Pixels	ER at 662 keV	FWHM	Noise Amplitude ADC Channel
BC11	2.66	28.47	67.89
BC12	2.1	26.86	65.19
BC13	2.02	27.96	68.96
BC14	2	26.78	65.69
BC15	2.08	27.81	66.27
BC21	2.03	27.025	67.438
BC22	2.09	27.118	66.27
BC23	5.12	26.75	65.38
BC24	--	--	--
BC25	2.12	27.14	66.1
BC31	--	--	--
BC32	2.59	26.72	65.889
BC33	--	--	--
BC34	--	--	--
BC35	2.06	35.539	82.959
BC41	2.01	27.06	66.665
BC42	2.31	30.34	73.39
BC43	2.34	29.24	70.78
BC44	--	--	--
BC45	--	--	--
BC51	2.33	29.74	78.16
BC52	2.79	26.99	66.44
BC53	2.74	29.71	72.13
BC54	3.24	26.65	65.04
BC55	3.3	28.19	69.2

Figure A.39: Back detector noise amplitude measurements

Bibliography

Alavi, A., & Basu, S. 2008. Planar and SPECT imaging in the era of PET and PET–CT: can it survive the test of time? *European journal of nuclear medicine and molecular imaging*, **35**(8), 1554–1559.

An, S.H., Seo, H., Lee, J.H., Lee, C.S., Lee, J.S., & Kim, C.H. 2007a. Effect of detector parameters on the image quality of Compton camera for 99mTc. *Nuclear Instruments and Methods in Physics Research Section A: Accelerators, Spectrometers, Detectors and Associated Equipment*, **571**(1-2), 251 – 254.

An, So Hyun, Seo, Hee, & Kim, Chan Hyeong. 2007b. Optimization of a table-top Compton camera system by Monte Carlo simulation. *Nuclear Instruments and Methods in Physics Research Section A: Accelerators, Spectrometers, Detectors and Associated Equipment*, **580**(1), 169 – 172.

Asma, Evren, & Manjeshwar, Ravindra. 2008 (oct.). Evaluation of the impact of resolution-sensitivity tradeoffs on detection performance for SPECT imaging. *Pages 3730 –3733 of: Nuclear Science Symposium Conference Record, 2008. NSS '08. IEEE.*

Ballinger, James. 2008. Re: Planar and SPECT imaging in the era of PET and PET-CT: can it survive the test of time? *European Journal of Nuclear Medicine and Molecular Imaging*, **35**, 2340–2340. 10.1007/s00259-008-0957-0.

Basko, R., Zeng, G.L., & Gullberg, G.T. 1997. Analytical reconstruction formula for one-dimensional Compton camera. *Nuclear Science, IEEE Transactions on*, **44**(3), 1342–1346.

Bengel, Frank M., Higuchi, Takahiro, Javadi, Mehrbod S., & Lautamki, Riikka. 2009. Cardiac Positron Emission Tomography. *Journal of the American College of Cardiology*, **54**(1), 1 – 15.

Bernabeu, J., Clinthorne, N. H., Dewaraja, Y., Lacasta, C., Llos, G., Mikuz, M., Roe, S., Rogers, W. L., Studen, A., Weilhammer, P., Zhang, L., & Zontar, D. 2004. Development of a high efficiency and high resolution Compton probe for prostate imaging. *Nuclear Instruments and Methods in Physics Research Section A: Accelerators, Spectrometers, Detectors and Associated Equipment*, **527**(1-2), 58 – 61.

Biggs, F., Mendelsohn, L.B., & Mann, J.B. 1975. Hartree-Fock Compton profiles for the elements. *Atomic Data and Nuclear Data Tables*, **16**(3), 201 – 309.

Bolozdynya, A.I., Egorov, V.V., Koutchenkov, A.V., Safronov, G.A., Smirnov, G.N., Medved, S.A., & Morgunov, V.L. 1997. High pressure xenon electronically collimated camera for low energy gamma ray imaging. *Nuclear Science, IEEE Transactions on*, **44**(6), 2408–2414.

Boston, H.C., Gillam, J., Boston, A.J., Cooper, R.J., Cresswell, J., Grint, A.N., Mather, A.R., Nolan, P.J., Scraggs, D.P., Turk, G., Hall, C.J., Lazarus, I., Berry, A., Beveridge, T., & Lewis, R. 2007. Orthogonal strip HPGe planar SmartPET detectors in Compton configuration. *Nuclear Instruments and Methods in Physics Research Section A: Accelerators, Spectrometers, Detectors and Associated Equipment*, **580**(2), 929 – 933.

Brechner, R.R., Singh, M., & Leahy, R. 1987. Computer Simulated Studies of Tomographic Reconstruction with an Electronically Collimated Camera for SPECT. *Nuclear Science, IEEE Transactions on*, **34**(1), 369–373.

Castoldi, A., Galimberti, A., Guazzoni, C., Strder, L., & Walenta, A. H. 2006. A Novel Scatter Detector for High-Resolution SPECT Imaging With Compton Telescopes. *Nuclear Science, IEEE Transactions on*, **53**(6), 3912–3917.

Cerqueira, Manuel. 2010. Diagnosis and prognosis of coronary artery disease: PET is superior to SPECT: Con. *Journal of Nuclear Cardiology*, **17**, 678–682. 10.1007/s12350-010-9254-y.

Cherry, Simon R. 2004. In vivo molecular and genomic imaging: new challenges for imaging physics. *Physics in Medicine and Biology*, **49**(3), R13.

Clinthorne, Neal H., yi Ng, Chor, Strobel, Joerg, ho Hua, Chia, LeBlanc, James W., Wilderman, Scott J., & Rogers, W. Leslie. 1998. Determining detector requirements for medical imaging applications. *Nuclear Instruments and Methods in Physics Research Section A: Accelerators, Spectrometers, Detectors and Associated Equipment*, **409**(1-3), 501 – 507.

Conka-Nurdan, T., Nurdan, K., Constantinescu, F., Freisleben, B., Pavel, N.A., & Walenta, A.H. 2002. Impact of the detector parameters on a Compton camera. *Nuclear Science, IEEE Transactions on*, **49**(3), 817–821.

Conka-Nurdan, T., Nurdan, K., Laihem, K., Walenta, A.H., Fiorini, C., Freisleben, B., Hornel, N., Pavel, N.A., & Struder, L. 2004. Preliminary results on Compton electrons in silicon drift detector. *Nuclear Science, IEEE Transactions on*, **51**(5), 2526–2532.

Conka-Nurdan, T., Nurdan, K., Walenta, A.H., Chiosa, I., Freisleben, B., Pavel, N.A., & Struder, L. 2005. First results on Compton camera coincidences with the silicon drift detector. *Nuclear Science, IEEE Transactions on*, **52**(5), 1381–1385.

Cooper, R.J., Boston, A.J., Boston, H.C., Cresswell, J.R., Grint, A.N., Mather, A.R., Nolan, P.J., Scraggs, D.P., Turk, G., Hall, C.J., Lazarus, I., Berry, A., Beveridge, T., Gillam, J., & Lewis, R.A. 2007. SmartPET: Applying HPGe and pulse shape analysis to small-animal PET. *Nuclear Instruments and Methods in Physics Research Section A: Accelerators, Spectrometers, Detectors and Associated Equipment*, **579**(1), 313 – 317.

Dedek, N., Speller, R.D., Spendley, P., & Horrocks, J.A. 2008. Performance Evaluation of 98 CZT Sensors for Their Use in Gamma-Ray Imaging. *Nuclear Science, IEEE Transactions on*, **55**(5), 2689–2697.

Dogan, N., & Wehe, D.K. 1994. Efficiency and angular resolution calculations for a prototype multiple Compton scatter camera. *Nuclear Instruments and Methods in Physics Research Section A: Accelerators, Spectrometers, Detectors and Associated Equipment*, **345**(2), 296 – 302.

Dogan, N., Wehe, D.K., & Knoll, G.F. 1990. Multiple Compton scattering gamma ray imaging camera. *Nuclear Instruments and Methods in Physics Research Section A: Accelerators, Spectrometers, Detectors and Associated Equipment*, **299**(1-3), 501 – 506.

Dogan, N., Wehe, D.K., & Akcasu, A.Z. 1992. A source reconstruction method for multiple scatter Compton cameras. *Nuclear Science, IEEE Transactions on*, **39**(5), 1427–1430.

Driol, C., Nguyen, M.K., & Truong, T.T. 2008. Modeling and simulation results on high sensitivity scattered gamma-ray emission imaging. *Simulation Modelling Practice and Theory*, **16**(8), 1067 – 1076.

Du, Y. F., He, Z., Knoll, G. F., Wehe, D. K., & Li, W. 2001. Evaluation of a Compton scattering camera using 3-D position sensitive CdZnTe detectors. *Nuclear Instruments and Methods in Physics Research Section A: Accelerators, Spectrometers, Detectors and Associated Equipment*, **457**(1-2), 203 – 211.

Earnhart, Jonathan, Prettyman, Thomas, Lestone, John, & Gardner, Robin. 2000. Simulation of Compton camera imaging with a specific purpose Monte Carlo code. *Applied Radiation and Isotopes*, **53**(4-5), 673 – 680.

Eisen, Y., Shor, A., & Mardor, I. 2004. CdTe and CdZnTe X-ray and gamma-ray detectors for imaging systems. *Nuclear Science, IEEE Transactions on*, **51**(3), 1191–1198.

Eskin, J. D., Barrett, H. H., & Barber, H. B. 1999. Signals induced in semiconductor gamma-ray imaging detectors. *Journal of Applied Physics*, **85**(2), 647–659.

Evans, B.L., Martin, J.B., Burggraf, L.W., & Roggemann, M.C. 1997. Nondestructive inspection using Compton scatter tomography. *Pages 386–390 vol.1 of: Nuclear Science Symposium, 1997. IEEE.*

Everett, D.B., Fleming, J. S., Todd, R.W., & Nightingale, J. M. 1977. Gamma-radiation imaging system based on the Compton effect. *Electrical Engineers, Proceedings of the Institution of*, **124**(11), 995–.

Farahmand, M., Boston, A.J., Grint, A.N., Nolan, P.J., Joyce, M.J., Mackin, R.O., D'Mellow, B., Aspinall, M., Peyton, A.J., & van Silfhout, R. 2007. Detection of explosive substances by tomographic inspection using neutron and gamma-ray spectroscopy. *Nuclear Instruments and Methods in Physics Research Section B: Beam Interactions with Materials and Atoms*, **261**(1-2), 396 – 400.

Fukazawa, Y., Nakamoto, T., Sawamoto, N., Uno, S., Ohsugi, T., Tajima, H., Takahashi, T., Mitani, T., Tanaka, T., & Nakazawa, K. 2005. Development of low-noise double-sided silicon strip detector for cosmic soft gamma-ray Compton Camera. *Nuclear Instruments and Methods in Physics Research Section A: Accelerators, Spectrometers, Detectors and Associated Equipment*, **541**(1-2), 342 – 349.

Fullerton, G.D., Hazle, J.D., Orton, C.G., *et al.* 2005. The development of technologies for molecular imaging should be driven principally by biological questions to be addressed rather than by simply modifying existing imaging technologies. *Medical physics*, **32**, 1231.

Gabathuse, Justice. 2005. *Performance Evaluation of the UCL Germanium Compton Camera for Nuclear Medicine Applications.* MPhil Transfer Report, University College London.

Georgiev, A., & Gast, W. 1993. Digital pulse processing in high resolution, high throughput, gamma-ray spectroscopy. *Nuclear Science, IEEE Transactions on*, **40**, 770–779.

Gholamrezanejhad, A., Mirpour, S., & Mariani, G. 2009. Future of nuclear medicine: SPECT versus PET. *Journal of Nuclear Medicine*, **50**(7), 16N.

Gillam, John E., Beveridge, Toby E., Boston, Andrew J., Boston, Helen C., Cooper, Reynold J., Hall, Chris J., Mather, Andrew R., Nolan, Paul J., & Lewis, Rob A. 2007. Effect of position resolution on LoR discrimination for a dual-head Compton camera. *Nuclear Instruments and Methods in Physics Research Section A: Accelerators, Spectrometers, Detectors and Associated Equipment*, **573**(1-2), 76 – 79.

Gormley, J. E., Rogers, W. L., Clinthorne, N. H., Wehe, D. K., & Knoll, G. F. 1997. Experimental comparison of mechanical and electronic gamma-ray collimation. *Nuclear Instruments and Methods in Physics Research Section A: Accelerators, Spectrometers, Detectors and Associated Equipment*, **397**(2-3), 440 – 447.

Grignon, C., Barbet, J., Bardis, M., Carlier, T., Chatal, J.F., Couturier, O., Cussonneau, J.P., Faivre, A., Ferrer, L., Girault, S., Haruyama, T., Ray, P. Le, Luquin, L., Lupone, S., Mtivier, V., Morteau, E., Servagent, N., & Thers, D. 2007. Nuclear medical imaging using [beta]+[gamma] coincidences from 44Sc radio-nuclide with

liquid xenon as detection medium. *Nuclear Instruments and Methods in Physics Research Section A: Accelerators, Spectrometers, Detectors and Associated Equipment*, **571**(1-2), 142 – 145.

Harkness, L.J., Boston, A.J., Boston, H.C., Cooper, R.J., Cresswell, J.R., Grint, A.N., Nolan, P.J., Oxley, D.C., Scraggs, D.P., Beveridge, T., Gillam, J., & Lazarus, I. 2009. Optimisation of a dual head semiconductor Compton camera using Geant4. *Nuclear Instruments and Methods in Physics Research Section A: Accelerators, Spectrometers, Detectors and Associated Equipment*, **In Press, Uncorrected Proof**, –.

Haskins, P.S., McKisson, J.E., Neelands, K.C., & Henderson, D.P., Jr. 1996. Point source resolution performance of a germanium Compton camera. *Nuclear Science, IEEE Transactions on*, **43**(3), 1832–1836.

Hattori, K., Kabuki, S., Kubo, H., Kurosawa, S., Miuchi, K., Nagayoshi, T., Nishimura, H., Okada, Y., Orito, R., Sekiya, H., Takada, A., Takeda, A., Tanimori, T., & Ueno, K. 2007. Gamma-ray imaging with a large micro-TPC and a scintillation camera. *Nuclear Instruments and Methods in Physics Research Section A: Accelerators, Spectrometers, Detectors and Associated Equipment*, **581**(1-2), 517 – 521.

Heller, Gary, Calnon, Dennis, & Dorbala, Sharmila. 2009. Recent advances in cardiac PET and PET/CT myocardial perfusion imaging. *Journal of Nuclear Cardiology*, **16**, 962–969. 10.1007/s12350-009-9142-5.

Hua, C. 2000. *Compton imaging system development and performance assessment*. Ph.D. thesis, The University of Michigan.

Hua, C.H., Clinthorne, N.H., Wilderman, S.J., LeBlanc, J.W., & Rogers, W.L. 1999. Quantitative evaluation of information loss for Compton cameras. *Nuclear Science, IEEE Transactions on*, **46**(3), 587–593.

Jansen, Floris P., & Vanderheyden, Jean-Luc. 2007. The future of SPECT in a time of PET. *Nuclear Medicine and Biology*, **34**(7), 733 – 735.

Jordanov, V.T., Petrick, N., Martin, J.B., & Wehe, D.K. 1994. A data acquisition system for a Ring Compton-scatter Camera. *Nuclear Science, IEEE Transactions on*, **41**(1), 92–96.

Kabuki, Shigeto, Hattori, Kaori, Kohara, Ryota, Kunieda, Etsuo, Kubo, Atsushi, Kubo, Hidetoshi, Miuchi, Kentaro, Nakahara, Tadaki, Nagayoshi, Tsutomu, Nishimura, Hironobu, Okada, Yoko, Orito, Reiko, Sekiya, Hiroyuki, Shirahata, Takashi, Takada, Atsushi, Tanimori, Toru, & Ueno, Kazuki. 2007. Development of Electron Tracking Compton Camera using micro pixel gas chamber for medical imaging. *Nuclear Instruments and Methods in Physics Research Section A: Accelerators, Spectrometers, Detectors and Associated Equipment*, **580**(2), 1031 – 1035.

Kamea, T., & Hanada, H. 1988. *IEEE Trans. Nucl. Sci.*, **NS-35 (1)**, 352.

Khamzin, M., Valentine, J.D., & Li, Junqiang. 2002. False-preferred event analysis for the energy-subtraction Compton scatter camera. *Nuclear Science, IEEE Transactions on*, **49**(6), 3262–3268.

Kim, N.Y., Lee, J.H., Kim, J.Y., Lee, C.S., & Jang, Z.H. 2006. Development of a customized leading-edge discriminator for a planar-type segmented germanium detector. *Nuclear Instruments and Methods in Physics Research Section A: Accelerators, Spectrometers, Detectors and Associated Equipment*, **563**(1), 104 – 107.

Kim, Soo Mee, Lee, Jae Sung, Lee, Mi No, Lee, Ju Hahn, Lee, Chun Sik, Kim, Chan-Hyeong, Lee, Dong Soo, & Lee, Soo-Jin. 2007. Two approaches to implementing projector-backprojector pairs for 3D reconstruction from Compton scattered data. *Nuclear Instruments and Methods in Physics Research Section A: Accelerators, Spectrometers, Detectors and Associated Equipment*, **571**(1-2), 255 – 258.

King, S.E., Phillips, G.W., Haskins, P.S., McKisson, J.E., Piercey, R.B., & Mania, R.C. 1994. A solid-state Compton camera for three-dimensional imaging. *Nuclear Instruments and Methods in Physics Research Section A: Accelerators, Spectrometers, Detectors and Associated Equipment*, **353**(1-3), 320 – 323.

Kobayashi, S., Hasebe, N., Igarashi, T., Kobayashi, M. N., Miyachi, T., Miyajima, M., Okada, H., Okudaira, O., Tezuka, C., Yokoyama, E., Doke, T., Shibamura, E., Dmitrenko, V. V., Ulin, S. E., & Vlasik, K. F. 2004. Scintillation luminescence for high-pressure xenon gas. *Nuclear Instruments and Methods in Physics Research Section A: Accelerators, Spectrometers, Detectors and Associated Equipment*, **531**(1-2), 327 – 332.

Kuykens, H.J.P., & Audet, S.A. 1988. A 3 3 silicon drift chamber array for application in an electronic collimator. *Nuclear Instruments and Methods in Physics Research Section A: Accelerators, Spectrometers, Detectors and Associated Equipment*, **273**(2-3), 570 – 574.

LeBlanc, J. W., Clinthorne, N. H., Hua, C., Rogers, W. L., Wehe, D. K., & Wilderman, S. J. 1999a. A Compton camera for nuclear medicine applications using 113mIn1. *Nuclear Instruments and Methods in Physics Research Section A: Accelerators, Spectrometers, Detectors and Associated Equipment*, **422**(1-3), 735 – 739.

LeBlanc, J.W., Clinthorne, N.H., Hua, C.-H., Nygard, E., Rogers, W.L., Wehe, D.K., Weilhammer, P., & Wilderman, S.J. 1998. C-SPRINT: a prototype Compton camera system for low energy gamma ray imaging. *Nuclear Science, IEEE Transactions on*, **45**(3), 943–949.

LeBlanc, J.W., Clinthorne, N.H., Hua, C.-H., Nygard, E., Rogers, W.L., Wehe, D.K., Weilhammer, P., & Wilderman, S.J. 1999b. Experimental results from the C-SPRINT prototype Compton camera. *Nuclear Science, IEEE Transactions on*, **46**(3), 201–204.

Lee, J.H., & Lee, C.S. 2004. Studies on sensitivity, resolution, and Doppler broadening in gamma-ray imaging with pixellated semiconductor detectors. *Nuclear Physics A*, **746**, 639 – 642.

Lee, J.H., Kim, N.Y., Lee, C.S., & Jang, Z.H. 2005. Development of the multi-purpose gamma-ray detection system consisting of a double-sided silicon strip detector and a 25-segmented germanium detector. *Nuclear Physics A*, **758**, 150 – 153.

Lee, Se Hyung, Seo, Hee, An, So Hyun, Lee, Jae Sung, & Kim, Chan Hyeong. 2008. Performance evaluation of a table-top Compton camera for various detector parameters. *Nuclear Instruments and Methods in Physics Research Section A: Accelerators, Spectrometers, Detectors and Associated Equipment*, **591**(1), 88 – 91.

Lee, W., Wehe, D. K., Jeong, M., Barton, P., & Berry, J. 2009. A Dual Modality Gamma Camera Using $rmLaCl_3(rmCe)$ Scintillator. *Nuclear Science, IEEE Transactions on*, **56**(1), 308–315.

Lee, Wonho, & Lee, Taewoong. 2011. 4[pi] FOV compact Compton camera for nuclear material investigations. *Nuclear Instruments and Methods in Physics Research Section A: Accelerators, Spectrometers, Detectors and Associated Equipment*, **In Press, Corrected Proof**, –.

Lee, Wonho, & Wehe, David. 2007. Hybrid gamma ray imaging–Model and results. *Nuclear Instruments and Methods in Physics Research Section A: Accelerators, Spectrometers, Detectors and Associated Equipment*, **579**(1), 200 – 204.

Lehner, C.E., He, Zhong, & Zhang, Feng. 2004. 4 Compton imaging using a 3-D position-sensitive CdZnTe detector via weighted list-mode maximum likelihood. *Nuclear Science, IEEE Transactions on*, **51**(4), 1618–1624.

Mariani, G., Bruselli, L., & Duatti, A. 2008. Is PET always an advantage versus planar and SPECT imaging? *European journal of nuclear medicine and molecular imaging*, **35**(8), 1560–1565.

Mariani, Giuliano, & Strauss, H. 2011. Positron emission and single-photon emission imaging: synergy rather than competition. *European Journal of Nuclear Medicine and Molecular Imaging*, **38**, 1189–1190. 10.1007/s00259-011-1767-3.

Mariani, Giuliano, Bruselli, Laura, Kuwert, Torsten, Kim, Edmund, Flotats, Albert, Israel, Ora, Dondi, Maurizio, & Watanabe, Naoyuki. 2010. A review on the clinical uses of SPECT/CT. *European Journal of Nuclear Medicine and Molecular Imaging*, **37**, 1959–1985. 10.1007/s00259-010-1390-8.

Martin, J.B., Knoll, G.F., Wehe, D.K., Dogan, N., Jordanov, V., Petrick, N., & Singh, M. 1993. A ring Compton scatter camera for imaging medium energy gamma rays. *Nuclear Science, IEEE Transactions on*, **40**(4), 972–978.

McKisson, J.E., Haskins, P.S., Phillips, G.W., King, S.E., August, R.A., Piercey, R.B., & Mania, R.C. 1994. Demonstration of three-dimensional imaging with a germanium Compton camera. *Nuclear Science, IEEE Transactions on*, **41**(4), 1221–1224.

McKisson, J.E., Haskins, P.S., Henderson, D.P., Jr., Neelands, K.C., Wang, C.K., & Evans, T. 1997. 3-D imaging of complex source fields with a Compton Camera Imager. *Nuclear Science, IEEE Transactions on*, **44**(3), 916–921.

Meier, D., Czermak, A., Jalocha, P., Sowicki, B., Kowal, M., Dulinski, W., Maehlum, G., Nygard, E., Yoshioka, K., Fuster, J., Lacasta, C., Mikuz, M., Roe, S., Weilhammer, P., Hua, C.-H., Park, S.-J., Wildermann, S.J., Zhang, L., Clinthorne, N.H., & Rogers, W.L. 2002. Silicon detector for a Compton camera in nuclear medical imaging. *Nuclear Science, IEEE Transactions on*, **49**(3), 812–816.

Meng, L.J., & Wehe, D.K. 2003. Feasibility study of using hybrid collimation for nuclear environmental imaging. *Nuclear Science, IEEE Transactions on*, **50**(4), 1103–1110.

Mihailescu, L., Vetter, K.M., Burks, M.T., Hull, E.L., & Craig, W.W. 2007. SPEIR: A Ge Compton camera. *Nuclear Instruments and Methods in Physics Research Section A: Accelerators, Spectrometers, Detectors and Associated Equipment*, **570**(1), 89 – 100.

Mikuz, M., Studen, A., Cindro, V., & Kramberger, G. 2002. Timing in thick silicon detectors for a Compton camera. *Nuclear Science, IEEE Transactions on*, **49**(5), 2549–2557.

Mitani, T., Tanaka, T., Nakazawa, K., Takahashi, T., Takashima, T., Tajima, H., Nakamura, H., Nomachi, M., Nakamoto, T., & Fukazawa, Y. 2004. A prototype Si/CdTe Compton camera and the polarization measurement. *Nuclear Science, IEEE Transactions on*, **51**(5), 2432–2437.

Motomura, S., Enomoto, S., Haba, H., Igarashi, K., Gono, Y., & Yano, Y. 2007. Gamma-Ray Compton Imaging of Multitracer in Biological Samples Using Strip Germanium Telescope. *Nuclear Science, IEEE Transactions on*, **54**(3), 710–717.

Myjak, M.J., & Seifert, C.E. 2008. Real-Time Compton Imaging for the Gamma-Tracker Handheld CdZnTe Detector. *Nuclear Science, IEEE Transactions on*, **55**(2), 769–777.

Niedermayr, T., Vetter, K., Mihailescu, L., Schmid, G.J., Beckedahl, D., Blair, J., & Kammeraad, J. 2005. Gamma-ray imaging with a coaxial HPGe detector. *Nuclear Instruments and Methods in Physics Research Section A: Accelerators, Spectrometers, Detectors and Associated Equipment*, **553**(3), 501 – 511.

Nishimura, H., Hattori, K., Kabuki, S., Kubo, H., Miuchi, K., Nagayoshi, T., Okada, Y., Orito, R., Sekiya, H., Takada, A., Takeda, A., Tanimori, T., & Ueno, K. 2007. Development of large area gamma-ray camera with GSO(Ce) scintillator arrays and PSPMTs. *Nuclear Instruments and Methods in Physics Research Section A: Accelerators, Spectrometers, Detectors and Associated Equipment*, **573**(1-2), 115 – 118.

Nurdan, K., onka Nurdan, T., Besch, H. J., Freisleben, B., Pavel, N. A., & Walenta, A. H. 2003. FPGA-based data acquisition system for a Compton camera. *Nuclear Instruments and Methods in Physics Research Section A: Accelerators, Spectrometers, Detectors and Associated Equipment*, **510**(1-2), 122 – 125.

Odaka, Hirokazu, Takeda, Shin'ichiro, Watanabe, Shin, nosuke Ishikawa, Shin, Ushio, Masayoshi, Tanaka, Takaaki, Nakazawa, Kazuhiro, Takahashi, Tadayuki, Tajima, Hiroyasu, & Fukazawa, Yasushi. 2007. Performance study of Si/CdTe semiconductor Compton telescopes with Monte Carlo simulation. *Nuclear Instruments and Methods in Physics Research Section A: Accelerators, Spectrometers, Detectors and Associated Equipment*, **579**(2), 878 – 885.

onka Nurdan, T., Nurdan, K., Walenta, A. H., Besch, H. J., Fiorini, C., Freisleben, B., & Pavel, N. A. 2004. Silicon drift detector readout electronics for a Compton camera. *Nuclear Instruments and Methods in Physics Research Section A: Accelerators, Spectrometers, Detectors and Associated Equipment*, **523**(3), 435 – 440.

Oonuki, Kousuke, Tanaka, Takaaki, Watanabe, Shin, Takeda, Shin'ichiro, Nakazawa, Kazuhiro, Ushio, Masayoshi, Mitani, Takefumi, Takahashi, Tadayuki, & Tajima, Hiroyasu. 2007. A stacked CdTe pixel detector for a compton camera. *Nuclear Instruments and Methods in Physics Research Section A: Accelerators, Spectrometers, Detectors and Associated Equipment*, **573**(1-2), 57 – 60.

Ordonez, Caesar E., Bolozdynya, Alexander, & Chang, Wei. 1998. Doppler Broadening of Energy Spectra in Compton Cameras. *IEEE*.

Ordonez, C.E., Bolozdynya, A., & Chang, Wei. 1997a. Dependence of angular uncertainties on the energy resolution of Compton cameras. *Pages 1122–1125 vol.2 of: Nuclear Science Symposium, 1997. IEEE*, vol. 2.

Ordonez, C.E., Bolozdynya, A., & Chang, Wei. 1997b. Doppler broadening of energy spectra in Compton cameras. *Pages 1361–1365 vol.2 of: Nuclear Science Symposium, 1997. IEEE*, vol. 2.

Ordonez, C.E., Chang, Wei, & Bolozdynya, A. 1999. Angular uncertainties due to geometry and spatial resolution in Compton cameras. *Nuclear Science, IEEE Transactions on*, **46**(4), 1142–1147.

Orito, R., Kubo, H., Miuchi, K., Nagayoshi, T., Takada, A., Tanimori, T., & Ueno, M. 2003. A novel design of the MeV gamma-ray imaging detector with Micro-TPC. *Nuclear Instruments and Methods in Physics Research Section A: Accelerators, Spectrometers, Detectors and Associated Equipment*, **513**(1-2), 408 – 412.

Orito, R., Kubo, H., Miuchi, K., Nagayoshi, T., Takada, A., Takeda, A., Tanimori, T., & Ueno, M. 2004. Compton gamma-ray imaging detector with electron tracking. *Nuclear Instruments and Methods in Physics Research Section A: Accelerators, Spectrometers, Detectors and Associated Equipment*, **525**(1-2), 107 – 113.

Oxley, D.C., Boston, A.J., Boston, H.C., Cooper, R.J., Cresswell, J.R., Grint, A.N., Nolan, P.J., Scraggs, D.P., Lazarus, I.H., & Beveridge, T.E. 2009. Quantifying the limitations of small animal positron emission tomography. *Nuclear Instruments and Methods in Physics Research Section A: Accelerators, Spectrometers, Detectors and Associated Equipment*, **In Press, Uncorrected Proof**, –.

Pani, R., Pellegrini, R., Cinti, M.N., Bennati, P., Betti, M., Vittorini, F., Mattioli, M., Trotta, G., Cencelli, V. Orsolini, Scaf, R., Navarria, F., Bollini, D., Baldazzi, G., Moschini, G., & de Notaristefani, F. 2007. Ce doped lanthanum tri-bromide SPET scanner for molecular imaging. *Nuclear Instruments and Methods in Physics Research Section A: Accelerators, Spectrometers, Detectors and Associated Equipment*, **571**(1-2), 187 – 190.

Pauli, J., Pauli, E. M., & Anton, G. 2002. ITEM–QM solutions for EM problems in image reconstruction exemplary for the Compton Camera. *Nuclear Instruments and Methods in Physics Research Section A: Accelerators, Spectrometers, Detectors and Associated Equipment*, **488**(1-2), 323 – 331.

Pavel, N. A. 2002. Particle detectors for biomedical applications–demands and trends. *Nuclear Instruments and Methods in Physics Research Section A: Accelerators, Spectrometers, Detectors and Associated Equipment*, **478**(1-2), 1 – 12.

Phillips, Gary W. 1995. Gamma-ray imaging with Compton cameras. *Nuclear Instruments and Methods in Physics Research Section B: Beam Interactions with Materials and Atoms*, **99**(1-4), 674 – 677.

Piqueras, I., Beck, F. A., Duchne, G., Medina, P., Santos, C., & Villaum, D. 2004. Segmented germanium detector developments for Compton Camera application. *Nuclear Instruments and Methods in Physics Research Section A: Accelerators, Spectrometers, Detectors and Associated Equipment*, **525**(1-2), 275 – 278.

Protic, D., Hull, E.L., Krings, T., & Vetter, K. 2005. Large-volume Si(Li) orthogonal-strip detectors for Compton-effect-based instruments. *Nuclear Science, IEEE Transactions on*, **52**(6), 3181–3185.

Radeka, V. 1988. Low-Noise Techniques in Detectors. *Annual Review of Nuclear and Particle Science*, **38**(1), 217–277.

Rahmim, A., & Zaidi, H. 2008. PET versus SPECT: strengths, limitations and challenges. *Nuclear medicine communications*, **29**(3), 193.

Ramo, Simon. 1939. Currents Induced by Electron Motion. *Proceedings of the IRE*, **27**(9), 584–585.

Reed, W. A., & Eisenberger, P. 1972. Gamma-Ray Compton Profiles of Diamond, Silicon, and Germanium. *Phys. Rev. B*, **6**(Dec), 4596–4604.

Ribberfors, Roland. 1975. Relationship of the relativistic Compton cross section to the momentum distribution of bound electron states. *Phys. Rev. B*, **12**(Sep), 2067–2074.

Rohe, R., & Valentine, J.D. 1995. A novel Compton scatter camera design for in-vivo medical imaging of radiopharmaceuticals. *Pages 1579–1583 vol.3 of: Nuclear Science Symposium and Medical Imaging Conference Record, 1995., 1995 IEEE*, vol. 3.

Royle, G.J., & Speller, R.D. 1994. Design of a Compton camera for imaging 662 keV radionuclide distributions. *Nuclear Instruments and Methods in Physics Research Section A: Accelerators, Spectrometers, Detectors and Associated Equipment*, **348**(2-3), 623 – 626.

Royle, G.J., Speller, R.D., Sellin, P., Gabathuse, J., & Ghoggali, W. 2003. Development of a pixellated germanium Compton camera for nuclear medicine. *Pages 3687–3690 Vol.5 of: Nuclear Science Symposium Conference Record, 2003 IEEE*, vol. 5.

Sauve, A.C., Hero, A.O., III, Rogers, W.L., Wilderman, S.J., & Clinthorne, N.H. 1999. 3D image reconstruction for a Compton SPECT camera model. *Nuclear Science, IEEE Transactions on*, **46**(6), 2075–2084.

Scannavini, M. G., Speller, R. D., Royle, G. J., Cullum, I., Raymond, M., Hall, G., & Iles, G. 2002. A possible role for silicon microstrip detectors in nuclear medicine: Compton imaging of positron emitters. *Nuclear Instruments and Methods in Physics Research Section A: Accelerators, Spectrometers, Detectors and Associated Equipment*, **477**(1-3), 514 – 520.

Scannavini, M.G., Speller, R.D., Royle, G.J., Cullum, I., Raymond, M., Hall, G., & Iles, G. 2000. Design of a small laboratory Compton camera for the imaging of positron emitters. *Nuclear Science, IEEE Transactions on*, **47**(3), 1155–1162.

Schmid, G. J., Beckedahl, D. A., Kammeraad, J. E., Blair, J. J., Vetter, K., & Kuhn, A. 2001. Gamma-ray Compton camera imaging with a segmented HPGe. *Nuclear Instruments and Methods in Physics Research Section A: Accelerators, Spectrometers, Detectors and Associated Equipment*, **459**(3), 565 – 576.

Schopper, Florian, Andritschke, Robert, Shaw, Henry, Nefzger, Christian, Zoglauer, Andreas, Schnfelder, Volker, & Kanbach, Gottfried. 2000. CsI calorimeter with 3-D position resolution. *Nuclear Instruments and Methods in Physics Research Section A: Accelerators, Spectrometers, Detectors and Associated Equipment*, **442**(1-3), 394 – 399.

Seo, H, Park, J H, Ushakov, A, Kim, C H, Kim, J K, Lee, J H, Lee, C S, & Lee, J S. 2011. Experimental performance of double-scattering Compton camera with anthropomorphic phantom. *Journal of Instrumentation*, **6**(01), C01024.

Seo, Hee, An, So Hyun, Kim, Jong Kyung, & Kim, Chan Hyeong. 2007. Monte Carlo study of a double-scattering Compton camera with GEANT4. *Nuclear Instruments and Methods in Physics Research Section A: Accelerators, Spectrometers, Detectors and Associated Equipment*, **580**(1), 314 – 317.

Seo, Hee, Lee, Se Hyung, Jeong, Jong Hwi, Lee, Ju Hahn, Lee, Chun Sik, Lee, Jae Sung, & Kim, Chan Hyeong. 2008a. AID A Novel Method for Improving the Imaging Resolution of a Table-Top Compton Camera. *Nuclear Science, IEEE Transactions on*, **55**(5), 2527–2530.

Seo, Hee, Lee, Se Hyung, Kim, Chan Hyeong, An, So Hyun, Lee, Ju Hahn, & Lee, Chun Sik. 2008b. Optimal geometrical configuration of a double-scattering compton camera for maximum imaging resolution and sensitivity. *Nuclear Instruments and Methods in Physics Research Section A: Accelerators, Spectrometers, Detectors and Associated Equipment*, **591**(1), 80 – 83.

Seo, Hee, Lee, Se Hyung, Jeong, Jong Hwi, Kim, Chan Hyeong, Lee, Ju Hahn, Lee, Chun Sik, & Lee, Jae Sung. 2009. Feasibility study on hybrid medical imaging device based on Compton imaging and magnetic resonance imaging. *Applied Radiation and Isotopes*, **In Press, Accepted Manuscript**, –.

Seret, Alain. 2009. Will high-resolution/high-sensitivity SPECT ensure that PET is not the only survivor in nuclear medicine during the next decade? *European Journal of Nuclear Medicine and Molecular Imaging*, **36**, 533–535. 10.1007/s00259-008-1026-4.

Shockley, W. 1938. Currents to Conductors Induced by a Moving Point Charge. *Journal of Applied Physics*, **9**(10), 635–636.

Singh, M., & Doria, D. 1983. *Med. Phys.*, 428–435.

Smith, L. E., Chen, C., Wehe, D. K., & He, Z. 2001. Hybrid collimation for industrial gamma-ray imaging: combining spatially coded and compton aperture data. *Nuclear Instruments and Methods in Physics Research Section A: Accelerators,Spectrometers,Detectors and Associated Equipment*, **462**(3), 576 – 587.

Solomon, Christopher John, & Ott, Robert John. 1988. Gamma ray imaging with silicon detectors – A Compton camera for radionuclide imaging in medicine. *Nuclear Instruments and Methods in Physics Research Section A: Accelerators, Spectrometers, Detectors and Associated Equipment*, **273**(2-3), 787 – 792.

Stepanov, V. E., Ivanov, O. P., Potapov, V. N., Sudarkin, A. N., & Urutskoev, L. I. 1999. Application of gamma-ray imager for non-destructive testing. *Nuclear Instruments and Methods in Physics Research Section A: Accelerators, Spectrometers, Detectors and Associated Equipment*, **422**(1-3), 724 – 728.

Studen, A., Cindro, V., Clinthorne, N. H., Czermak, A., Dulinski, W., Fuster, J., Han, L., Jalocha, P., Kowal, M., Kragh, T., Lacasta, C., Llos, G., Meier, D., Mikuz, M., Nygrd, E., Park, S. J., Roe, S., Rogers, W. L., Sowicki, B., Weilhammer, P., Wilderman, S. J., Yoshioka, K., & Zhang, L. 2003. Development of silicon pad detectors and readout electronics for a Compton camera. *Nuclear Instruments and Methods in Physics Research Section A: Accelerators, Spectrometers, Detectors and Associated Equipment*, **501**(1), 273 – 279.

Studen, A., Burdette, D., Chesi, E., Cindro, V., Clinthorne, N. H., Dulinski, W., Fuster, J., Han, L., Kagan, H., Lacasta, C., Llos, G., Marques, A. C., Malakhov, N., Meier, D., Mikuz, M., Park, S. J., Roe, S., Rogers, W. L., Steinberg, J., Weilhammer, P., Wilderman, S. J., Zhang, L., & Zontar, D. 2004. First coincidences in pre-clinical Compton camera prototype for medical imaging. *Nuclear Instruments and Methods in Physics Research Section A: Accelerators, Spectrometers, Detectors and Associated Equipment*, **531**(1-2), 258 – 264.

Tajima, H., Nakamoto, T., Tanaka, T., Uno, S., Mitani, T., Silva, Ed.Ce., Fukazawa, Y., Kamae, T., Madejski, G., Marlow, D., Nakazawa, K., Nomachi, M., Okada, Y., & Takahashi, T. 2004. Performance of a low noise front-end ASIC for Si/CdTe detectors in Compton gamma-ray telescope. *Nuclear Science, IEEE Transactions on*, **51**(3), 842–847.

Tajima, H., Kamae, T., Madejski, G., Mitani, T., Nakazawa, K., Tanaka, T., Takahashi, T., Watanabe, S., Fukazawa, Y., Ikagawa, T., Kataoka, J., Kokubun, M., Makishima, K., Terada, Y., Nomachi, M., & Tashiro, M. 2005. Design and performance of the soft gamma-ray detector for the NeXT mission. *Nuclear Science, IEEE Transactions on*, **52**(6), 2749–2757.

Takada, A., Hattori, K., Kubo, H., Miuchi, K., Nagayoshi, T., Nishimura, H., Okada, Y., Orito, R., Sekiya, H., Tada, A., & Tanimori, T. 2005. Development of an advanced Compton camera with gaseous TPC and scintillator. *Nuclear Instruments and Methods in Physics Research Section A: Accelerators, Spectrometers, Detectors and Associated Equipment*, **546**(1-2), 258 – 262.

Takada, A., Hattori, K., Kabuki, S., Kubo, H., Miuchi, K., Nagayoshi, T., Nishimura, H., Okada, Y., Orito, R., Sekiya, H., Takeda, A., Tanimori, T., & Ueno, K. 2007. A very large area Micro Pixel Chamber. *Nuclear Instruments and Methods in*

Physics Research Section A: Accelerators, Spectrometers, Detectors and Associated Equipment, **573**(1-2), 195 – 199.

Tindall, C.S., Amman, M., & Luke, P.N. 2004. Large-area Si(Li) orthogonal-strip detectors. *Nuclear Science, IEEE Transactions on*, **51**(3), 1140–1143.

Todd, R.W., NIGHTINGALE, J.M., & EVERETT, D.B. 1974. A Proposed Gamma Camera. *Nature*, **251**, 132–134.

Tomitani, T., & Hirasawa, M. 2003. Analytical image reconstruction of cone-beam projections from limited-angle Compton camera data. *Nuclear Science, IEEE Transactions on*, **50**(5), 1602–1608.

Tumer, T.O., Yin, S., & Kravis, Scott. 1997. A high sensitivity, electronically collimated gamma camera. *Nuclear Science, IEEE Transactions on*, **44**(3), 899–904.

Uche, C.Z., Round, W.H., & Cree, M.J. 2011. Effects of energy threshold and dead time on Compton camera performance. *Nuclear Instruments and Methods in Physics Research Section A: Accelerators, Spectrometers, Detectors and Associated Equipment*, **In Press, Corrected Proof**, –.

Ueno, Kazuki, Hattori, Kaori, Ida, Chihiro, Iwaki, Satoru, Kabuki, Shigeto, Kubo, Hidetoshi, Kurosawa, Shunsuke, Miuchi, Kentaro, Nagayoshi, Tsutomu, Nishimura, Hironobu, Orito, Reiko, Takada, Atsushi, & Tanimori, Toru. 2008. Performance of the gamma-ray camera based on GSO(Ce) scintillator array and PSPMT with the ASIC readout system. *Nuclear Instruments and Methods in Physics Research Section A: Accelerators, Spectrometers, Detectors and Associated Equipment*, **591**(1), 268 – 271.

Uhlmann, N., Wolfel, S., Pauli, J., & Anton, G. 2005. 3D-position-sensitive compact scintillation detector as absorber for a Compton-camera. *Nuclear Science, IEEE Transactions on*, **52**(3), 606–611.

Ullan, M., Lozano, M., Campabadal, F., Fleta, C., Garcia, C., Gonzalez, F., & Bernabeu, J. 2004. High-pitch metal-on-glass technology for pad pitch adaptation between detectors and readout electronics. *Nuclear Science, IEEE Transactions on*, **51**(3), 968–974.

V. Schoenfelder, et al. 1973. *Nucl. Instr. and Meth.*

Vetter, K., Burks, M., & Mihailescu, L. 2004. Gamma-ray imaging with position-sensitive HPGe detectors. *Nuclear Instruments and Methods in Physics Research Section A: Accelerators, Spectrometers, Detectors and Associated Equipment*, **525**(1-2), 322 – 327.

Vetter, K., Burks, M., Cork, C., Cunningham, M., Chivers, D., Hull, E., Krings, T., Manini, H., Mihailescu, L., Nelson, K., Protic, D., Valentine, J., & Wright, D.

2007. High-sensitivity Compton imaging with position-sensitive Si and Ge detectors. *Nuclear Instruments and Methods in Physics Research Section A: Accelerators, Spectrometers, Detectors and Associated Equipment*, **579**(1), 363 – 366.

Walenta, A.H., Brill, A.B., Castoldi, A., Conka-Nurdan, T., Guazzoni, C., Hartmann, K., Longoni, A., Nurdan, K., & Struder, L. 2005. Vertex detection in a stack of Si-drift detectors for high resolution gamma-ray imaging. *Nuclear Science, IEEE Transactions on*, **52**(5), 1434–1438.

Watanabe, S., Tanaka, T., Nakazawa, K., Mitani, T., Oonuki, K., Takahashi, T., Takashima, T., Tajima, H., Fukazawa, Y., Nomachi, M., Kubo, S., Onishi, M., & Kuroda, Y. 2005. A Si/CdTe semiconductor Compton camera. *Nuclear Science, IEEE Transactions on*, **52**(5), 2045–2051.

Watanabe, Shin, Tanaka, Takaaki, Oonuki, Kousuke, Mitani, Takefumi, Takeda, Shin'ichiro, Kishishita, Tetsuichi, Nakazawa, Kazuhiro, Takahashi, Tadayuki, Kuroda, Yoshikatsu, & Onishi, Mitsunobu. 2006. Development of CdTe pixel detectors for Compton cameras. *Nuclear Instruments and Methods in Physics Research Section A: Accelerators, Spectrometers, Detectors and Associated Equipment*, **567**(1), 150 – 153.

Watanabe, Shin, Takeda, Shin'ichiro, nosuke Ishikawa, Shin, Odaka, Hirokazu, Ushio, Masayoshi, Tanaka, Takaaki, Nakazawa, Kazuhiro, Takahashi, Tadayuki, Tajima, Hiroyasu, Fukazawa, Yasushi, Kuroda, Yoshikatsu, & Onishi, Mitsunobu. 2007. Development of semiconductor imaging detectors for a Si/CdTe Compton camera. *Nuclear Instruments and Methods in Physics Research Section A: Accelerators, Spectrometers, Detectors and Associated Equipment*, **579**(2), 871 – 877.

Weilhammer, Peter. 2003. Front end electronics for multi-channel semiconductor imaging systems. *Nuclear Instruments and Methods in Physics Research Section A: Accelerators, Spectrometers, Detectors and Associated Equipment*, **497**(1), 210 – 220.

Wilderman, S.J., Rogers, W.L., Knoll, G.F., & Engdahl, J.C. 1997. Monte Carlo calculation of point-spread functions of Compton scatter cameras. *Nuclear Science, IEEE Transactions on*, **44**(2), 250–254.

Wilderman, S.J., Rogers, W.L., Knoll, G.F., & Engdahl, J.C. 1998. Fast algorithm for list mode back-projection of Compton scatter camera data. *Nuclear Science, IEEE Transactions on*, **45**(3), 957–962.

Wulf, E.A., Phlips, B.F., Johnson, W.N., Kurfess, J.D., & Novikova, E.I. 2004. Thick silicon strip detector Compton imager. *Nuclear Science, IEEE Transactions on*, **51**(5), 1997–2003.

Xu, D., & He, Z. 2007. Gamma-ray energy-imaging integrated spectral deconvolution. *Nuclear Instruments and Methods in Physics Research Section A: Accelerators, Spectrometers, Detectors and Associated Equipment*, **574**(1), 98 – 109.

Xu, D., & He, Zhong. 2006. Filtered Back-Projection in4*pi*Compton Imaging With a Single 3D Position Sensitive CdZnTe Detector. *Nuclear Science, IEEE Transactions on*, **53**(5), 2787–2796.

Yang, Y. F., Gono, Y., Motomura, S., Enomoto, S., & Yano, Y. 2002. Monte Carlo simulations of the performance of a Compton camera consisting of position-sensitive germanium detectors. *Nuclear Instruments and Methods in Physics Research Section A: Accelerators, Spectrometers, Detectors and Associated Equipment*, **482**(3), 806 – 813.

Yang, Y.F., Gono, Y., Motomura, S., Enomoto, S., & Yano, Y. 2001. A Compton camera for multitracer imaging. *Nuclear Science, IEEE Transactions on*, **48**(3), 656–661.

Zhang, Lisha, Rogers, W Leslie, & Clinthorne, Neal H. 2004. Potential of a Compton camera for high performance scintimammography. *Physics in Medicine and Biology*, **49**(4), 617.